



UNIVERSITY OF MESSINA

DEPARTMENT OF ENGINEERING

PHD PROGRAM IN

“CHEMISTRY AND ENGINEERING OF MATERIALS AND
CONSTRUCTIONS”

**THEORETICAL AND PRACTICAL ASPECTS OF
THE CATALYTIC PATTERN OF
NANOSTRUCTURED $MnCeO_x$ SYSTEMS FOR
ENVIRONMENTAL APPLICATIONS**

Doctoral Dissertation of:

Roberto Di Chio

Supervisor:

Prof. Francesco Arena

Tutor:

Dr. Lorenzo Spadaro

Coordinator:

Prof. Signorino Galvagno

2017/2018 – XXXI Cycle

**THEORETICAL AND PRACTICAL ASPECTS OF
THE CATALYTIC PATTERN OF
NANOSTRUCTURED MnCeO_x SYSTEMS FOR
ENVIRONMENTAL APPLICATIONS**

Dissertation presented by
Roberto Di Chio
to obtain the degree:
Doctor of Philosophy
at the University of Messina

Department of Engineering

ACKNOWLEDGMENTS

With the writing of this thesis, my PhD path is about to finish. It has been three years of a long and almost never linear journey, and if I have reached the finish line I owe it to the many people who have been there for me during this trip.

First of all, I want to thank my supervisor, Prof. Francesco Arena for his guidance, his support and reproaches during this period spent as a two-men group. I hope one day I will be able to take advantage of all the teachings received and all the knowledge he tried to transmit to me.

Many are the colleagues with whom I have spent many pleasant moments, and among these I would like to show gratitude to Chal, for our long conversations and the mutual respect we have for each other, Ciccio, for sharing the burden of a PhD with me, Georgia, Salvo and Gianfranco, who have made the hours in the department a little less heavy with their wise words. Thanks also to all the people I met abroad while attending conferences, in particular in Palermo, filling me with personal experience and making me realize how enjoyable research can be.

I do not think I will ever be able to thank my friends enough, for the many beautiful moments spent together for many years now and for always believing in me way more than I did. Thanks to the *Garage people*, who kept me awake at night and sleepy during the day. Thanks to Giacomo, Gianluca, Paolo, Alessandro and Antonio, who have always been friends for me, knowing I can always count on them when I need. A thank you to Gianluca, who allowed me to peek often in that magical world that is music and to my cousin Gabriele, because even if we only met once in a year, our minds have always been connected.

Lastly, a heartfelt thanks to my family, who supported me constantly even in the most difficult moments: I will never be able to repay them for everything they did for me. Thanks to Silvia, who is always with me despite everything, sharing with me the longest silences along the longest journey.

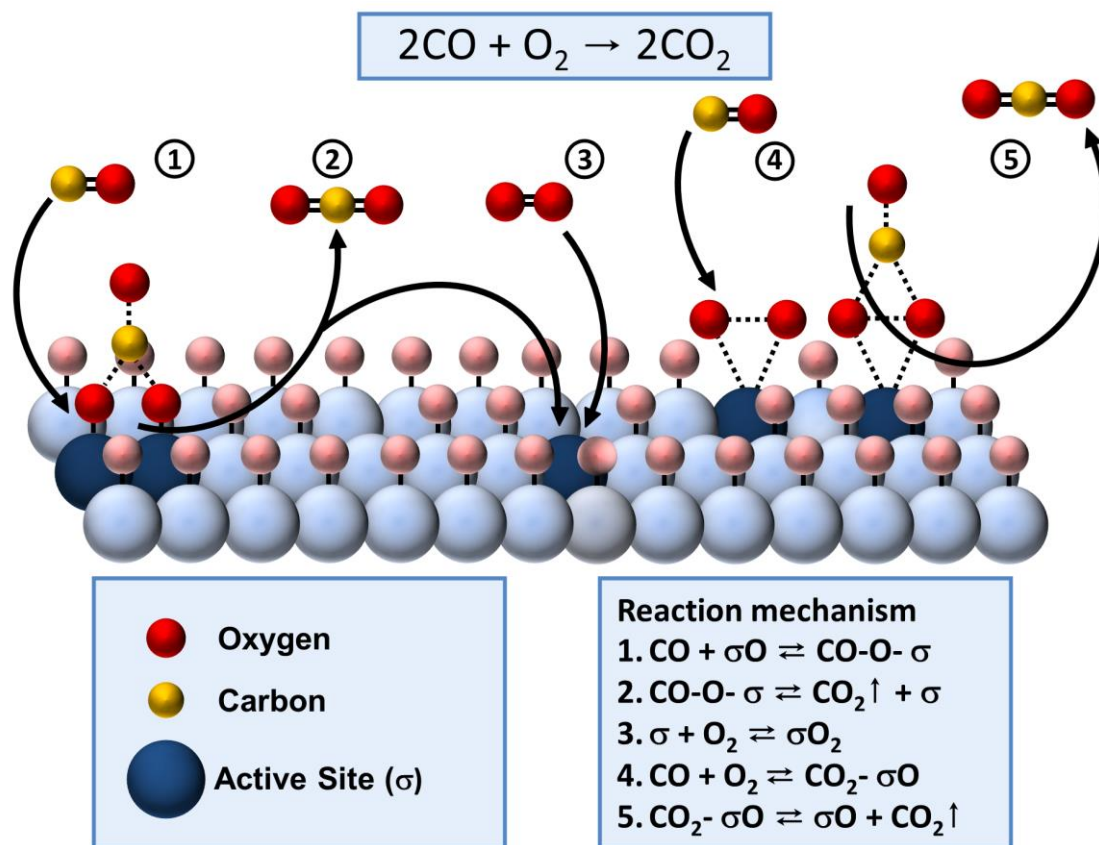
ABSTRACT

The technological development of human beings over the last few centuries has led them to produce great quantities of atmospheric pollutants. Nowadays, large areas of the globe find themselves facing pollution phenomena that undermine people's health, causing serious damage to the respiratory system, as well as to the ecosystems. Catalytic oxidation technologies proved to be successful in preventing or mitigating harmful gaseous emissions, but their large-scale exploitation is bound to the development of efficient and economical catalytic systems. Transition Metal Oxide catalysts, and in particular those based on Mn, have demonstrated excellent oxidative capacities in various applications such as the mineralization of toxic organic compounds from wastewater (CWAO), the oxidative detoxification of gas exhausts, the selective NO_x reduction (SCR), the synthesis of bio-fuels and fine chemicals, showing performance comparable or even superior to the traditional noble metal systems. Among these, the catalytic oxidation of carbon monoxide has a great value both from a scientific and technological point of view: in fact, it is considered a model reaction, which can provide basic information on the reactivity of heterogeneous catalysts but at the same time, many are the possible fields of application, ranging from the purification of industrial streams (e.g., PROX) to the development of ambient temperature operating systems for indoor or mobile applications (e.g., gas masks, gas sensors).

In this context, the work of this thesis is aimed at analyzing the practical and theoretical aspects of the oxidation of carbon monoxide on MnCeO_x catalysts. To achieve this goal, a series of samples with different Ce content was synthesized by the *redox precipitation* method and tested by means of Temperature Programmed Catalytic Reaction (TPCR) in the CO oxidation reaction. From a systematic comparison of the bulk (e.g., XRD,

Raman, BET) and superficial (XPS) characterization data, with the results of catalytic activity, it was possible to identify the Mn(IV) sites as main responsible for the marked oxidation activity of the MnCeO_x systems. Subsequently, the empiric reaction kinetics and mechanistic issues of the CO oxidation reaction were assessed on a model MnCeO_x (i.e., M5C1) catalyst. The numerous mechanistic evidences collected, led us to the formulation of a *Langmuir-Hinshelwood* reaction mechanism and the relative kinetic equation. The last goal of this work was to obtain a reaction model able to predict the reactivity pattern of the studied catalyst in a wide range of experimental conditions in terms of temperatures (293-533K), reagents pressure (p_{CO}^0 - $p_{O_2}^0$, 0.00625-0.025 atm) and CO/O₂ ratio (λ_0 , 0.25-4.0).

GRAPHICAL ABSTRACT



Graphic representation of the proposed CO oxidation reaction mechanism over MnCeO_x catalyst.

**THEORETICAL AND PRACTICAL ASPECTS OF THE CATALYTIC PATTERN OF
NANOSTRUCTURED MnCeO_x SYSTEMS FOR ENVIRONMENTAL APPLICATIONS**

TABLE OF CONTENTS

ACKNOWLEDGMENTS	I
ABSTRACT	III
GRAPHICAL ABSTRACT.....	V
1. INTRODUCTION	1
1.1 Air Quality.....	1
1.2 Air Pollutants.....	6
1.3 Carbon Monoxide.....	8
1.3.1 Effects on human health	8
1.3.2 Carbon Monoxide Sources.....	10
1.4 The Relevance of Heterogeneous Catalysis in Modern Life	13
1.5 Carbon Monoxide Catalytic Oxidation	15
1.5.1 Noble Metal Catalysts.....	17
1.5.1.1 Alumina- or silica-supported	17
1.5.1.2 Ceria-supported.....	18
1.5.1.3 Gold-Based	19
1.5.2 Metal Oxide Catalysts.....	19
1.5.2.1 Cobalt oxides	20
1.5.2.2 Copper oxides	21
1.5.2.3 Manganese oxides	23
2. MATERIALS AND METHODS.....	28
2.1 Catalysts Preparation.....	28
2.1.1 Redox-precipitation Method	28
2.2 Catalyst Characterization	29
2.2.1 X-ray fluorescence (XRF).....	29
2.2.2 N ₂ physisorption isotherm (SA, PV, APD).....	30
2.2.3 X-ray diffraction (XRD)	30
2.2.4 Laser Raman Spectroscopy (RS).....	30
2.2.5 X-ray Photoelectron Spectroscopy (XPS)	31

2.2.1	Temperature programmed reduction (TPR).....	31
2.2.2	Temperature Programmed Desorption (TPD).....	32
2.2.3	Steady-state O ₂ uptake measurements	32
2.2.4	Surface Oxygen Content (SOC) Measurements.....	32
2.3	Catalyst Testing	33
2.3.1	Temperature programmed catalytic reaction (TPCR) test	33
2.3.2	Quadrupole Mass Spectrometer (QMS)	33
3.	RESULTS AND DISCUSSION.....	38
3.1	Results and Discussion Outlines.....	38
3.2	The Kinetic Regime of CO Oxidation Tests: Theoretical and Experimental Evaluations ..	39
3.2.1	Reliability and reproducibility of catalytic data	39
3.2.2	Theoretical evaluations of diffusional resistances.....	41
3.2.3	Experimental assessment of the kinetic regime	43
3.3	Effect of Cerium on the Reactivity Pattern of Composite MnCeO_x Catalysts and Nature of Active Sites.....	46
3.3.1	Effects of cerium on the CO oxidation activity	46
3.3.2	Effects of cerium addition on the physico-chemical properties of composite MnCeO _x catalysts	49
3.3.2.1	Structural and textural characterization.....	49
3.3.2.2	Surface Chemistry	53
3.3.2.3	Redox properties.	56
3.3.3	Structure-activity relationships.	58
3.3.4	Conclusions	62
3.4	Kinetic and Mechanistic Evidences	63
3.4.1	Empiric Kinetics.....	63
3.4.2	Mechanistic evidences	67
3.4.2.1	Mobility and reactivity of catalyst oxygen species	67
3.4.2.2	Surface interactions and reaction intermediates.....	69
3.4.3	Reaction mechanism.....	74
3.4.4	Kinetic Modelling.....	79
3.4.5	Conclusions	85
4.	FINAL REMARKS AND FUTURE PROSPECTS	87
5.	REFERENCES.....	89
	APPENDIX A: LIST OF TABLES	97
	APPENDIX B: LIST OF FIGURES	98
	APPENDIX C: LIST OF PUBLICATIONS AND CONGRESSES PARTICIPATION.....	100

1. INTRODUCTION

1.1 Air Quality

Every human being needs to breathe clean air to survive. This is because our species, over the millennia, has evolved adapting to life on Earth and therefore to its atmosphere, which is a mixture of different gases, particles and aerosols enveloping our planet. It provides various functions, not least the ability to sustain life by filtering out deadly cosmic rays, powerful ultraviolet (UV) radiation from the Sun, and even meteors on collision course with Earth.

Air composition, which may vary locally, can be considered uniform from a global point of view, as a result of efficient recycling processes and turbulent mixing in the atmosphere. Such recycling and mixing of the air helps to minimise the amount of time spent by man-made pollution in the atmosphere at any single location, thereby reducing the local environmental impacts. The current atmospheric composition is the product of billions of years of biochemical modification of the *paleoatmosphere* by living organisms: the two most abundant gases are nitrogen (78% by volume) and oxygen (21% by volume), and together they make up over 99% of the lower atmosphere. In addition to nitrogen and oxygen, air contains a number of trace gases, including the noble gases argon, neon, helium, krypton and xenon, the greenhouse gases and ozone.

Despite their relative scarcity, the greenhouse gases play an important role in the regulation of the Earth's climate. The natural greenhouse gases include carbon dioxide, methane, nitrous oxide and water vapor. By adsorbing and radiating the infrared

radiation re-emitted by the surface of the Earth, the greenhouse gases warm the atmosphere. Consequently the Surface Air Temperature (SAT) of the Earth is 33°C warmer than it would be without an atmosphere [1].

During the last 200 years, the human race has begun to meaningfully alter the composition of the atmosphere through nocive gaseous emissions. Although the concentration of oxygen and nitrogen may be considered unchanged, some of the levels of trace gases have been increasing, in particular the concentrations of greenhouse gases, which are one of the main cause of global warming. Some air pollutants now present in the atmosphere are completely new, such as the CFCs, which are solely man-made.

Air pollution, particularly in cities, is certainly not a new problem and can be traced back to the Middle Ages, when the use of coal for domestic utilities in cities such as London was beginning to escalate. This problem became even more serious during the Industrial Revolution in the 18th and 19th centuries because coal was employed for the development of new industries, which were often located in towns and cities. Together with the burning of coal in homes for domestic heat, urban air pollution levels often reached very high levels. During foggy conditions, pollution levels escalated and urban smog (smoke and fog) were formed. These often brought cities to a halt, disrupting traffic but more dangerously causing **death rates to dramatically rise**. The effects of this pollution on buildings and vegetation also became obvious. Pollutant emissions continued to grow through the 19th and early 20th centuries, and dramatic smog episodes became common place in many European cities, leading to poor air quality. In more recent times pollution from motor vehicles has become the most recognised source of air quality issue.

While great efforts have been taken by the so-called developed countries to reduce nocive gaseous emissions, air pollution levels remain dangerously high in many parts of the world. In Figure 1 we can see a snap of the world Air Quality status in July 2018 [2]. In panel A we can see how Air Quality Index for Europe and North America is, with a due exception for some industrial area, “Good” to “Moderate” (See Panel C for Air Quality Index Legend). Moving our attention to Asia (Panel B), we can easily notice that most of the cities’ Air Quality Index is indicated as Moderate and “Unhealthy for Safety Group”, with higher pollution value, such as “Unhealthy” or worse, being way more common than in the Western part of the world. Since more than half of the Earth population live in this area of the world, we should not be surprised that new data from WHO shows that 90% of people breathe air containing high levels of pollutants [3].

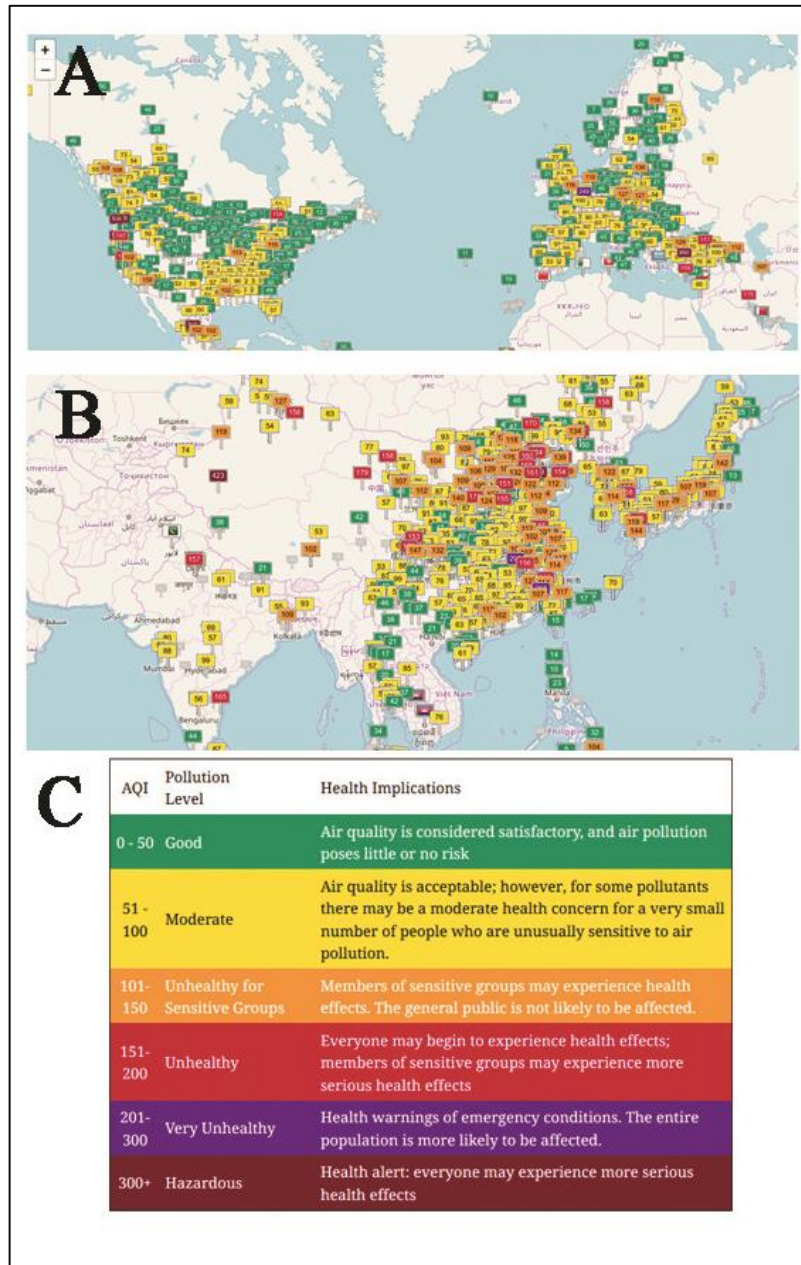


Figure 1 Snapshot of Real Time Air Quality Index map of (A) Europe and North America and (B) Asia; (C) Air Quality Index Chart [2].

WHO estimates that around 7 million people die every year from exposure to fine particles in polluted air that penetrate deep into the lungs and cardiovascular system, causing diseases including stroke, heart disease, lung cancer, chronic obstructive pulmonary diseases and respiratory infections, including pneumonia. Atmospheric pollution alone caused 4.2 million deaths in 2016, while household air pollution from

cooking with polluting fuels and technologies caused an estimated 3.8 million deaths in the same period. The highest ambient air pollution levels are in the Eastern Mediterranean Region and in South-East Asia, with annual mean levels often exceeding more than 5 times WHO limits, followed by low and middle-income cities in Africa and the Western Pacific. Unfortunately, the regions where the air pollution levels are higher, are also the ones who lack air pollution data the most, such as Africa and some of the Western Pacific. Europe, on the other hand, has the highest number of reporting data stations. Struggling between a lack of environmental policies and their economic weakness, which make the employment of modern environmental technologies unfeasible, we shouldn't be surprised that more than 90% of air pollution-related deaths occur in low- and middle-income countries, mainly in Asia and Africa, followed by low- and middle-income countries of the Eastern Mediterranean region, Europe and the Americas.

WHO has been monitoring household air pollution for more than a decade and, while the rate of access to clean fuels and technologies is increasing everywhere, improvements are not even keeping pace with population growth in many parts of the world, particularly in Sub-Saharan Africa. In fact, more than 40% of the world's population still do not have access to clean cooking fuels and technologies in their homes, the main source of household air pollution.

Air pollution does not recognize borders. Improving air quality demands sustained and coordinated government action at all levels. Countries need to work together on solutions for sustainable transport, more efficient and renewable energy production and waste management. In order to achieve this demanding task, while governments should

constantly improve and update their environmental politics, the scientific community has to focus on developing new cheaper and safer environmental technologies [3].

1.2 Air Pollutants

An air pollutant is defined as a material in the air that can have negative effects on the ecosystem and can be solid, liquid, or gaseous. It can be biogenic or anthropogenic and can also be classified as primary or secondary.

Biogenic pollutants are produced by natural sources such as volcanoes, animal digestion and wildfires while **anthropogenic** (man-made) emissions are entirely related to human activities. **Primary pollutants** are directly emitted into the atmosphere, conversely pollutants are defined as **secondary** when they form in the air by primary pollutants interaction. Some pollutants may be primary and secondary, being both emitted directly into the atmosphere and formed from other primary pollutants.

According to the above definition, a high number of substances could be considered a pollutant, but some of them require more attention than others due to the serious effects they may cause on human health or on ecosystems. Following, a list of the **main** substances emitted into the atmosphere by human activities:

- *Carbon dioxide* (CO₂) is a natural component of the atmosphere, essential for the development of plants and emitted by humans through breathing. Nowadays is considered the most important pollutant due to its role as a greenhouse gas. CO₂ currently forms about 410 parts per million (ppm) of earth's atmosphere, compared to about 280 ppm in pre-industrial times, and billions of metric tons of

CO₂ are emitted annually by burning of fossil fuels. CO₂ increase in earth's atmosphere has been accelerating;

- *Sulfur oxides* (SO_x), particularly sulphur dioxide, SO₂, produced by various industrial processes and fossil fuels combustion. Further oxidation of SO₂, usually in the presence of a catalyst such as NO₂, forms H₂SO₄, and thus acid rain;
- *Nitrogen oxides* (NO_x), particularly nitrogen dioxide, are expelled from high temperature combustion engines such as Diesel engines.
- *Carbon monoxide* (CO) is a colorless, odorless, toxic yet non-irritating gas. Given its importance in this thesis work, paragraph 1.3 will be entirely dedicated to this pollutant.
- *Volatile organic compounds* (VOC) can be categorized as either methane (CH₄) or non-methane (NMVOCs). Methane direct emissions produce a significant greenhouse effect, while NMVOCs contribute to this problem by prolonging the life time of methane in the atmosphere and creating ozone. Among the NMVOCs we find many substances with carcinogenic effects like benzene, toluene and xylene which can directly impact human health.
- *Particulates*, alternatively referred to as particulate matter (PM), atmospheric particulate matter, or fine particles, are tiny particles of solid or liquid suspended in a gas. Human activities, such as the burning of fossil fuels in vehicles, power plants and various industrial processes also generate significant amounts of aerosols. Averaged worldwide, anthropogenic aerosols, currently account for approximately 10 percent of our atmosphere. Increased levels of fine particles in

the air are linked to health hazards such as heart disease, altered lung function and lung cancer.

- *Ground level ozone* (O_3) is a secondary pollutant formed by reaction between NO_x and VOCs. Ozone (O_3) is a key constituent of the troposphere and also an important constituent of certain regions of the stratosphere commonly known as the Ozone layer. At abnormally high concentrations, in the lower regions of the atmosphere, due to human activities (mainly the combustion of fossil fuel), it is a pollutant and a constituent of smog.

1.3 Carbon Monoxide

Carbon monoxide is a colorless, tasteless and odorless gas, with a slightly smaller density than air. It is mainly produced by the partial oxidation of carbon containing compound in defect of oxygen. Carbon monoxide consists of one carbon atom and one oxygen atom, connected by a triple bond that consists of two covalent bonds as well as one dative covalent bond. The bond length between the carbon atom and the oxygen atom is 112.8 pm [4]. The gas was identified as a compound containing carbon and oxygen by the Scottish chemist William Cumberland Cruikshank in 1800.

1.3.1 Effects on human health

Known as the “silent killer”, carbon monoxide is a very poisonous gas. It is especially dangerous to humans because it is hardly detected by our senses. The toxic effects of CO have been known since ancient history [5] but the realization that hemoglobin was affected by CO was only determined in 1857 [5]. Hemoglobin contains four *heme* groups, each capable of reversibly binding to one oxygen molecule [6]. Oxygen binding to any of these sites causes a conformational change in the protein, facilitating binding

to each of the other sites. Carbon monoxide binds to hemoglobin at the same sites as oxygen, forming *carboxyhaemoglobin* (HbCO), a complex which is approximately 200 times more stable than the one formed with oxygen, *oxyhemoglobin* (HbO₂) [6]. Normally, oxygen would bind to hemoglobin in the lungs and be released in areas with low oxygen partial pressure (e.g. active muscles) [7]. When carbon monoxide binds to hemoglobin, it cannot be released as easily as oxygen. The slow release rate of carbon monoxide causes an accumulation of CO-bound hemoglobin molecules as exposure to carbon monoxide continues. Because of this, fewer hemoglobin particles are available to bind and deliver oxygen, thus causing the gradual suffocation associated with carbon monoxide poisoning [8]. The most common symptoms of CO poisoning are headache, dizziness, weakness, upset stomach, vomiting, chest pain, and confusion. CO symptoms are often described as “flu-like”. As can be seen in Table 1, breathing air that contains even small amounts of CO can prove fatal. A concentration of only 1% is enough to cause death in only a few minutes [9,10]. Carbon monoxide poisoning is relatively common, resulting in more than 20,000 emergency department visits a year in the United States [11]. It is the most common type of fatal poisoning in many countries [12]. In the United States, non-fire related cases result in more than 400 deaths a year. Everyone is at risk for CO poisoning, but Sensitive Groups such as infants, elderly, people with chronic heart disease, anemia, or breathing problems are more likely to get sick from CO.

Table 1. *Effects of carbon monoxide in relation to the concentration in parts per million in the air*

Concentration	Symptoms
35 ppm (0.0035%)	Headache and dizziness within 6-8 hours of constant exposure
100 ppm (0.01%)	Slight headache in two to three hours
200 ppm (0.02%)	Slight headache within two to three hours; loss of judgment
400 ppm (0.04%)	Frontal headache within one to two hours
800 ppm (0.08%)	Dizziness, nausea, and convulsions within 45 min; insensible within 2 hours
1,600 ppm (0.16%)	Headache, increased heart rate, dizziness, and nausea within 20 min; death in less than 2 hours
3,200 ppm (0.32%)	Headache, dizziness and nausea in five to ten minutes. Death within 30 minutes.
6,400 ppm (0.64%)	Headache and dizziness in one to two minutes. Convulsions, respiratory arrest, and death in less than 20 minutes.
12,800 ppm (1.28%)	Unconsciousness after 2–3 breaths. Death in less than three minutes.

1.3.2 Carbon Monoxide Sources

More than half of atmospheric CO emissions today are caused by human activities, especially in developed countries. As a result the Northern Hemisphere contains about twice as much CO as the Southern Hemisphere. In the high northern latitudes, CO abundances vary from about 60 ppb during summer to 200 ppb during winter. At the South Pole, CO varies between about 30 ppb in summer and 65 ppb in winter [13].

The Environmental Protection Agency (EPA) estimated that in 2011, only 26% of CO emissions in the USA can be considered of biogenic nature (see Figure 2) while the other part comes from anthropogenic activities [14]. Such portion, is distributed between stationary (such as fuel combustion and other industrial processes) and mobile (on-road and nonroad vehicles) sources. The latter, despite accounting for more than 80% of the total anthropogenic emissions, registered a steady decrease during the period 1990-2011 (see Figure 3), mainly thanks to the employment of the catalytic converter on automobile [14].

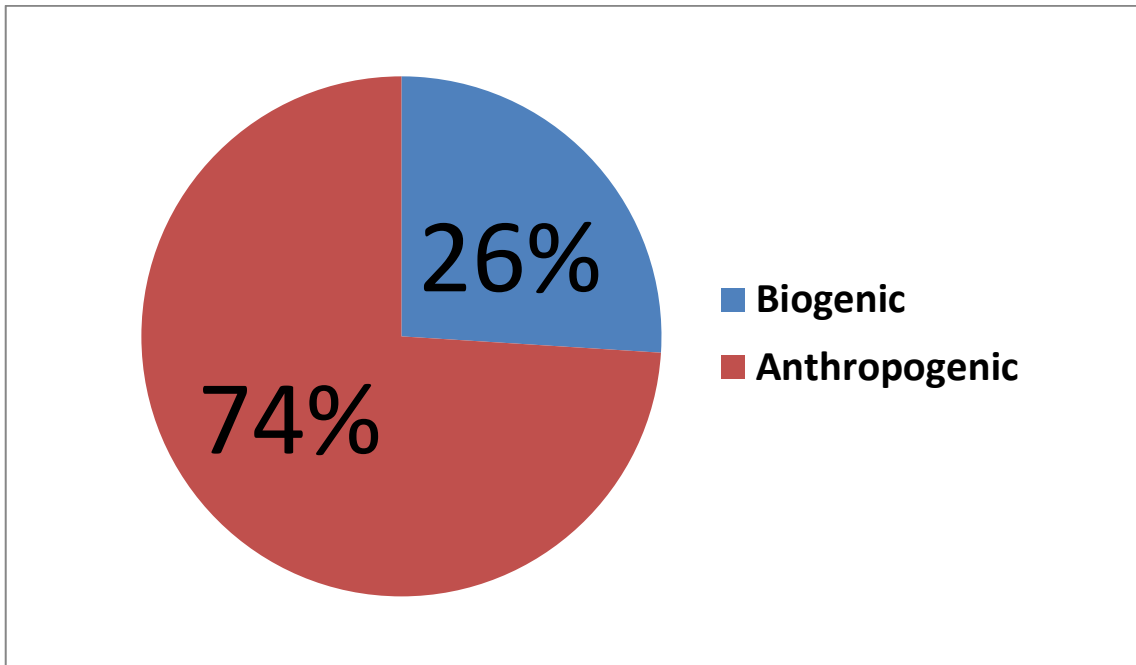


Figure 2. Relative amount of U.S. CO emissions from anthropogenic and biogenic sources in 2011 (adapted from ref. [14]).

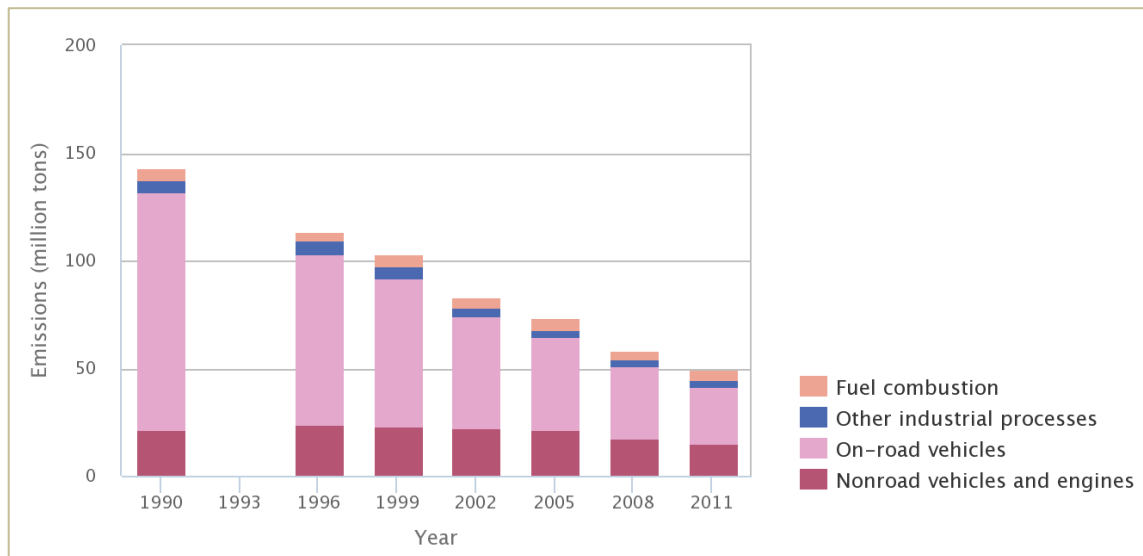


Figure 3. Anthropogenic CO emissions in the U.S. by sources category in the period 1990-2011 (adapted from ref. [14]).

Carbon monoxide does not absorb terrestrial infrared radiation strongly enough to be counted as a direct greenhouse gas, but its role in determining tropospheric OH indirectly affects the atmospheric burden of CH₄ and can lead to the formation of O₃ [13]. For this reason, the measurement of its concentration in the troposphere caught the

attention of many researchers [15–17], who tried to evaluate by modeling the impact of this gas to the green-house effect. Bergamaschi et al. used a model inversion in 2000 [16] to derive CO global sources. Their estimations (summarized in Figure 4) show that anthropogenic sources (deforestation, savanna and waste burning, fossil and domestic fuel use) dominate the direct emissions of CO, emitting 1300 out of 1460 T(CO)/yr. A source of 1402 T(CO)/yr is estimated from *in situ* oxidation of CH₄ and other hydrocarbons, and about half of this source can be attributed to anthropogenic emissions [13,16]. Daniel and Solomon estimated that the cumulative indirect radiative forcing due to anthropogenic CO emissions may be larger than that of N₂O [15].

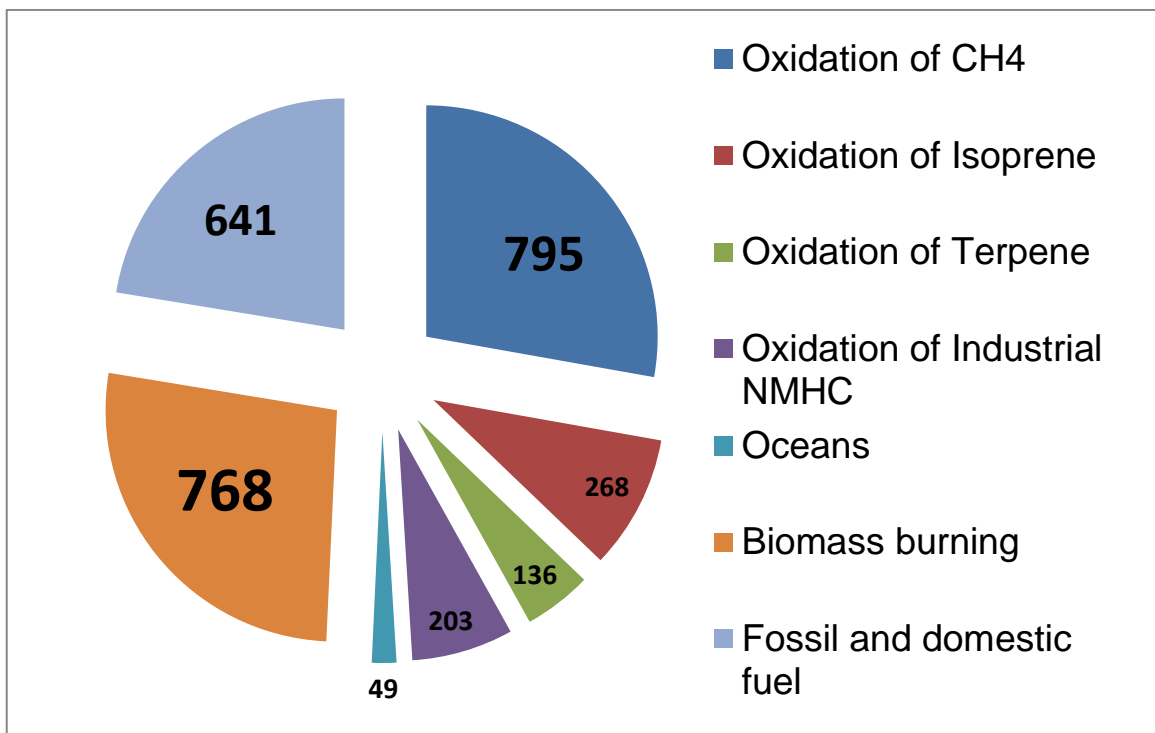


Figure 4. Sources of global CO emissions in terms of T(CO)/yr (adapted from ref. [16]).

1.4 The Relevance of Heterogeneous Catalysis in Modern Life

The transformation of chemical species through catalysis is crucial for different aspects of modern life, from agriculture to the synthesis of pharmaceuticals and will certainly lay the foundations for future technologies such as alternative energy storage and conversion and carbon sequestration. The development of the Haber-Bosch process for the synthesis of ammonia is a well known example of how catalysis impacted the society of the early 20th century. The western world of the 19th and early 20th centuries saw some of the worst food shortages in recorded history, mainly because of its rapid population growth. The only way to cope with the subsequent food demand was to employ nitrogen-rich fertilizers acquired from non-sustainable sources to improve crop yield [18]. By the end of the century, however, the scientific community recognized the need for a more sustainable fertilizers production through the discovery of artificial dinitrogen fixation, to avoid a global wheat deficiency. The discovery and commercialization of an efficient way to fix nitrogen into ammonia using an iron oxide catalyst, was so important that, despite its apparently extreme temperatures and pressures, has been credited as the most important scientific accomplishment of the 20th century. The Haber-Bosch process, by the name of its two inventors, enabled a cheaper route for nitrogen-rich fertilizers production becoming largely responsible for the global population increase from 1.6 billion people in 1900 to the current 7.4 billion [19]. In this case, catalysis has transformed the world we live in by intervening in the natural nitrogen cycle, while the 20th century economic growth was already proposing new challenges to the scientific community.

During the first half of the 20th century, catalysis continued to play a leading role in the economic growth of many countries. The development of new chemical processes, but

above all new materials (e.g. plastic materials), was in fact only possible thanks to the synthesis of new and more performing catalytic systems. Moving our attention to the second part of the century, the huge emission of gaseous pollutants discussed in the previous paragraphs, led catalysis to assume an important role from an environmental point of view. While, respecting the guidelines of **Green Chemistry**, chemical processes become more and more efficient, it is still necessary to remedy where the current production technologies are not sufficiently "clean". Catalysis is, in fact, a key technology to provide realistic solutions to many environmental issues; its areas of application in the environmental sector are multiple and continuously increasing, and include [20]:

- catalytic technologies for liquid or solid waste reduction or purification;
- use of catalysts in energy-efficient catalytic technologies and processes;
- reduction of the environmental impact in the use or disposal of catalysts;
- new eco-compatible refinery, chemical or non-chemical catalytic processes;
- **catalysis for greenhouse gas control;**
- **use of catalysts for indoor pollution reduction;**
- catalytic processes for sustainable chemistry;
- **reduction of the environmental impact of transport.**

Great efforts have been made to develop catalytic materials that can be used for eliminating atmospheric pollutants. Compared to bulk materials, nanosized or porous materials possess larger surface areas or more abundant pores, which are beneficial for the diffusion, adsorption, and activation of the reactants. In the past decades, the related

research has focused on the synthesis and environmental applications of nanosized or porous catalysts [21].

1.5 Carbon Monoxide Catalytic Oxidation

The oxidation of carbon monoxide:



in an oxygen-rich atmosphere occurs readily at high temperatures but only in the presence of certain materials at lower temperatures. The reaction is thermodynamically irreversible at room temperature, with ΔG° being equal to -256.9 KJ/mol. The major contribution to ΔG° is the high negative value of $\Delta H^\circ = -282.84$ KJ/mol. The entropy for the reaction is -86.61 J/K/mol, so the negative value of ΔG° becomes smaller as the temperature is increased. Even at very high temperatures, the equilibrium for the reaction always favors conversion to CO_2 [22]. The heterogeneous catalytic oxidation of CO has been widely studied over the last century by many investigators. Ever since the early work of Langmuir investigating CO oxidation over platinum group metals, where the conversion was improved by a heated platinum sponge which became incandescent due to the heat of reaction, scientists have been captivated by this area of research [23]. The mass diffusion of the internal combustion engine led more scientific interest in CO oxidation catalysis. Vehicle manufacturers needed a way to efficiently convert the poisonous gas, among others, into more benign gaseous products, either for environmental and safety reasons. These necessity ultimately led to the development of the modern three-way catalytic converter in use today [24], but a renewed interest in developing low-cost, earth-abundant catalysts for CO oxidation ultimately came from

the need to remove CO from hydrogen sources (most notably synthesis gas, an industrial mixture of H₂ and CO from the steam reforming of methane) since CO adsorbs and poisons the surface of platinum anodes in proton exchange membrane fuel cells [25,26]. Under such hydrogen-rich conditions, where other products can be formed, the oxidation of CO to CO₂ is referred to as Preferential CO Oxidation, PROX for short and constitutes a major field of scientific inquiry [18,27]. Other real-world applications for CO oxidation catalysis abound. In particular, due to its toxic nature for human being, a lot of attention has been drawn into researching contact agents which operate at ambient temperature [28], for applications like:

- Indoor air cleaning in building as well as in motor vehicles;
- Gas masks in military & mining fields;
- CO detectors;

Scientific research into CO oxidation catalysis is also inspired by the need to understand the fundamental reactivity of carbon monoxide, a key intermediate in C1 chemistry, with surfaces of metals and metal oxides [29]. The oxidation of CO has often been used as a catalytic test reaction due to fact that the chemisorption of carbon monoxide is facile and non-dissociative under normal catalytic conditions. The reaction has served to increase the understanding of the redox mechanism of catalytic oxidation, as well as helping to verify the electronic theory of chemisorption on catalysts. The revival in the study of this field has been underpinned by the development of new, high-powered surface science techniques, which have offered new insight into chemisorbed species and the molecular model of carbon monoxide oxidation. Such is its importance to fundamental catalysis principles that it is still under much scrutiny, even today [30].

1.5.1 Noble Metal Catalysts

From an industrial point of view, the development of an efficient auto-motive gas catalyst drew attention to the study of CO Oxidation. In the 1970s, in fact, car manufactures needed to develop a catalyst with an ambitious goal: achieve in the same reactor the conversion of three major pollutants: CO and hydrocarbons (HC) by oxidation and nitrogen oxides by reduction. Many studies at that time were devoted to analyze CO Oxidation reaction on model catalysts based on Pt, Pd, or Rh deposited on alumina and/or ceria-doped oxides [31], both in Universities and private research laboratories.

1.5.1.1 Alumina- or silica-supported

One of the first systematic studies of CO oxidation carried out over model “three-way” catalysts was reported by Yu Yao in 1984, working for Ford Motor Company [32]. A first series of alumina-supported Pt, Pd, and Rh catalysts was prepared with metal dispersion ranging between 6 and 87% by varying the sintering temperature. The CO oxidation reaction was carried out in the 200–300°C temperature range in oxygen excess (0.5% CO+0.5% O₂). Plotting the turnover frequencies at 250°C against the metal dispersion, Yu Yao found that the reaction is slightly structure-sensitive, with TOFs increasing with particle size. Rh and Pd appeared more active than Pt but the latter also results to be the least structure-sensitive for this reaction. This was in agreement with Cant who, in 1980, studied the particle size effect on a series of Pt/SiO₂ catalysts with metal dispersions of 6 to 81%, finding small TOF variations for the whole series [33]. For particle sizes of 1–67 nm, Oh and Eickel found a TOF virtually constant at 155°C over Rh/Al₂O₃ catalysts (1% CO+1%O₂) [34].

1.5.1.2 Ceria-supported

Cerium Oxide was added to automotive depollution catalysts for its oxygen storage properties. It allows the metallic active phase to compensate oxygen fluctuation, thus improving its performance in transient regime, especially when the oxygen pressure in gas phase decreases below the stoichiometry [35–37]. In addition, ceria is able to promote the CO water–gas shift reaction and hydrocarbons steam reforming [38], and inhibits metals sintering [31,39–41]. In his study on CO oxidation over noble metals catalysts, Yu Yao found the impact of ceria on the kinetics of reaction to be different than the one previously found for alumina [32]. The addition of ceria decreases the oxygen kinetic order, which tends to zero, while the kinetic orders with respect to CO become positive, whereas they were negative over M/Al_2O_3 catalysts. This findings were interpreted as the result of a cooperative effect between metals and ceria (dual-site mechanism) particles, with the former being responsible for carbon monoxide adsorption and the latter for oxygen activation. The significant effect of ceria on CO oxidation was confirmed in many further studies [42–47] which agree on the following findings:

- the support/metal interface plays a crucial role: ceria active sites neighboring metal particles have lower activation energy (23 kJ/mol), being more active than the ones located on the support (44 kJ/mol) [43];
- the reaction is very sensitive to the metal state: different pretreatment can lead to large variations in activity [45], significantly affecting the CO conversion during transient regime [48].

1.5.1.3 Gold-Based

Initially considered chemically and catalytically inert, materials based on gold represent some of the best catalysts for CO oxidation at or below room temperature. Since the initial discovery by Japanese chemist Masatake Haruta that small ($d < 5$ nm) nanoparticle deposits of gold on TiO₂ are catalytically active for CO oxidation [49,50], many theories have been proposed for explaining this surprising catalytic activity. Despite the lack of a general consensus, there are a number of phenomena that most researchers in the field agree upon. These include the observations that bulk forms of gold are not active, that the highest rates are found for gold nanoparticles 2-3 nm in diameter supported on transition-metal oxide supports and that the method of depositing and annealing the gold is critical for achieving good performance [51,52]. Disagreement in the literature include the identification of the active site or interface, whether the support has a direct role in catalysis and the mechanism for the catalytic turnover. Furthermore, the recorded activation energies and kinetic orders vary from study to study. The heterogeneity reported in literature therefore reflect the complexity and the inherent difficulty in fully understanding catalytic reactions in two-phase systems [52].

1.5.2 Metal Oxide Catalysts

The literature on CO oxidation over metal oxide catalysts can be divided into two distinct periods: a) A great interest of the researchers for this kind of materials up to 1975–80, before noble metal catalysts definitively imposed their supremacy in automotive exhaust gas catalysis; b) recent interest for these oxide catalysts for stationary applications [volatile organic compound (VOC) abatement] and for the substitution of noble metals by less costly materials. The main reason for their withdrawal from catalytic converter formulations was their undesirable behavior in

cycled transient conditions and their high susceptibility to deactivation by sulfur and water. The huge decrease in sulfur content in fuels and progress in oxide catalyst synthesis, have allowed metal oxides to be reconsidered for practical applications. A high-throughput investigation by Saalfrank and Maier in 2004 documented the very good results obtained on noble metal-free catalysts [53].

1.5.2.1 Cobalt oxides

The most active form of cobalt oxide is Co_3O_4 which is also the most stable form between 350°C and 900°C . Activities in CO or hydrocarbon oxidation of different unsupported Co_3O_4 catalysts were investigated by Yu Yao in 1974. This early results for CO oxidation showed that intrinsic activity was only slightly affected by sample BET surface area, indicating that the reaction is structure insensitive for this materials. The coexistence of Co^{2+} - Co^{3+} pairs in the same materials seems to be essential for the Co^{3+} ion catalytic activity, despite Co^{2+} ions alone being inactive for the reaction [54]. The most active samples showed TOFs values comparable to the one of noble metals, but also presented negative reaction order for water. In fact, the addition of steam to the reaction mixture shows a severe inhibitory effect on the reaction. For example, Yu Yao reported that addition of 0.45% H_2O decreased the activity from 21 to $0.6 \text{ mmolCO}_2\text{s}^{-1}\text{m}^{-2}$ [54]. The same effect was confirmed by Grillo et al. in a diffuse-reflectance infrared Fourier transform (DRIFT) spectroscopy study [55]. Water inhibitory effect was not observed over noble metals, and, since gas exhaust fumes contain about 10% of steam in their composition, this systems were preferred over cobalt oxide ones. Yu Yao also showed that Co_3O_4 was extremely sensitive to SO_2 poisoning, a few ppm of SO_2 being sufficient to completely deactivate the catalyst at low temperature.

Further attempts to overcome these problems were made by supporting cobalt oxide on different materials. A series of samples were prepared by Yao et al. [54] by impregnating γ -Al₂O₃ with acid cobalt salts but showed no increase in activity. Years later, using basic salt precursors, Jansson [56] was able to prepare a very active catalyst. The Co₃O₄/ γ -Al₂O₃ system he synthesized can convert carbon monoxide at very low temperature, but suffers CO poisoning at temperatures below 50°C.

Sample supported on silica gave poor performances in CO oxidation due to the poor interaction between silica and cobalt oxide [54]. To solve this, Lopes et al. tried to prepare catalysts in which Co₃O₄ nanoclusters were inserted in the mesopore of SBA-15. Promising results were obtained, but the activity of the Co₃O₄ clusters extracted from the mesoporosity of SBA-15 was higher than that of Co₃O₄/SBA-15, probably due to diffusion effects inside the mesoporous silica structure [31,57]. Cerium oxide [58–60] is able to improve the CO oxidation activity of the supported cobalt oxide [31], along with improving its resistance towards water inhibition. In fact, Kang et al. [58] showed that CoO_x/CeO₂ was not inhibited by addition of 2% H₂O to the reaction mix [31].

1.5.2.2 *Copper oxides*

In comparison to Co₃O₄, unsupported copper oxides have been more rarely used in CO oxidation [31]. As previously said, cobalt oxide derives its activity from the co-existence in its structure of both Co²⁺ and Co³⁺. On the contrary CuO or Cu₂O have only either Cu²⁺ or Cu⁺ ions respectively, but their oxidation state may vary in the course of reaction, due to their poor stability [61]. Depending on the reducing/oxidizing power of the reaction atmosphere, it is highly probable that Cu²⁺ and Cu⁺ (and even Cu⁰) coexist. Jernigan and Somorjai investigated the CO oxidation reaction over well-defined thin

films of Cu^0 , Cu_2O , and CuO between 200 and 350°C by surface science techniques [62]. Metallic copper was shown to be more active than copper oxides but, at 275°C, its complete oxidation to the less active Cu(II) oxide at CO/O_2 ratio below 67:33, strongly limits the material working range.

Recently, Sadykov et al. revisited most of the previous studies pointing out that copper films are not suited for the study of CO Oxidation over CuO_x [63]. In fact, employing electrochemical techniques, high-resolution electron microscopy (HRTEM) and FTIR spectroscopy, these authors showed that Cu^+ cations located at outlets of extended defects (grain boundaries) would be the most active sites for CO oxidation at 25°C. They also commented that, at ambient temperature, the oxygen replenishment from subsurface layers by conventional diffusion process would be too slow, whereas diffusion along grain boundaries can lead to very fast oxygen diffusion [31,63,64]. The great reactivity of Cu_2O was confirmed by other authors, both experimentally [65] and by DFT calculations [66].

In the 1970s, researchers were already able to demonstrate the positive influence of support on copper reactivity in terms of active phase stabilization [67], activity [68] and resistance to SO_2 deactivation [69]. More recent studies, conducted by Choi and Vannice, [70] Huang et al. [71,72] and Laine, Lòpez-Agudo and co-workers [73–77], focused their attention on alumina-supported copper catalysts, to improve the understanding of these materials. Despite focusing on different aspects of the carbon monoxide catalytic oxidation, they all conclude that reduced species of copper (Cu^0 , Cu^+) are required for good oxidation activity, highlighting the crucial role of reducing pre-treatment to stabilize the required active species [31].

Ceria-supported copper oxide shows very good performance in CO Oxidation, probably related to the exceptional OSC of CuO_x/ceria systems [78]. However, the outstanding performance of this catalytic system in CO Preferential Oxidation (CO-PROX), drawn most of the scientific attention towards its application in this field [79,80].

1.5.2.3 Manganese oxides

Many studies have been devoted to bare manganese oxides [81,82,91,83–90], only in rare cases supported on other materials [92]. In some of this studies, manganese oxides were also promoted by metals such as palladium [81,82,86,93], gold [85,90,92], or silver [84].

Three types of manganese oxides are generally used for the CO oxidation: MnO₂, Mn₃O₄, or Mn₂O₃. Wang et al. compared the catalytic behavior of the three manganese oxides, doped or not by gold, finding that Mn₂O₃ is the most active oxide, reducing at the lowest temperature. In accordance, Imamura et al. found similar high activity for the same manganese oxide, employed as a support in their formulation (Pd/Mn₂O₃). Its role would be to incorporate oxygen from the gas phase, which is subsequently withdrew from Pd active site, where the actual surface oxidation takes place [31,81].

Given its excellent electrochemical properties and its use in batteries and supercapacitors, MnO₂ has been the subject of numerous investigations. It forms four kinds of polymorphs, denoted as α -, β -, γ -, and δ -MnO₂ [83]. α and δ -MnO₂ were found to be the most active phases for CO oxidation, whereas γ and β -MnO₂ are much less active [83]. The order of activity is well-correlated to the Mn–O bond strength ($\alpha < \delta < \gamma < \beta$); the higher the Mn–O bond strength, the lower the activity. Liang et al. suggested that the reactivity of MnO₂ would be related to the constant oscillation

between Mn^{4+} and Mn^{3+} . This could explain the lower performance of γ - and β - MnO_2 since the re-oxidation of Mn^{3+} into Mn^{4+} in this polymorphs would be more difficult than in α - and δ - MnO_2 . A recent study on MnO_2 oxide was published by J-H Park et al. [91]. In their work, the Korean team compares the performance of a series of sample prepared by a redox method, using different precursors. The different salts employed, not only affected the physicochemical properties of the catalysts, but also their reducibility and quantity of liable oxygen species. These two factors were recognized as the main contributors to the catalytic performance of the MnO_2 catalyst.

Morgan et al. [90] prepared Au-doped and bare CuMnO_x (Hopcalite), to analyze the mechanism of CO Oxidation reaction using a temporal analysis of products (TAP) reactors. Both samples showed a larger contribution of the *Mars van Krevelen* mechanism and a smaller contribution of the *Langmuir–Hinshelwood* mechanism. Gold doping does not significantly affected the L-H mechanism contribution, whereas it clearly promotes the *Mars van Krevelen* mechanism compared with the undoped CuMnO_x catalyst which led to an overall CO oxidation activity increase of the 0.5% for the Au-doped CuMnO_x catalyst [90].

Cerium effectively promotes reactivity and chemical stability of MnO_x catalysts, although oxide dispersion and interaction pattern affect structure and reactivity of composite MnCeO_x materials [94,95]. Thus, special synthesis routes have been devised to improve the functionality of MnCeO_x systems [93,94,96–102], while recent computational studies addressed physico-chemical and catalytic properties of surface Mn ions adsorbed on ceria surface [103,104]. Despite quantum-chemical evidences on model systems predict high mobility of oxygen-bridge species and a superior O^{2-}

activation capability of the Mn-doped ceria surface [103,104], structural and/or electronic effects shape the functionality of “real” MnCeO_x catalysts [94,96–98,105,106]. In particular, compositions corresponding to manganese-to-cerium atomic ratios in between 0.3 and 2.0 generally ensure the best performance [93,94,96–98,107], while highly Mn-loaded catalysts have been scarcely investigated also in spite of the economic advantages due to lower cerium content in catalyst formulation [108].

Our research group focused its attention on manganese oxides [109] and their redox behavior since 2001, but it was only in 2007 that a preparation method including cerium oxide in the formulation was proposed. Named “redox-precipitation” method, it leads to a (quasi)molecular dispersion of the active phase and enhanced textural properties in comparison to the standard coprecipitation synthesis [102]. The unique properties attained by the employment of the redox-precipitation method [102,110] led the group to exploit its performance in different oxidation reaction, both in liquid [99,100,106,111,112] and gas [97] phase [94]. The improved reactivity in the CO oxidation reaction, compared to coprecipitated sample, was ascribed to high MnO_x dispersion and very effective MnO_x - CeO_2 interaction, enhancing the oxidation strength and stability [97].

Zou et al., recognized the formation of a solid solution as a possible explanation for the superior activity of the sample they prepared in 2010. With a Mn/Ce ratio of 4/6 being the optimum for the series analyzed, the oxidation performance of the catalysts seems to be dependent on the formation of highly active oxygen species on the interface oxygen vacancies between cerium and manganese. The catalytic system is characterized by a mixture of different oxidation state both for Mn (I,III and IV) and Ce (III and IV) [93].

In 2015 Zhang et al. synthesized a mesoporous MnCeO_x system ($\text{Mn}_{0.5}\text{Ce}_{0.5}\text{O}_x$) which showed great activity either for CO total oxidation and for hydrocarbons selective oxidation (i.e. cyclohexane conversion to KA oil). In this case, structural effects play a crucial role since the authors attributed the outstanding performance of the MnCeO_x system to the formation of a solid solution between manganese and cerium oxides: in fact, the introduction of Mn^{4+} ions into ceria matrix for the formation of maximum solid solution phases can lower the energy for oxygen vacancy formation and facilitate the rapid migration of oxygen vacancies from the bulk to the surface, thus continuing the activation of gas oxygen molecules [96].

In the same year, another group synthesized a $\text{Mn}_{0.7}\text{Ce}_{0.3}\text{O}_x$ solid solution by a simple coprecipitation method. Venkataswamy et al. explained the superior CO oxidation activity by the strong synergistic effect between MnO_x and CeO_2 species and the improvement in redox properties of ceria, facilitating the formation of surface oxygen vacancies leading to the availability of active oxygen for CO oxidation. Opposed to what Zhang et al. reported on the significant role of Mn^{4+} ions in the ceria lattice, such ionic species were not detected in this sample. The observed remarkable enhancement in the reactivity for CO oxidation at lower temperatures has been, conversely, attributed to a highly dispersed state of $\text{Mn}^{2+}/\text{Mn}^{3+}$ in the ceria matrix [113].

A survey of the most recent literature data in terms of catalytic activity is presented in Table 2

Table 2. Literature CO₂ yield data of bare and promoted MnO_x catalysts at various temperatures.

Catalyst Composition	F (mL·min ⁻¹)	Reaction mixture composition (%)	W _{cat} (g)	F _{mol} (mol _{CO} ·g _{cat} ⁻¹ ·s ⁻¹) 1)	X _{CO} ^b (%)	Y _{CO2} ^b (mol _{CO2} ·g _{cat} ⁻¹ ·s ⁻¹)	T ^b (K)	Ref.
Mn _{0.5} Ce _{0.5} O _x	10	CO (1.0) – Air (99.0)	0.03	2.3·10 ⁻⁶	100	2.3·10 ⁻⁶	≈373	[96]
Mn _{0.3} Ce _{0.7} O _x	50-60	CO (1.0) – O ₂ (1.0) – Ar (98.0)	0.10	4.2·10 ⁻⁶	100	4.2·10 ⁻⁶	≈473	[113]
MnO ₂	200	CO (1.0) – O ₂ (4.0) – N ₂ (95.0)	0.10	1.4·10 ⁻⁵	100	1.4·10 ⁻⁵	≈473	[91]
MnO _x	50.0	CO (2.0) – O ₂ (2.0) – Ar (96.0)	0.14	5.0·10 ⁻⁶	≈14	7.0·10 ⁻⁷	≈298	[89]
MnO _x	50.0	CO (2.0) – O ₂ (2.0) – Ar (96.0)	0.14	5.0·10 ⁻⁶	100	5.0·10 ⁻⁶	≈423	[89]
Mn _{0.4} Ce _{0.6} O _x	250 ^a	CO (2.0) – O ₂ (10.0) – N ₂ (88.0)	0.50	6.9·10 ⁻⁶	100	6.9·10 ⁻⁶	≈373	[93]
CuMnO _x	22.5	CO (1.0) – O ₂ (89.0) – He (10.0)	0.10	1.6·10 ⁻⁶	25	4.0·10 ⁻⁷	298	[90]
Au/CuMnO _x	22.5	CO (1.0) – O ₂ (89.0) – He (10.0)	0.10	1.6·10 ⁻⁶	55	8.8·10 ⁻⁷	298	[90]
Mn _{0.5} Ce _{0.5} O _x	100	CO (8.0) – O ₂ (4.0) – He (88.0)	0.03	1.8·10 ⁻⁴	≈2	2.9·10 ⁻⁶	373	[97]
Mn _{0.5} Ce _{0.5} O _x	100	CO (8.0) – O ₂ (4.0) – He (88.0)	0.03	1.8·10 ⁻⁴	≈4	5.9·10 ⁻⁶	393	[97]
Mn _{0.5} Ce _{0.5} O _x	100	CO (8.0) – O ₂ (4.0) – He (88.0)	0.03	1.8·10 ⁻⁴	≈9	1.4·10 ⁻⁵	423	[97]

2. MATERIALS AND METHODS

2.1 Catalysts Preparation

2.1.1 Redox-precipitation Method

The redox-precipitation preparation technique allows an intimate mixing of the oxide phases generated during the synthesis process, leading to a noticeable improvement of the chemical-physical properties compared to other more conventional methods such as co-precipitation [97]. Having already shown excellent performances in catalytic oxidation processes such as CWAO and the selective conversion of benzyl alcohol to benzaldehyde, it has been employed in this thesis work with the aim of deepening the motivations behind its exceptional oxidative behavior.

Bare (M) and cerium (MxCy) promoted MnO_x catalysts with different atomic ratios (Mn/Ce, x/y) were prepared *via* the acidic protocol of the *redox-precipitation* route [101,112], according to the following procedure. Deionized water (150 mL), at pH≈4.5 by HNO₃ addition, was heated at 343K under stirring, adding the proper amounts of the Mn(NO₃)₂·4H₂O (>97%, *Carlo Erba*) precursor. This was then titrated (343K) by the dropwise addition of an aqueous solution (200 mL) of the KMnO₄ (>99%, *Carlo Erba*) and Ce(NH₃)₂(NO₃)₆ (>98.5%, *Aldrich*) precursors (pH≈1), keeping a constant pH (4.5±0.5) by 0.1 M KOH solution additions. The occurring reactions are:

1. $\text{MnO}_4^- + 3\text{e}^- + 2\text{H}_2\text{O} \rightarrow \text{MnO}_2(\downarrow) + 4\text{HO}^-$
2. $\text{Mn}^{2+} + 4\text{HO}^- \rightarrow \text{MnO}_2(\downarrow) + 2\text{e}^- + \text{H}_2\text{O}$
3. $\text{Ce}^{4+} + 4\text{OH}^- \rightarrow \text{CeO}_2(\downarrow) + 2\text{H}_2\text{O}$

Thereafter the solids were digested overnight, filtered and washed with a large amount of hot deionized water (2 L, 343K) to remove K^+ ions coming from the precursors. The sample was subsequently dried at 373K (16h) and calcined at 673K (6h).

The bare CeO_2 (C) sample was obtained via an analogous experimental protocol, precipitating at the same pH the above ceria precursor.

The designed catalysts were synthesized by dosing the amount of the various precursors, according to the quantitative relationships provided by the following equations system:

$$2 \cdot mol_{Mn^{VII}} = 3 \cdot mol_{Mn^{II}} \quad (1)$$

$$\frac{mol_{Mn^{VII}} + mol_{Mn^{II}}}{mol_{Ce^{IV}}} = \left(\frac{Mn_{at}}{Ce_{at}} \right)_{design} \quad (2)$$

$$mol_{Mn^{VII}} + mol_{Mn^{II}} + mol_{Ce^{IV}} = 1 \quad (3)$$

referring to the electron (1) and mass (3) balances and the designed catalyst composition (2), respectively [101].

2.2 Catalyst Characterization

2.2.1 X-ray fluorescence (XRF)

The analytical composition of the investigated systems was determined by XRF measurements, using a *Bruker AXS-S4 Explorer Spectrometer*. The elements concentration was determined by the emission value of $K_{\alpha 1}$ transitions of Mn (5.9 keV) and Ce (4.8 keV).

2.2.2 N₂ physisorption isotherm (SA, PV, APD)

N₂-physisorption isotherms were obtained at 77K using an *ASAP 2010* static adsorption device (*Micromeritics Instrument*). The samples were outgassed at 423K until reaching a residual pressure lower than 0.01 atm. The isotherms were elaborated in the p/p⁰ range of 0-0.2, according to the B.E.T. (*Brunauer, Emmett and Teller*) method for the determination of the amount of N₂ adsorbed on the “monolayer” (V_m) for surface area determination. Pore size distributions and average pore diameter were obtained, using the B.J.H. (*Barrett-Joyner-Halenda*) method for mesopore evaluation.

2.2.3 X-ray diffraction (XRD)

X-ray Diffraction (*XRD*) analyses of powdered samples were performed by a *Philips X-Pert diffractometer* operating with a Ni β-filtered Cu K_α radiation (40kV; 30mA) in the range of 2θ = 10°-80° with a scan step of 0.05 deg/s. The crystallite size (*d*) of the ceria matrix was calculated using the Scherrer's equation:

$$d = \frac{K \cdot \lambda}{\beta \cdot \cos\theta} \quad (4)$$

where K is a constant equal to 0.92 for spherical shape, λ is equal to 1.5406 Å, β is the width of the main peak of the diffractogram and θ the relative position of the maximum after baseline subtraction. Peaks were then identified on the base of the JCPDS database for reference compounds.

2.2.4 Laser Raman Spectroscopy (RS)

Laser Raman Spectroscopy (RS) analyses were performed using a laser wavelength of 632.8 nm (He-Ne) at a power of 0.03 mW, focused on the sample by a 50× objective at long focal distance over a 1.5 μm diameter spot. Measurements were carried out on the “as prepared” samples, and after laser annealing at higher laser power (3 mW; 30 s)

under the same conditions. The signal, collected by a microscope (*Olympus BX41*) in the back-scattering configuration, was dispersed by an HR800 monochromator (*Horiba-Jobin Yvon*) and detected by a Peltier-cooled silicon charge-coupled device (CCD) array sensor (*Synapse, Horiba-Jobin Yvon*), with a resolution of ca. 3 cm⁻¹.

2.2.5 X-ray Photoelectron Spectroscopy (XPS)

X-ray Photoelectron Spectroscopy (XPS) data were obtained using a *Physical Electronics GMBH PHI 5800-01* spectrometer operating with a monochromatized Al-*K_α* radiation with a power beam of 300W. The pass energy for determination of the oxidation state and concentration of surface species was 11.0 eV and 58.0 eV, respectively. The BE regions of C_{1s}-K_{1s} (280-300 eV), Mn_{2p} (635-680 eV), Ce_{3d} (870-935 eV), and O_{1s} (525-535 eV) were investigated, taking the C_{1s} line (284.8 eV) of adventitious carbon as reference.

2.2.1 Temperature programmed reduction (TPR)

Temperature Programmed Reduction (TPR) measurements in the range of 293-1073K were carried out using a linear quartz microreactor (i.d., 4 mm) heated at the rate of 12K/min and fed with 5% H₂/Ar and 5% CO/He (CO-TPR) carrier flowing at 60 stp mL/min. The analyses were performed using catalyst samples of 20 mg after an in situ pretreatment under a 5% O₂/He flow at 423K (1h). The amount of catalyst was calculated to respect the following P parameter:

$$P = \frac{\beta \cdot S \cdot n}{F \cdot C} \quad (5)$$

where β is the heating rate (12 K/min), S the fraction of reducible species present in the catalyst, n the stoichiometry of H₂ or CO consumption, F the reducing flux (ca. 60 stp mL/min), C the fraction of H₂ or CO in the reducing flux (5% H₂/Ar or 5% CO/He mixtures). The consumptions of the reducing agents were monitored by a TCD after

removing water and carbon dioxide by a trap containing $\text{Mn}(\text{ClO}_4)_2$ and ascarite, respectively [112].

2.2.2 Temperature Programmed Desorption (TPD)

Temperature Programmed Desorption (TPD) measurements were carried out in the above apparatus, using He as carrier gas (60 stp mL/min) and a heating rate of 12K/min. Pretreated catalyst samples (20 mg) were cooled at r.t. (298K) and further treated under 5% CO/He, CO/O₂/He ($p_{\text{CO}}=p_{\text{O}_2}$, 0.025 atm) or 10% CO₂/He flow for 1h. Thereafter, the catalyst was flushed by the carrier gas and, after baseline stabilization, the (m/z) signals of He (4), H₂O (18), CO (28), O₂ (32) and CO₂ (44) were recorded by a QMS (*Hidden Analytical*, HPR 20), operating in MID mode with the SEM amplifier at 1,200V [95].

2.2.3 Steady-state O₂ uptake measurements

Steady-state O₂ uptake measurements were performed in pulse mode after catalyst (20 mg) exposure to the He/CO/O₂ reaction mixture (CO/O₂, 0.25-3.3) at 393K for 1h. After flushing by the He carrier (35 stp mL/min), very small O₂ pulses ($2.7 \cdot 10^{-9}$ mol_{O₂}) were injected, with **no consumption** being recorded, irrespective of the reaction mixture composition.

2.2.4 Surface Oxygen Content (SOC) Measurements

The Surface Oxygen Content (SOC) of the catalyst was determined by KI titration method [114]. 0.2 g of the M5C1 catalyst and 2 g potassium iodide were added to 15 mL of buffer solution (pH 7.1) and vigorously stirred in nitrogen atmosphere for 30 minutes. The reaction mixture was then filtered, acidified with 1M HCl and the liberated iodine was titrated against 0.1M sodium thiosulfate solution using starch as an

indicator. The SOC of the M5C1 sample, as an average of three independent measurements, resulted equal to $6.3 \cdot 10^{-3} \text{ mol}_O/\text{g}_{\text{cat}}$.

2.3 Catalyst Testing

2.3.1 Temperature programmed catalytic reaction (TPCR) test

CO oxidation activity has been probed by temperature programmed catalytic reaction (TPCR) measurements. In a typical test, the employed quartz microreactor was heated at the rate of 4K/min in the range of 293-533K. A CO/O₂/He (1/1/38) mixture ($p_{\text{CO}}=p_{\text{O}_2}$, 0.025 atm; P, 1 atm) was fed at the rate of 60 stp mL/min using a Mass Flow Controller (*Brooks Instruments*). The catalyst bed was composed of 20 mg powdered catalyst ($d_p < 0.1 \text{ mm}$) diluted (1/15, wt/wt) with granular SiC ($L_b \approx 20 \text{ mm}$), and its temperature controlled by a K-type internal thermocouple. A direct contact between the thermocouple and the catalyst bed is a necessary precaution to ensure a “realistic” reading of the temperature since the studied reaction is exothermic. Before tests, all the catalysts were pre-treated under a 5% O₂/He flow at 423K (1h). The output stream was collected through a heated capillary and analyzed by a QMS.

Pulse CO oxidation tests were carried out at 393K injecting five consecutive CO pulses ($1.3 \text{ } \mu\text{mol}_{\text{CO}}$) on the catalyst (20 mg) kept under 5% O₂/He carrier (35 stp mL/min) and, then, other five pulses under He flow. The CO and CO₂ signals were acquired by the QMS.

2.3.2 Quadrupole Mass Spectrometer (QMS)

Mass spectrometry (MS) is an analytical technique that ionizes chemical species and sorts the ions based on their mass-to-charge ratio. The roots of this technique lies in the late 19th century pioneering studies on anode rays by Eugen Goldstein and successive

discoveries by J. J. Thomson in 1913 [115,116], but only in 1918 Arthur Jeffrey Dempster [117] reported on his mass spectrometer and established the basic theory and design of mass spectrometers that are still used to this day. Since then, mass spectrometry has been used in many different fields and applied to pure samples as well as complex mixtures [118].

In a typical Mass Spectrometer, a sample, which may be solid, liquid, or gas, is ionized by an ion source. There is a wide variety of ionization techniques, depending on the phase of the sample and the ionization efficiency required. This usually causes some of the sample's molecules to break into charged fragments. These ions are then accelerated by an electric field and deflected by a perpendicular magnetic field. Fragments with different mass-to-charge ratio will follow different trajectories, according to Lorentz force law:

$$F = Q(E + v \times B) \quad (6),$$

and Newton's second law:

$$F = m \cdot a \quad (7),$$

where \mathbf{F} is the force applied to the ion, \mathbf{m} is the mass of the ion, \mathbf{a} is the acceleration, Q is the ion charge, \mathbf{E} is the electric field, and $\mathbf{v} \times \mathbf{B}$ is the vector cross product of the ion velocity and the magnetic field. The above equations, combined, lead to the next one:

$$(m/Q)a = E + v \times B \quad (8),$$

which, together with the particle's initial conditions, completely determines the particle's motion in space and time in terms of m/Q .

Following different paths, as shown in Figure 5, the ions are then detected by a charged particles detecting mechanism, such as an electron multiplier or an ion-to-photon detector. Results are displayed as spectra of the relative abundance of detected ions as a function of the mass-to-charge ratio. The atoms or molecules in the sample can be identified by correlating known masses (e.g. an entire molecule) to the identified masses or through a characteristic fragmentation pattern.

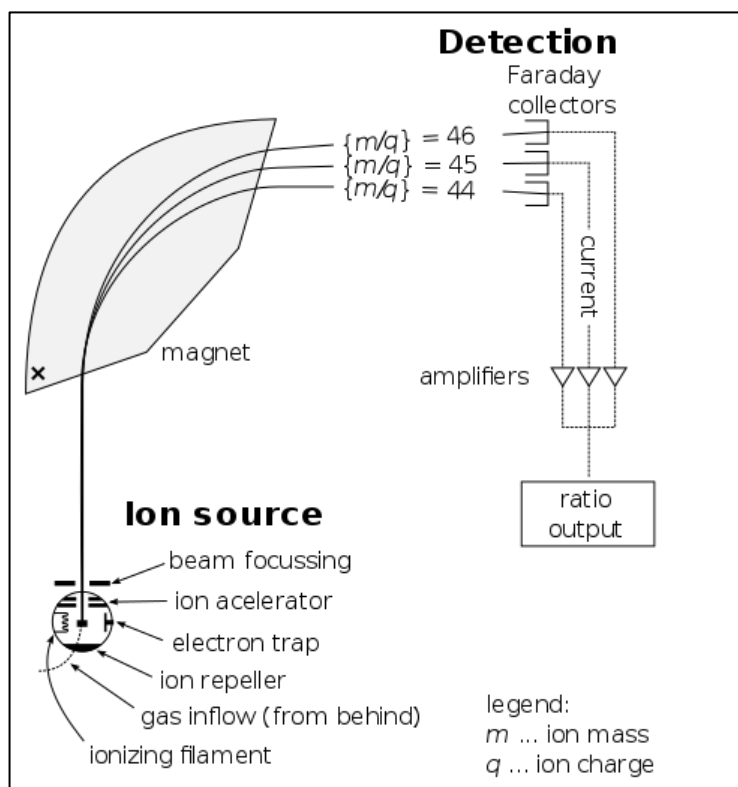


Figure 5. Schematics of a simple mass spectrometer with sector type mass analyzer.

The quadrupole mass spectrometer (QMS) is one type of mass analyzer used in mass spectrometry. The quadrupole mass filter was patented by Wolfgang Paul and co-workers at the University of Bonn, in the 1950s and nowadays is the most common analytical mass spectrometer in use. A mass filter consists of a square parallel array of four round (rather than the ideal hyperbolic form) rods to which a radiofrequency (rf) potential is applied such that opposite rods are held at the same potential and adjacent

rods are out-of-phase by 180° (Figure 6) [119]. In a quadrupole mass spectrometer, the quadrupole is the *mass analyzer* - the component of the instrument responsible for selecting sample ions based on their mass-to-charge ratio (m/z). Ions are separated based on the stability of their trajectories in the oscillating electric fields that are applied to the rods [120]. In fact, only ions of a certain mass-to-charge ratio will reach the detector for a given ratio of voltages: other ions have unstable trajectories and will collide with the rods. This allows selection of an ion with a particular m/z or to scan for a range of m/z -values by continuously varying the applied voltage [120].

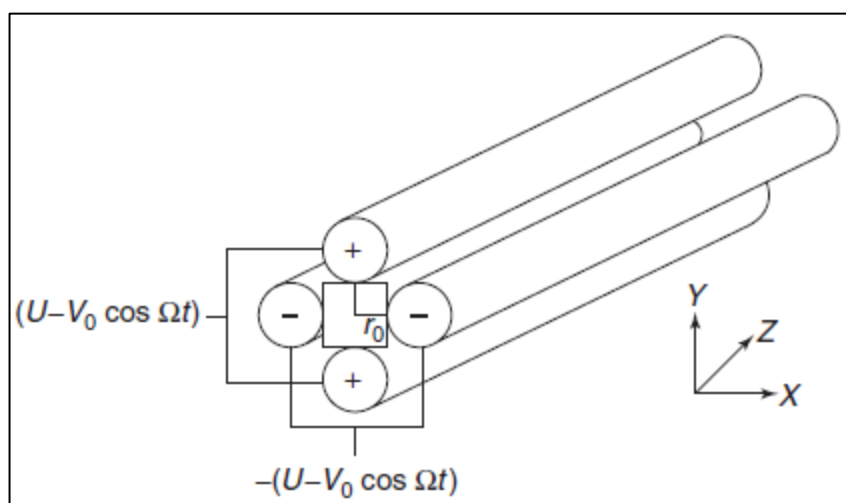


Figure 6. Schematic diagram of quadrupole with adjacent rods out-of-phase by 180° [119].

The quadrupole ion trap is an extremely versatile mass spectrometer, capable of multiple stages of mass selectivity (e.g tandem mass spectrometry and MS/MS), high sensitivity, mass resolution, and mass range [119]. Its use in the catalysis field allows an on-line analyses of the reaction streams of the catalytic reactions, making it particularly appropriate for TPCR [121,122].

In this thesis, the output reaction streams were analyzed by acquiring the signals of He, H₂O, CO, O₂, and CO₂ in MID mode. Helium was used as internal standard and a

correction factor for CO (m/z , 28) of 10% of the CO₂ signal (m/z , 44) was necessary, due to partial fragmentation of CO₂ molecule.

3. RESULTS AND DISCUSSION

3.1 Results and Discussion Outlines

The **Results and Discussion** chapter includes three main paragraphs documenting the achievement of the following main objectives:

- the kinetic regime of the CO oxidation catalytic tests, carried out in the range of 293-533K in Temperature Programmed mode [121,122], scientific premise for assessing the reliability of forthcoming catalyst screening (Par.3.3) and reaction kinetics studies (**3.2 *The Kinetic Regime of CO Oxidation Tests: theoretical and experimental evaluations***);
- probing the effects of the ceria promoter on the structural properties and reactivity pattern of the active MnO_x phase for ascertaining some fundamental structure-activity relationships and highlighting the nature of active sites of the nanocomposite MnCeO_x catalysts (**3.3 *Effect of Cerium on the Reactivity Pattern of Composite MnCeOx Catalysts and Nature of Active Sites***);
- study of the empiric reaction kinetics and mechanistic issues of the CO oxidation reaction on a model MnCeO_x (i.e., M5C1) catalyst, for the formulation of a plausible reaction mechanism and the relative kinetic equation. The ultimate aim of this work is the prediction of the reactivity pattern in a wide range of experimental conditions in terms of temperature (293-533K), reagents pressure (p^0_{CO} - $p^0_{O_2}$, 0.00625-0.025 atm) and CO/O₂ ratio (λ_0 , 0.25-4.0) (**3.4 *Kinetic and Mechanistic Evidences***).

3.2 The Kinetic Regime of CO Oxidation Tests: Theoretical and Experimental Evaluations

3.2.1 Reliability and reproducibility of catalytic data

Catalytic activity data in the CO oxidation in the range of 293-533K were obtained in Temperature Programmed mode (TPCR, Temperature Programmed Catalytic Reaction), using a heating rate of 2K/min and a QMS for the continuous analysis of the reaction stream. Previous studies have in fact shown that the TPCR technique is a powerful and reliable method to accelerate the work of catalyst testing by orders of magnitude in comparison to conventional steady-state measurements [121,122]. The method is quite reliable for both catalyst screening and reaction mechanism studies, provided that the experimental conditions ensure ideal kinetic conditions, free of whatever diffusional resistance [121]. Considering the absolute relevance of this point, experimental measurements and theoretical calculations have been performed to document the kinetic regime of catalytic tests, in the whole range of temperature (293-533K) and conversion (0-100%).

First, the reliability of data is demonstrated by the analysis of the conversion values, obtained in a typical TPCR test of the M5C1 catalyst under standard conditions (F_{mix} , 60 stp mL/min; p_{CO}^0 , 0.025 atm; $p_{\text{O}_2}^0$, 0.025 atm; w_{cat} , 20 mg; d_p , 0.05 mm; β , 4K/min). In particular, CO conversion data (i.e., X_{CO}), calculated using both the *internal standard* and *mass balance methods*:

$$X_{IS} = 1 - \frac{(p_{\text{CO}}/p_{\text{He}})_T}{(p_{\text{CO}}/p_{\text{He}})_{273\text{K}}} \quad (9),$$

$$X_{MB} = \frac{(p_{\text{CO}_2})_T}{(p_{\text{CO}} + p_{\text{CO}_2})_T} \quad (10),$$

show a very good agreement proved by a constant $X_{CO(MB)}/X_{CO(IS)}$ ratio of 1 in the whole conversion range (Figure 7A).

Moreover, the overall intrinsic reliability of TPCR data is evident from the comparison of CO and O₂ conversion data, resulting in a constant ratio of 2 (i.e., $X_{CO(MB)}/X_{O_2(IS)}$, 2), as expected from a CO/O₂ feed ratio of 1 (i.e., $\lambda_0=1$).

Finally, the CO conversion profiles of two tests performed one year apart also document the excellent data reproducibility of the TPCR tests (Figure 7B) [95].

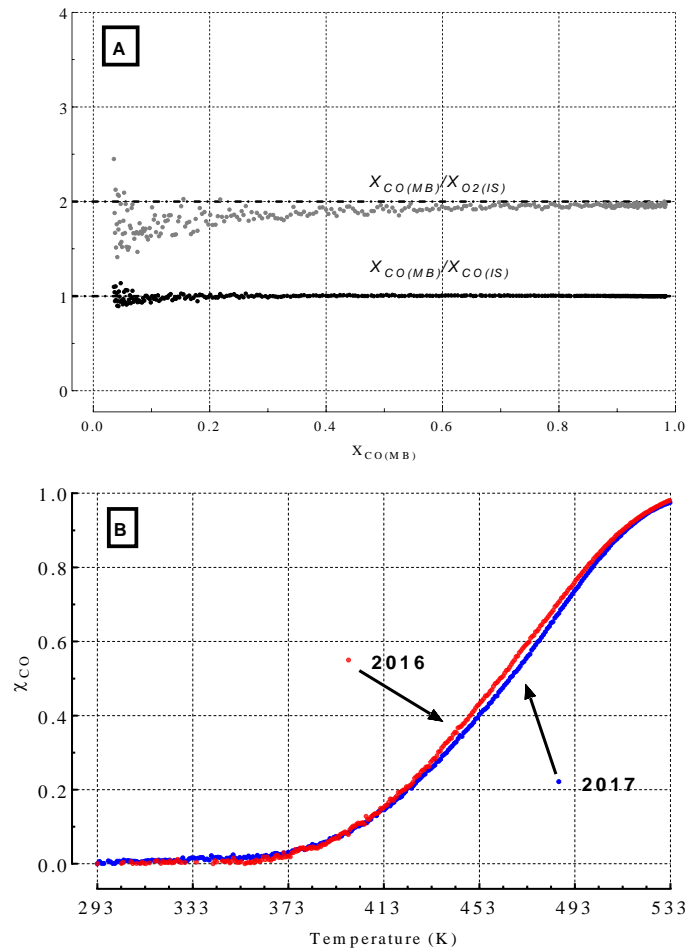


Figure 7. (A) Comparison of CO and O₂ conversion data by internal-standard and mass-balance methods ($X_{CO(MB)}/X_{CO(IS)}$) and CO-O₂ conversion values ($X_{CO(MB)}/X_{O_2(IS)}$) as a function of X_{CO} . (B) Comparison of CO conversion data of the same sample in 2016 (red line) and 2017 (blue line).

3.2.2 Theoretical evaluations of diffusional resistances

The lack of mass-transfer resistances on the reaction kinetics was assessed by theoretical criteria developed for the evaluation of external and internal diffusion and axial dispersion, respectively

<i>Resistance</i>	<i>Criterion</i>	<i>Relationship</i>	<i>Source</i>
<i>External diffusion</i>	<i>Mears</i>	$C_M = \frac{-r_{CO} \cdot \rho_b \cdot R \cdot n}{k_c \cdot C_{CO,b}} < \mathbf{0.15}$	a
<i>Internal diffusion</i>	<i>Weisz-Prater</i>	$C_{WP} = \frac{-r_{CO,obs} \cdot \rho_c \cdot R^2}{D_e \cdot C_{CO,s}} < \mathbf{1}$	a
<i>Axial Dispersion</i>	<i>Mears</i>	$\frac{L_b}{d_p} \geq \frac{20 \cdot n}{Pe} \cdot \ln\left(\frac{C_{in}}{C_{out}}\right)$	a

a) D.E. Mears, *Ind. Eng. Chem., Process Des. Dev.*, 1971, 10, 541.

where: $-r_{CO}$ is the reaction rate, $\text{kmol} \cdot \text{kg}_{\text{cat}}^{-1} \cdot \text{s}^{-1}$ ($4.2 \cdot 10^{-5} \text{ kmol} \cdot \text{kg}_{\text{cat}}^{-1} \cdot \text{s}^{-1}$); n the reaction order (1st); R the catalyst particle radius, m ($2.5 \cdot 10^{-5}$ m); ρ_b the bulk density of the catalyst bed, kg/m^3 ($900 \text{ kg}/\text{m}^3$); ε the porosity or void fraction of the packed bed (0.2); ρ_c the solid catalyst density, kg/m^3 ($3,300 \text{ kg}/\text{m}^3$); $C_{CO,b}$ the gas phase concentration of CO, being equal to the concentration at the catalyst surface if external diffusion is negligible (i.e., $C_{CO,s} = C_{CO,b}$); k_c the mass transfer coefficient, m/s; τ the tortuosity factor (4); σ_c , the constriction factor (0.5) and D_e the effective mass transfer coefficient, m^2/s , given by the formula:

$$\frac{1}{D_e} = \frac{1}{D_{CO/He,eff}} + \frac{1}{D_{Knudsen}}$$

where:

$$D_{CO/He,eff} = D_{CO/He} \cdot \varepsilon_p \cdot \sigma_c = 4 \cdot 10^{-6} \frac{\text{m}^2}{\text{s}} ; \text{ and } D_{Knudsen} = 19,400 \cdot \frac{\varepsilon_p^2}{\tau \cdot \sigma_c \cdot \rho_p} \cdot \sqrt{\frac{T}{P_{MCO}}} = 6 \cdot 10^{-7} \text{ m}^2/\text{s}$$

Considering a CO conversion of 80% at 463K and the following values of the experimental parameters:

Parameter	Experimental Value	Source
F (stp mL/min)	60 stp mL/min	exp. par.
Composition	He/CO/O ₂ =95/2.5/2.5	exp. par.
A.M.W. of reaction mixture	5.3 kg/kmol	exp. par.
d_{int} (m)	$4 \cdot 10^{-3}$ m	exp. par.
v_s (m/s)	$8 \cdot 10^{-2}$ m/s @ 298K	exp. par.
L_b	$2 \cdot 10^{-2}$ m	exp. par.
$D_{CO/He}$ (m ² /s)	$1.5 \cdot 10^{-4}$ m ² /s @ 463K	calculated
D_e (m ² /s)	$3.8 \cdot 10^{-6}$ m ² /s @ 463K	calculated
$\mu_{(He)}$ (N·s/m ²)	$2.5 \cdot 10^{-5}$ N·s/m ² @ 463K	b
ρ (kg/m ³)	0.22 kg/m ³ @ 298K; 0.14 kg/m ³ @ 463K	exp. par.
$C_{CO,b}$	$1.0 \cdot 10^{-3}$ kmol/m ³ @ 298K; $0.6 \cdot 10^{-3}$ kmol/m ³ @ 463K	exp. par.
d_p (m)	$5 \cdot 10^{-5}$ m	exp. par.

b) J.M. Coulson, J.F. Richardson, *Chemical Engineering*, vol. 1 - 4th Ed., Pergamon Press, 1990.

for calculation of Reynolds, Schmidt, Sherwood and Peclet numbers

Number	Relationship	Source	Calculated value
Reynolds	$Re = \frac{\rho \cdot v_s \cdot d_p}{(1 - \varepsilon) \cdot \mu}$	c	Re, 0.044
Schmidt	$Sc = \frac{\mu}{\rho \cdot D_{CO/He}}$	c	Sc, 1.20
Sherwood	$Sh = \frac{0.499 \cdot Re^{0.618} \cdot Sc^{0.33}}{\varepsilon} = \frac{k_c \cdot d_p}{D_{CO/He}}$	c	Sh, 0.4; $k_c = 1.15$ m/s
Peclet	$\frac{1}{Pe} = \frac{0.3}{Re \cdot Sc} + \frac{0.5}{1 + \frac{3.8}{Re \cdot Sc}}$	c	Pe, 0.19

c) Perry J.H. *Chemical Engineers Handbook – 3rd/4th/5th edition McGraw-Hill Book Company, Inc.*

the above relationships show that under the adopted conditions all mass transfer

resistances are practically negligible, indicating an ideal kinetic regime of TPCR tests in the whole temperature range.

<i>Calculated Values</i>	<i>Resistance</i>
$C_M = \frac{-r_{CO} \cdot \rho_b \cdot R \cdot n}{k_c \cdot C_{CO,b}} \cong 1.4 \cdot 10^{-3} (\ll 0.15)$	<u>No External diffusion</u>
$C_{WP} = \frac{-r_{CO,obs} \cdot \rho_c \cdot R^2}{D_e \cdot C_{CO,s}} \cong 3.8 \cdot 10^{-2} (\ll 1)$	<u>No Internal diffusion</u>
$\frac{L_b}{d_p} = \frac{2 \cdot 10^{-2}}{5 \cdot 10^{-5}} \cong 400 \left(> \frac{20 \cdot n}{Pe} \cdot \ln \left(\frac{C_0}{C} \right) = 146 \right)$	<u>No Axial Dispersion</u>

3.2.3 Experimental assessment of the kinetic regime

The absence of external diffusion phenomena was also probed experimentally by comparing CO conversion and CO₂ yield data at different contact time. The results in Figure 8 show that, varying the reaction mixture flow rate from 60 to 120 stp mL/min while keeping constant the catalyst sample (20 mg), causes a proportional decrease of X_{CO} values in the range of 293-473K (Figure 8A). These correspond to unchanging CO₂ yield values (Figure 8B), confirming the absence of external mass transfer resistances on the reaction kinetics under the adopted experimental conditions.

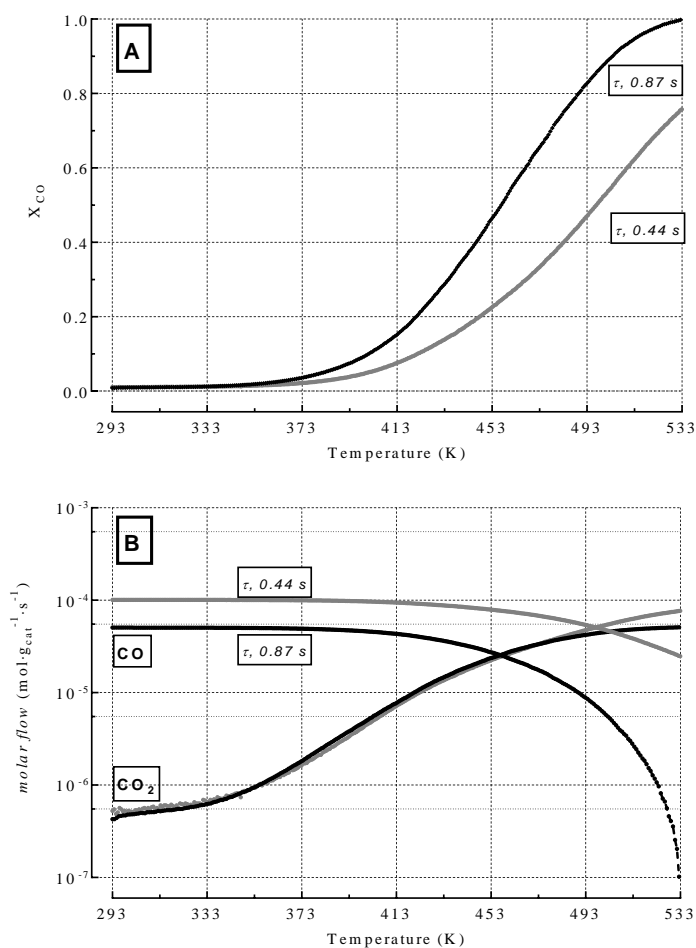


Figure 8. (A) Influence of the contact time on CO conversion and (B) CO_x molar flow. (Catalyst, M5C1; w_{cat} 0.02 g; F , 60-120 stp mL/min; P , 1 atm; p_{CO}^0 , 0.025; $p_{O_2}^0$, 0.025).

On the other hand, the lack of internal diffusion resistances was ascertained comparing the activity data of the M5C1 catalyst with average particle size of 0.05 mm (powder sample) and 0.3 mm (40-70 mesh sample). The results in Figure 9 show unchanging CO conversion levels in the range of 293-473K, which rule out the influence of internal diffusion resistances on the activity of the M5C1 catalyst up to conversion values of 70% (473K). At higher temperature, conversion values systematically lower indicate the occurrence of intraparticle diffusion phenomena, lowering the efficiency of the catalyst particles from 100 (473K) to 80% (533K).

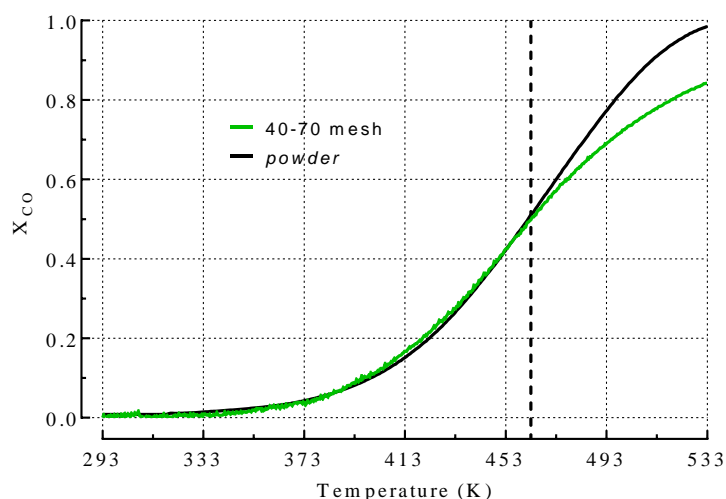


Figure 9. Influence of the particle size on CO conversion.
 (Catalyst, M5C1; w_{cab} , 0.02 g; F, 60 stp mL/min; P, 1 atm; p_{CO}^0 , 0.025; $p_{O_2}^0$, 0.025).

Lastly, the effect of the heating rate of TPCR measurements was probed to ascertain the absence of uncontrolled heat-transfer phenomena across the catalyst bed, which could be caused by the transient regime of the reaction temperature. In fact, the perfect match of activity data of the reference M5C1 catalyst at heating rate of 2 or 4K/min (Figure 10) exclude heat-transfer phenomena caused by the transient regime of TPCR tests [123,124].

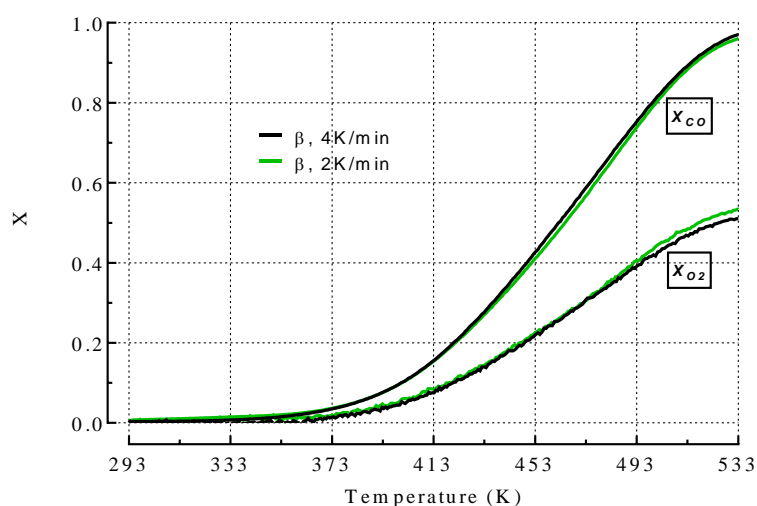


Figure 10. Effect of the heating rate (β) on CO conversion.
 (Catalyst, M5C1; w_{cab} , 0.02 g; F, 60 stp mL/min; P, 1 atm; p_{CO}^0 , 0.025; $p_{O_2}^0$, 0.025).

3.3 Effect of Cerium on the Reactivity Pattern of Composite MnCeO_x Catalysts and Nature of Active Sites

3.3.1 Effects of cerium on the CO oxidation activity

The study of the effects of cerium addition on the physico-chemical properties and CO oxidation activity pattern of composite MnCeO_x catalysts was a fundamental step of the PhD research activity, since it is aimed at providing basic information on the nature of the active phase and functionality of surface sites [125,126]. In this respect, several bare and composite materials, with Ce molar fractions varying between 0 (i.e., MnO₂) and 1 (i.e., CeO₂) were synthesized via the acidic protocol of the redox-precipitation synthesis route, being known for its efficiency in promoting the surface exposure, the dispersion and the strength of the MnO_x-CeO_x interaction [95,97,101].

The studied catalysts, with relative code and physico-chemical properties, are listed in Table 3, while Figure 11 shows an overview of their CO oxidation pattern in the range of 293-533K, under standard reaction conditions (F, 60 stp mL/min; P, 1 atm; p^0_{CO} , 0.025; $p^0_{O_2}$, 0.025).

Table 3. Physico-chemical properties of the studied catalysts.

Catalyst	Bulk Composition							SSA (m ² /g)	PV (cm ³ /g)	APD (nm)
	(wt %) ^a			(at %)						
	MnO _x	CeO _x	KO _x	Mn	Ce	K	χ _{Ce}			
C	-	100	-	-	100	-	1.00	132	0.10	3
M1C3	14.1	85.8	0.1	24.2	75.5	0.3	0.75	204	0.55	24
M1C1	34.4	65.4	0.2	50.7	48.8	0.5	0.50	190	0.46	25
M3C1	59.9	36.8	3.2	70.8	22.0	7.2	0.24	184	0.57	27
M5C1	66.9	28.4	4.7	74.3	16.0	9.7	0.18	159	0.56	30
M9C1	77.0	17.6	5.4	80.3	9.3	10.4	0.10	136	0.49	31
M	93.5	-	6.5	88.6	0.0	11.4	0.00	94	0.34	31

a) calculated as MnO₂, CeO₂ and K₂O.

The SiC material (BT), used as diluent of the catalyst bed, is practically inactive at any temperature, while the bare ceria (C) shows a low activity, according to an ignition temperature of 433K and a final CO conversion of 15% at 533K. At variance, bulk and promoted MnO_x catalysts show a high CO oxidation performance in the range of 293-533K, leading to a regular increase of conversion to final X_{CO} values of 75-100% (Figure 11A). In particular, the composite M1C1 and the bare M catalysts show the highest activity with a complete CO conversion at 533K and 503K, respectively, while the M3C1 and M5C1 samples show lower activity levels although higher than the least active M1C3 system.

Therefore, catalyst screening data disclose that the reactivity of the composite MnCeO_x materials is mostly determined by the functionality of the MnO_x phase, in agreement with previous findings in the selective oxidation of benzylic alcohol with oxygen [112].

On the other hand, the promoting effect of Mn(IV) oxo-complexes on the CO oxidation activity of ceria is predicted by recent theoretical studies on Mn-doped CeO₂ systems, in the light of a superior redox functionality in comparison to Ce(IV) ions [103,104].

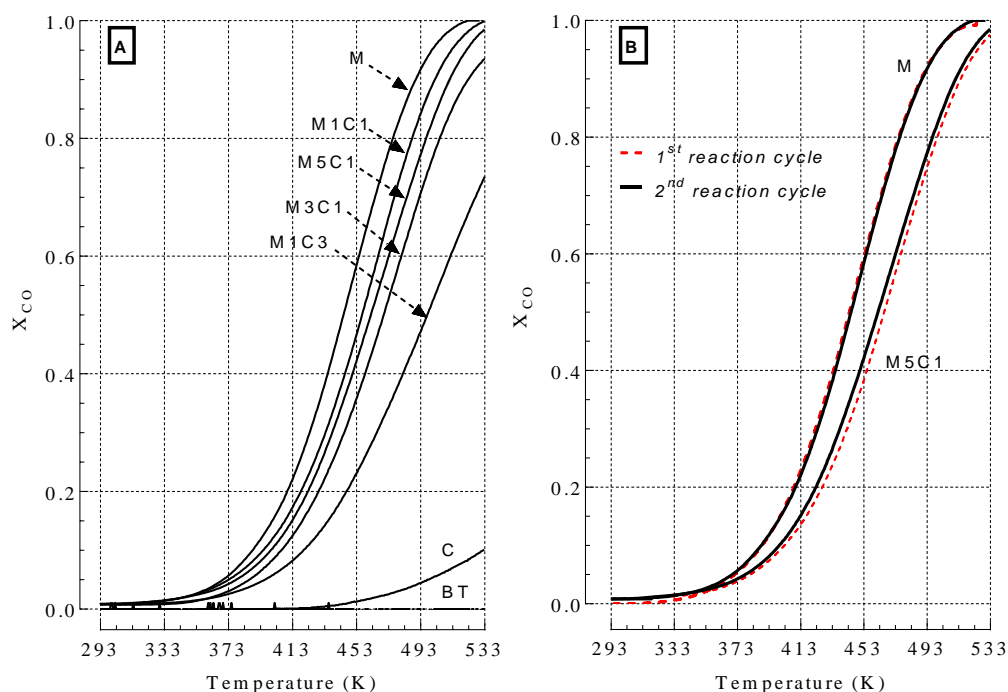


Figure 11. (A) CO oxidation conversion of the studied catalysts in the range of 293-533K; (B) Stability test (2nd reaction cycle) of M5C1 and M catalysts. (F , 60 stp mL/min; P , 1 atm; p_{CO}^0 , 0.025; $p_{O_2}^0$, 0.025; w_{cat} , 0.02 g).

The last finding of the screening study concerns the catalyst stability, this being generally the most critical issue of the reactivity pattern of heterogeneous catalysts. On this account, the bare M and the composite M5C1 catalysts were subjected to a 2nd TPCR test and the results compared with the conversion curves recorded in the 1st run in Figure 11B. Both systems show unchanging conversion patterns, indicating a good stability of the studied catalysts under CO oxidation conditions, irrespective of the composition [95,97].

3.3.2 Effects of cerium addition on the physico-chemical properties of composite MnCeO_x catalysts

3.3.2.1 Structural and textural characterization

Basic information on the structural characteristics of the studied catalysts are provided by X-ray diffraction (XRD) and Laser Raman Scattering (LRS) analyses, carried out in collaboration with CNR “ITAE” and “ITCP” Institutes of Messina, respectively.

The XRD patterns in Figure 12 show that the bare C and M materials feature several diffraction lines in the 2θ range of 20-80°, indexed to JCPDS 34-394 and JCPDS 44-0141, respectively. These are characteristic of the fluorite-like structure of cerianite and the body-centered tetragonal α -MnO₂ phase, including K⁺ ions in tunnel structure parallel to c-axis [127–130], as confirmed by chemical analysis indicating a consistent K/Mn atomic ratio of 0.12-0.13 for catalyst compositions with $\chi_{\text{Ce}} > 0.5$ (Table 3) [129].

At variance, rather featureless diffraction patterns prove a significantly lower degree of crystallinity of the oxide phases in all the composite catalysts. This is attributable to the strong MnO_x-CeO_x interactions hindering an extensive development of spatially ordered oxide structures in the composite systems. In fact, four main broad reflections at 28.5, 33.3, 47.5 and 56.5° indicate an incipient crystallization of ceria nanodomains at high Ce content ($\chi_{\text{Ce}} \geq 0.5$), the size of which is in the order of few nanometers (i.e., 3-10 nm) according to Scherrer’s equation calculations. Furthermore, no MnO_x phases are visible on the M1C3 and M1C1 samples, while the progressive growth of peak at ca. 37.5°, along with the lessening of the above signals, reveals a progressive shrinking of ceria particles and an incipient formation of MnO₂ nanodomains at low Ce loading ($\chi_{\text{Ce}} < 0.5$).

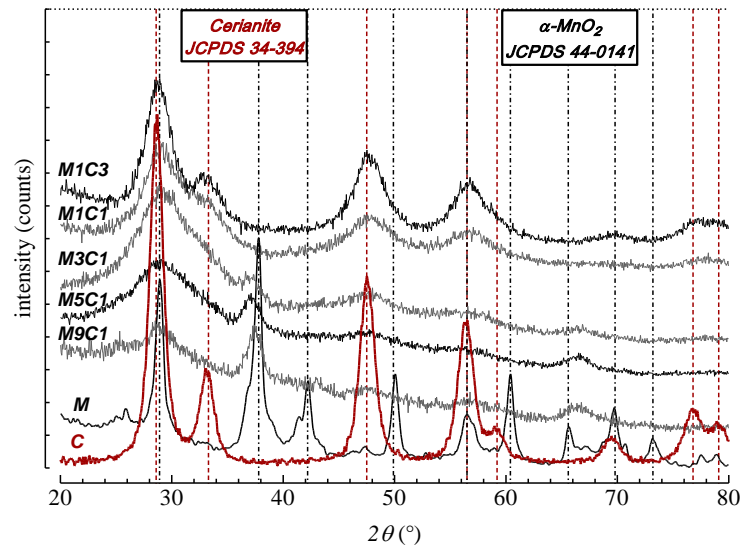


Figure 12. (A) XRD patterns of the studied catalysts.

In order to shed further light into speciation and interaction pattern of the oxide phases, the studied catalysts were subjected to LRS analysis, since this technique is very sensitive to the microstructures of nanosized material. In fact, spatial symmetries determine whether the vibrations are Raman active, whereas the changes in lattice spacing and chemical environment are responsible of the band shifts.

In particular, the bulk M sample shows three main peaks at 187, 584 and 635 cm^{-1} , confirming the predominant presence of $\alpha\text{-MnO}_2$ domains in the bulk M sample, likely in the form of *nanorods* [127,129–132]. The peak at 187 cm^{-1} disappears in the LRS spectra of the composite materials with low Ce content ($\chi_{\text{Ce}} < 0.5$), while the other two signals shift slightly, likely because of the defective nature of MnO_2 nanodomains caused by the presence of cerium promoter [130–133].

All these signals disappear at higher Ce loading ($\chi_{\text{Ce}} \geq 0.5$), while some other small peaks (430, 490 and 707 cm^{-1}) become evident (Figure 13) Their occurrence in the spectrum of the bare ceria sample and the lack of the strong F_{2g} signal of the cerianite at 465 cm^{-1} reveal the very defective character of ceria domains in the composite materials, likely

due to the extensive presence of vacancies and/or foreign ions across the ceria lattice [134]. However, red-shift of the cerianite peak and lack of “Mn-O” bond fingerprints in the range of $620\text{-}660\text{ cm}^{-1}$ could also indicate the formation of Mn-O-Ce solid solutions in such composite MnCeO_x systems [96,133,135,136].

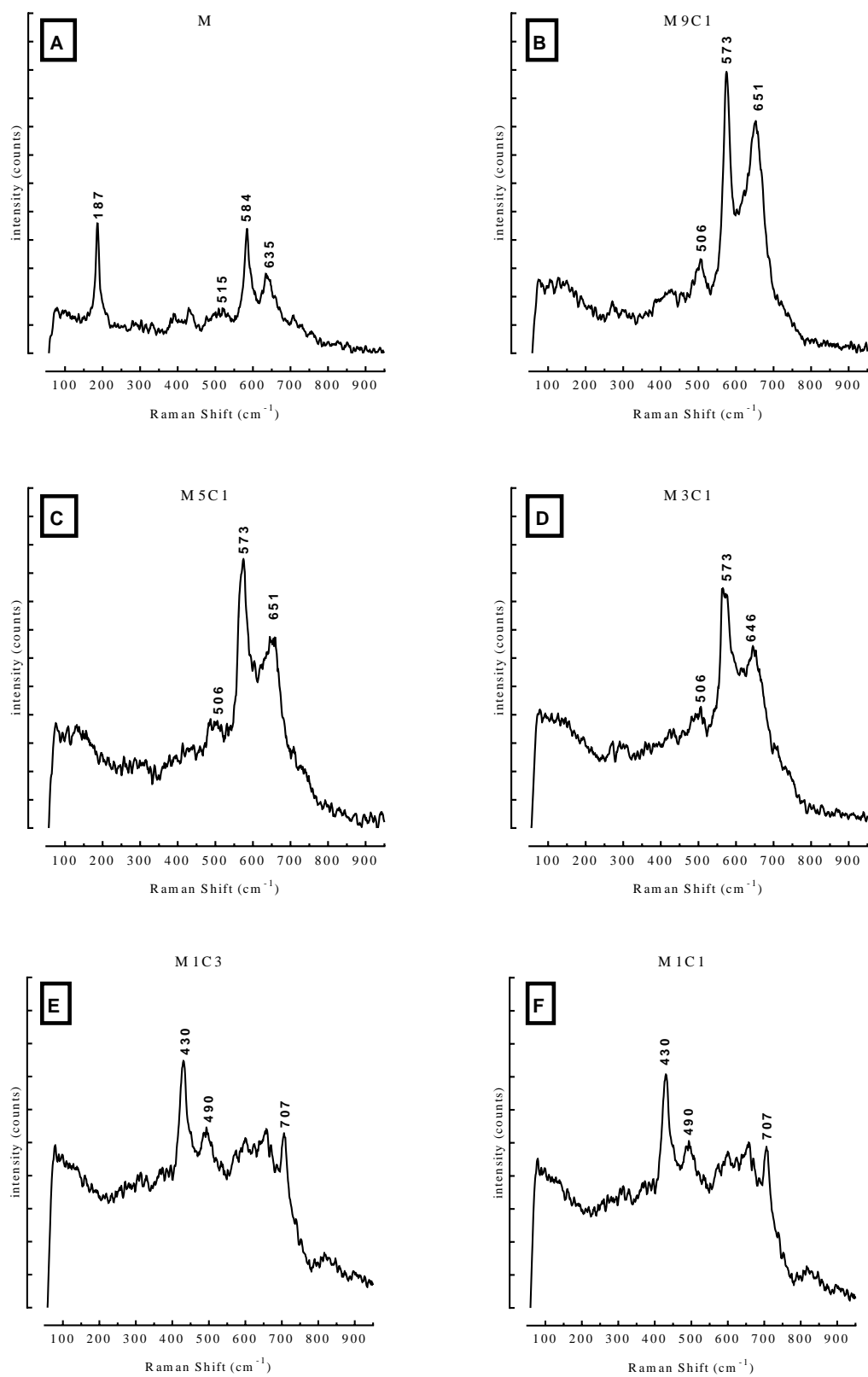


Figure 13. Laser Raman scattering spectra of the studied catalysts.

The addition of the Ce promoter also affects the catalyst texture (Table 3), as indicated by SSA values (136-204 m²/g) considerably larger than C (132 m²/g) and M (94 m²/g) materials (Figure 14). In fact, these depict a volcano-shaped trend with maximum for χ_{Ce} of 0.5, proving the occurrence of remarkable *structural effects* depending on the strength of the MnO_x-CeO_x interaction. However, PV and APD comparable to the values of the bare M sample indicate that the transport properties of MnCeO_x materials are determined by an outer shell of the MnO_x phase [112].

In conclusion, structural and textural characterization data document the occurrence of strong solid-state interactions promoting the dispersion of the oxide phases and the surface exposure of nanocomposite MnCeO_x catalysts.

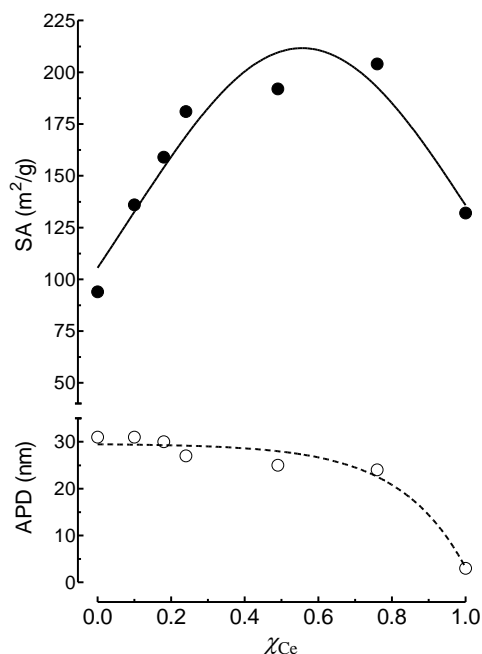


Figure 14. Influence of the cerium loading on the textural properties of the studied catalysts.

3.3.2.2 Surface Chemistry

The XPS analysis provides further insights into the effects of catalyst composition on the chemistry and dispersion of the oxide phases. On this account, the XPS spectra of Mn_{2p}, Ce_{3d} and O_{1s} core levels and the influence of the Ce loading on the average

oxidation number (AON) and the relative abundance of surface Mn and Ce atoms are shown in Figure 15. Furthermore, maximum position and split of the $2p_{3/2}$ and $2p_{1/2}$ Mn_{2p} peaks, atomic composition and AON data of Mn and Ce atoms are summarized in Table 4.

Table 4. XPS data of the studied catalysts.

Catalyst	Mn _{2p} peaks centre and 2p _{3/2} -2p _{1/2} split (eV)			atom (%)				AON (<i>n</i>)	
	2p _{3/2}	2p _{1/2}	ΔE _s	Mn	Ce	K	O	^a Mn ^{<i>n</i>+}	^b Ce ^{<i>n</i>+}
M1C3	641.4	652.8	11.4	8.1	19.8	0.0	72.1	3.1	3.9
M1C1	641.5	653.0	11.5	15.4	16.2	0.0	68.4	3.2	3.8
M5C1	642.0	653.7	11.7	28.6	6.8	3.5	61.1	3.7	3.6
M9C1	642.1	653.9	11.8	31.7	4.4	5.2	59.3	3.8	3.5
M	642.5	654.3	11.8	33.7	0.0	7.8	58.4	4.1	-

a) determined from the Mn_{2p_{3/2}} peak center; b) obtained from the relative intensity of the 916.1 eV transition [137].

The Mn_{2p} spectra feature the typical 2p_{1/2} (652.8-654.3 eV) and 2p_{3/2} (641.4-642.5 eV) signals (Figure 15A), shifting upward and with spin-orbit split values (ΔE_s) rising at lower χ_{Ce} (Table 4). Indeed, bulk (M) and composite catalysts with low Ce content (M5C1 and M9C1) feature the highest BE for both peaks and similar split values (11.7-11.8 eV), overall diagnostic of Mn atoms in the “+4” state [96,113,129]. Whereas, downward shift of Mn_{2p} peaks and lower split values (ΔE_s, 11.4-11.5 eV) indicate oxidation states close to III at high Ce content (Figure 15D) [97].

The Ce_{3d} spectra are rather complex due to the evident contribution of six transitions relative to Ce^{IV} and four hidden components of Ce^{III} ions (Figure 15B) [93,97,113,137]. Taking the transition at 916.3 eV as characteristic of the IV state [97,137], the

deconvolution analysis signals a Ce AON rising from 3.5 (M9C1) to 3.9 (M1C3) resulting, thus, in a trend opposite to Mn AON (Figure 15D).

Furthermore, all the O_{1s} spectra (Figure 15C) show a main peak, shifting from 529.1 (M1C3, M1C1) to 530.2 eV (M) and attributable to lattice ions (O_L), and a smaller component at higher B.E., with unchanging position (531.3-531.5 eV), generally ascribed to surface hydroxyls and/or adsorbed oxygen species (O_S) [97,129,133,137].

The significant shift of the O_L component mirrors a different chemical environment of lattice oxygen ions, considering that composition and strong MnO_x - CeO_x interactions could explain B.E. values typical of ceria for the M1C3 and M1C1 catalysts [97,133]. A higher intensity of the O_S peak reflects instead higher surface area, and probably exposure of defective sites, in the same samples.

The surface abundance of Mn and Ce atoms is taken as a measure of the relative dispersion of the oxide phases, thus, the surface Mn/Ce atomic ratio allows ascertaining the influence of the catalyst composition on the dispersion of the active MnO_x phase. In particular, the normalized surface Mn/Ce ratio (e.g., $[(Mn/Ce)_{XPS}]/[(Mn/Ce)_{XRF}]$) grows significantly (0.8-1.2) with χ_{Ce} (Figure 15D) as consequence of the strong MnO_x - CeO_x interaction that favors a quasi-ionic dispersion of the MnO_x phase across ceria particles, leading to the formation of solid solutions structures, mostly at high Ce loading (M1C3 and M1C1). The incipient MnO_2 crystallization, probed by structural characterization analyses, well accounts for the decreasing trend of the Mn/Ce ratio with Ce loading [96,105,113]. Finally, XPS data of the bulk M system are typical of K-containing MnO_2 species, according to XRD data [129].

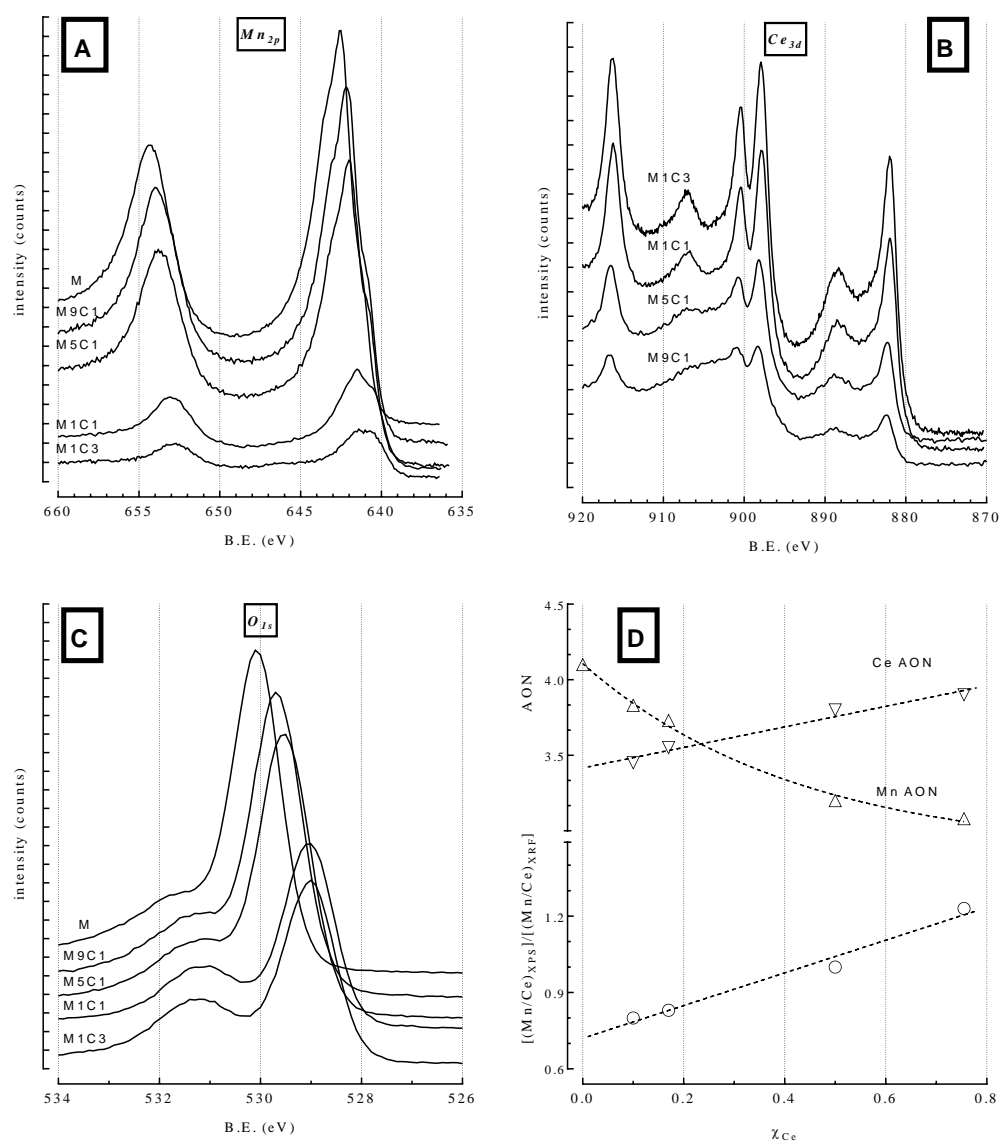


Figure 15. XPS spectra of (A) Mn_{2p} , (B) Ce_{3d} and (C) O_{1s} core levels of the various catalysts and (D) effect of cerium loading on the AON and relative abundance of surface Mn and Ce atoms.

3.3.2.3 Redox properties.

The effect of ceria on the reducibility of composite $MnCeO_x$ catalysts has been probed by CO-TPR measurements, having the additional advantage of highlighting the reactivity of catalyst oxygen species toward the reaction substrate [112]. All the profiles (Figure 16) consist of a main peak with maximum shifting from 453 (M1C1) to 533K (M), merged with a smaller component that keeps an unchanged position (607K), except for the bulk M sample (648K). The peak at low temperature is attributable to

surface Mn^{IV} centers, constituting the prevailing portion of the reduction profiles, in agreement with very high dispersion of the active phase.

The 2nd peak monitors the reduction of Mn(III) and Mn₃O₄ species ($x \leq 1.5$) [112]. An onset temperature close to 293K irrespective of composition (Figure 16) signals a similar high reactivity of surface Mn^{IV} sites to CO, consequently ruling out significant electronic effects of the ceria carrier thereon. Thus, the easier reduction of composite catalysts [112], is attributable to cerium promoting the MnO_x dispersion (i.e., *structural effect*). Actually, extents of CO consumption roughly proportional to the MnO_x loading (CO/Mn, 0.85-1.03) account for the reduction of the MnO_x phases to MnO in bulk and composite catalysts with low Ce loading, signaling the reduction of a significant fraction of surface Ce^{IV} ions in M1C3 and M1C1 catalysts.

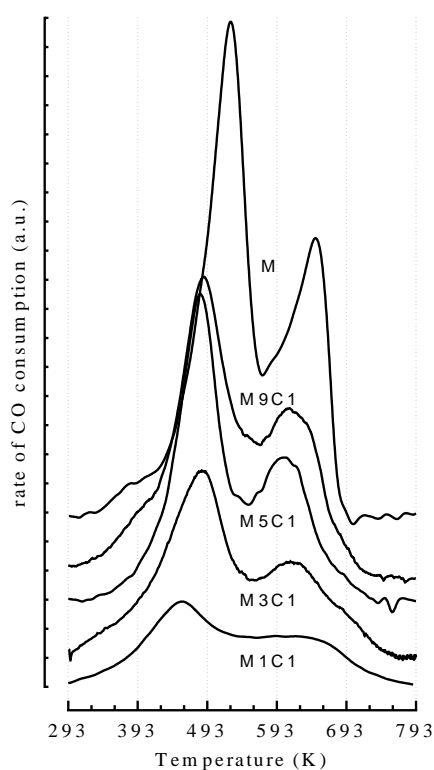


Figure 16. CO-TPR pattern of the studied catalysts.

3.3.3 Structure-activity relationships.

Basic information on the influence of Ce and temperature on the mechanism and kinetics of the CO oxidation is given by the activation energy values listed in Table 5.

Table 5. Activation energy values (E_{app}) and activity data of the studied catalysts at 393K.

Catalyst	E_{app}^a (kJ/mol)	E_{app}^b (kJ/mol)	X_{CO}^c (%)	$rate^c$ (mol _{CO} ·g _{cat} ⁻¹ ·s ⁻¹)	$rate_{MnO_x}^c$ (mol _{CO} ·g _{MnO_x} ⁻¹ ·s ⁻¹)	$rate_{SA}^c$ (mol _{CO} ·m _{cat} ⁻² ·s ⁻¹)
C	51±1	52±1	-	-	-	-
M1C3	37±1	42±1	4.6	2.3·10 ⁻⁶	1.6·10 ⁻⁵	1.1·10 ⁻⁸
M1C1	38±1	45±1	9.4	4.8·10 ⁻⁶	1.4·10 ⁻⁵	2.5·10 ⁻⁸
M3C1	45±1	47±1	6.4	3.9·10 ⁻⁶	6.5·10 ⁻⁶	2.2·10 ⁻⁸
M5C1	39±1	45±1	8.5	4.3·10 ⁻⁶	6.4·10 ⁻⁶	2.7·10 ⁻⁸
M	43±1	47±1	12.0	6.1·10 ⁻⁶	6.1·10 ⁻⁶	6.5·10 ⁻⁸

a) 3-10% X_{CO} range; b) 3-80% X_{CO} data elaboration by eq. 11 [138]; c) activity data taken from Figure 11

These were obtained from the Arrhenius plot of differential data (X_{CO} , 3-10%), while integral data (X_{CO} , 3-80%) were analyzed by the pseudo-1st order kinetic equation for catalytic oxidations in packed-bed reactor [138]:

$$\ln[-\ln(1 - X)] = \ln(a) + \ln(\tau) - \left(\frac{E_{app}}{R}\right) \cdot \frac{1}{T} \quad (11).$$

Both analyses provide accurate linear correlations (Figure 17), resulting in very close E_{app} values for all the studied systems in the whole temperature range (Table 5). These negligible differences indicate the same type of active sites irrespective of catalyst composition, also ruling out any change of reaction mechanism, according to literature data indicating a *Langmuir-Hinshelwood* (L-H) path for the CO oxidation on MnO_x and MnCeO_x systems under similar reaction conditions [93,97,98,103,104,139–141].

A higher activation barrier of the bare ceria (51-52 kJ/mol) confirms the lack of chemical effects in composite catalysts, previously probed by CO-TPR measurements.

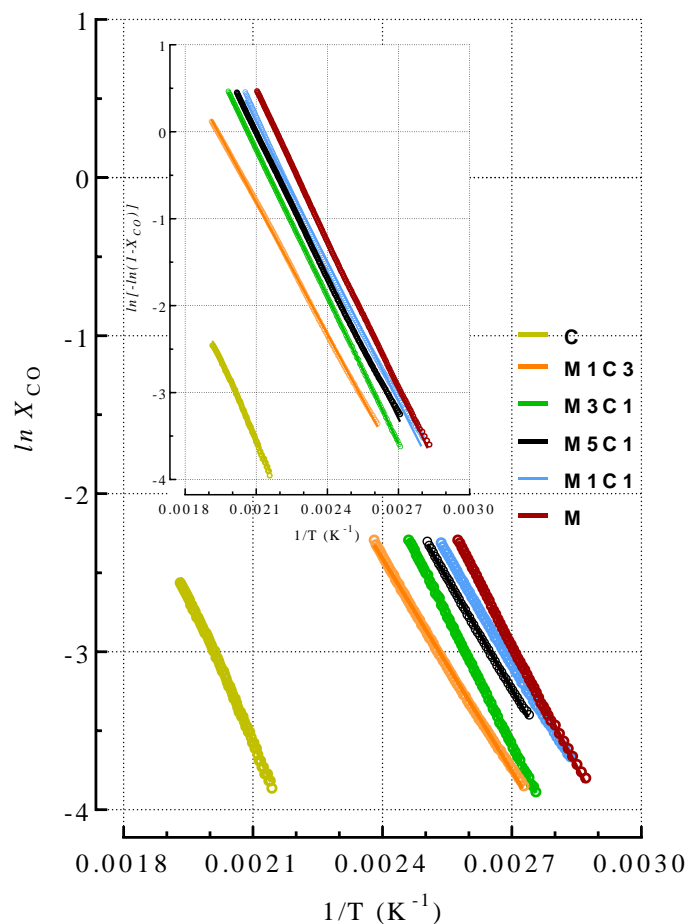


Figure 17. Arrhenius plot of differential (3-10%) CO conversion data and elaboration of integral CO conversion data (3-80%) by eq. 11 [138] (inset).

Moreover, to shed light into the nature of the active sites we have compared specific rate values with the surface abundance of the various Mn states, obtained by deconvolution analysis of the $Mn_{2p_{3/2}}$ XPS peaks using linear combination of Shirley-background and Gaussian-Lorentzian model functions centered at 640.5, 641.2, 642.3 and 643.3 eV, as shown in Figure 18 [90,94,103,153]. The first three components are associated to +2, +3 and +4 states respectively, while the latter is related to Mn(IV) ions in $KMnO_x$ species (Figure 18) [93,96,105,142]. The data of such a deconvolution analysis are summarized in Table 6.

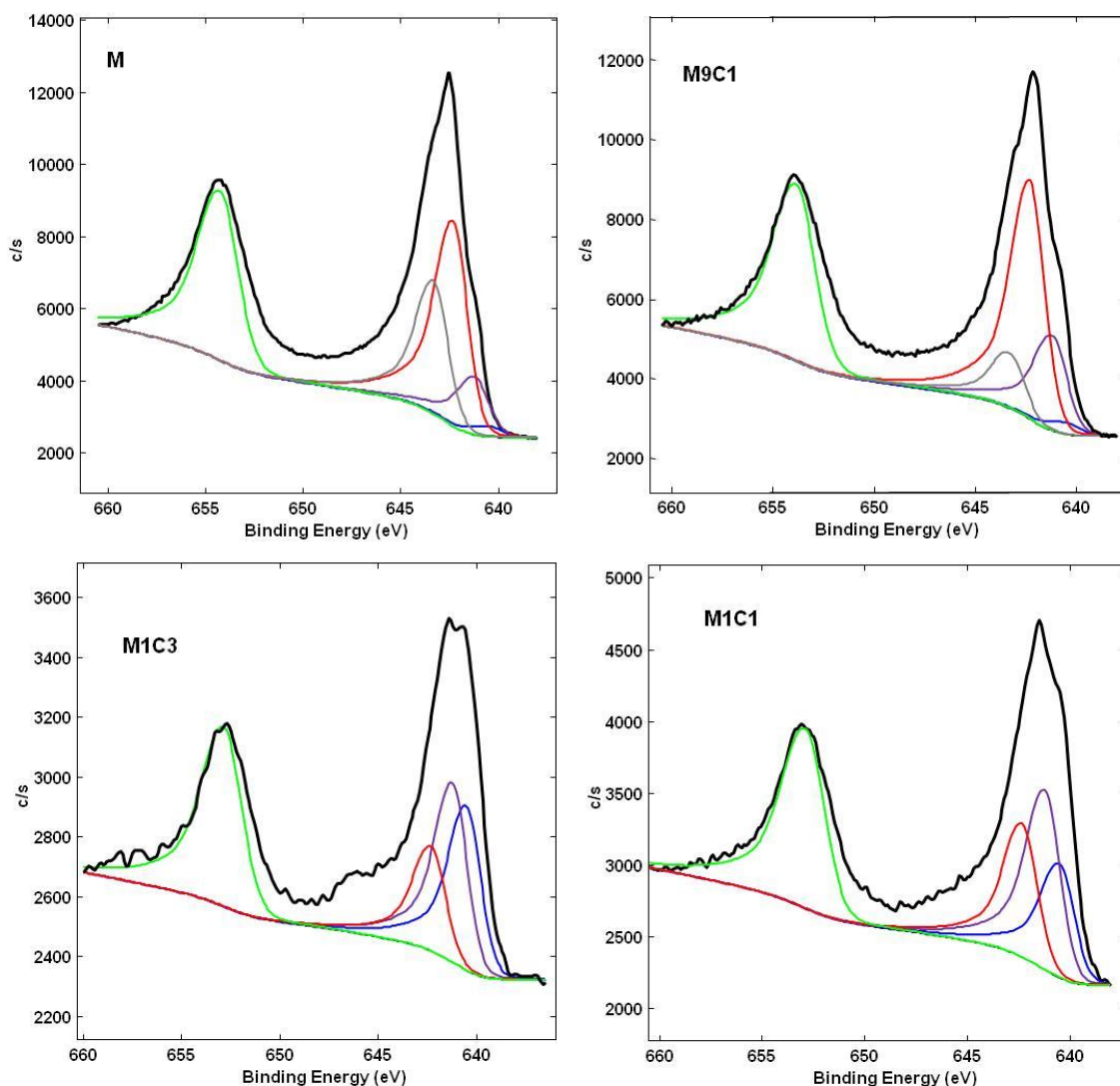


Figure 18. Deconvolution analysis of the Mn_{2p} XPS peak of the various catalysts.

Table 6. Data of the deconvolution analysis of the $Mn_{2p3/2}$ XPS peak (see Figure 18).

Catalyst	$[Mn^{II}]$		$[Mn^{III}]$		$[Mn^{IV}]$		$[Mn^{IV}]^a$		$[Mn]_{surf}^b$	AON^c
	C (eV)	A (%)	C (eV)	A (%)	C (eV)	A (%)	C (eV)	A (%)	(%)	
M1C3	640.5	36.7	641.2	40.0	642.3	23.3	-	0.0	8.1	2.87
M1C1	640.5	26.7	641.2	42.1	642.3	31.2	-	0.0	15.4	3.05
M5C1	640.6	3.3	641.2	36.7	642.3	45.6	643.3	14.4	28.6	3.57
M9C1	640.6	3.0	641.2	23.8	642.3	59.4	643.3	13.9	31.7	3.70
M	640.6	2.7	641.2	14.2	642.3	50.4	643.3	32.7	33.7	3.81

a) Mn^{IV} ions in KO_x-MnO_2 structures; b) $[Mn]_{surf} = \sum [Mn^x]$; c) $AON = (2 \times [Mn^{II}] + 3 \times [Mn^{III}] + 4 \times [Mn^{IV}])$

According to the AON data, the surface concentration of Mn^{IV} sites decreases steadily with χ_{Ce} from 90 (M) to 20% (M1C3), while that of Mn(III) and Mn(II) species depict decreasing trends, stronger for the latter (Table 6). Likely, larger populations of Mn(II) sites reflect the formation of solid solutions structures in the M1C1 and M1C3 samples [93,113,133].

Apart that the reaction rate values of the studied catalysts compare to those of other redox-precipitated MnCeO_x catalyst [97], no systematic relationships with composition could depend on different availability and type of active sites (Table 6). Therefore, the surface molar fraction of Mn(IV), Mn(III) and Mn(II) species (Figure 19A) can be compared to the specific surface activity (rate_{SA}) and the specific MnO_x activity ($\text{rate}_{\text{MnO}_x}$), considering the bulk composition of the various catalysts (Figure 19B).

The specific surface rate lowers exponentially with χ_{Ce} , with a trend similar to Mn^{IV} centers (Figure 19A), substantiating the role of active sites in the CO oxidation, irrespective of the ceria promoter [98,103,104,143]. Furthermore, the specific MnO_x rate depicts a sigmoidal-shaped trend with χ_{Ce} , indicating a twofold higher reactivity of the MnO_x phase at high Ce loading (≥ 0.5) (Figure 19B). Notably, the fact that it is similar to the concentration of Mn(II) species (Figure 19A), suggests their reasonable contribution as active sites. These are Mn(II) ions incorporated into ceria lattice, generating O-vacancies counterbalancing the lower charge of the guest ion. High reactivity and concentration of such sites explains the higher surface reactivity of the M1C1 catalyst than expected from the concentration of Mn(IV) sites, indicating that the CO oxidation functionality could be shaped by different types of active sites at high and low Ce loading.

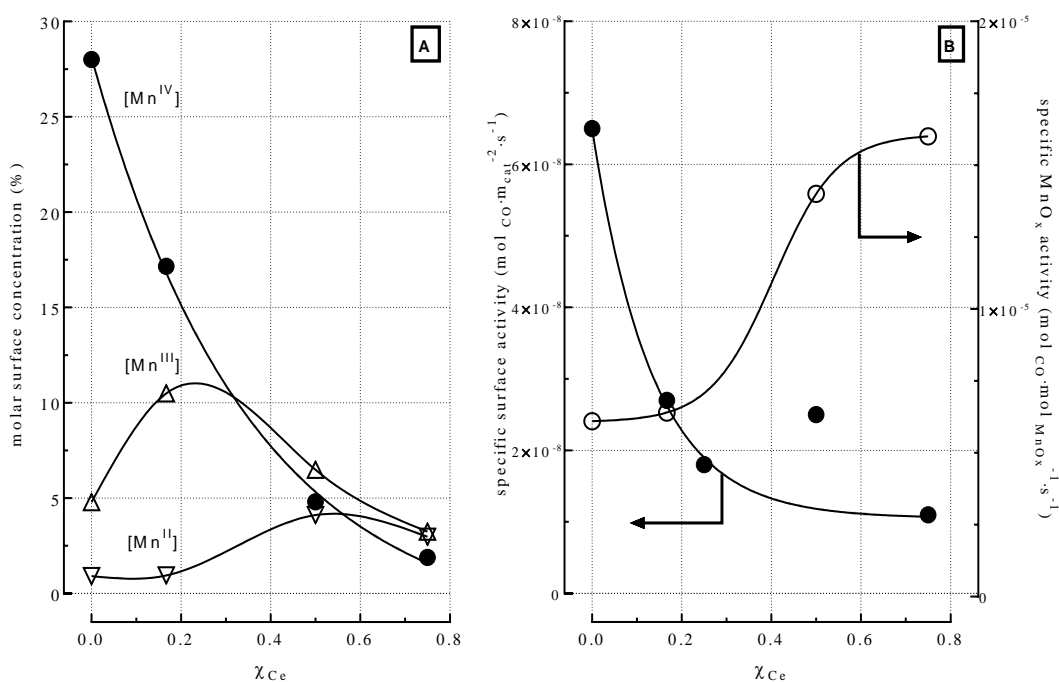


Figure 19. Influence of the cerium loading on: (A) surface concentration of Mn^x centers and (B) surface and MnO_x activity at 393K.

3.3.4 Conclusions

The study of the effects of Ce addition on the physico-chemical properties and CO oxidation functionality of MnCeO_x catalysts leads to the following conclusions:

- Cerium induces remarkable structural effects promoting surface exposure and oxide dispersion of nanostructured MnCeO_x materials;
- Oxide dispersion and MnO_x-CeO_x interaction strength determine the formation of different types of active Mn sites;
- Surface Mn(IV) and substitutional Mn(II) solid solution sites shaping the reactivity of MnCeO_x catalysts, at low and high Ce loading respectively;
- The recognized nature of active sites opens the study of the reaction mechanism on the M5C1 catalyst, representative of the reactivity pattern of surface Mn(IV) sites.

3.4 Kinetic and Mechanistic Evidences

3.4.1 Empiric Kinetics

The M5C1 catalyst was chosen as reference system for the study of the reaction kinetics and mechanism, due to the fact that its CO oxidation functionality depends essentially on the reactivity of Mn(IV) sites at the surface of MnO₂ (nano)domains (*v. supra*).

The work starts with the assessment of the empiric kinetics by a systematic study of the effects of the reagents' pressure on the CO conversion pattern in the range of 293-533K. In particular, the total reagents pressure ($p_{CO}^0 + p_{O_2}^0$) was varied between 0.02 and 0.05 atm, while the CO and O₂ pressure was varied between 0.00625 and 0.025 atm, corresponding to CO/O₂ feed ratio ($\lambda_0 = p_{CO}^0 / p_{O_2}^0$) of 0.25-4.0 (see Table 7). Such low reagents pressure ensures ideal kinetic conditions, because of the minimization of adsorption phenomena on the active sites and the absence of temperature gradients across the catalyst bed, even at high CO conversion levels.

The effects of the overall reagents' pressure ($\lambda_0, 1$) and of each single reagent ($\lambda_0, 0.25-4.0$) on the CO conversion pattern of the M5C1 catalyst are shown in Figure 20. The first evidence coming from these data is the lack of effects of the overall reagents' pressure on the CO conversion levels in the whole temperature range (Figure 20A). The integral forms of the various kinetic models suggest that this corresponds to 1st-order kinetic behaviour.

At variance, the concentration effect of each reagent is noticeable, showing conversion levels that systematically decrease with p_{CO}^0 and grow with $p_{O_2}^0$ (Figure 20B). In particular, CO conversion levels lower than expected from the relative pressure change suggests a kinetic order in-between 0 and 1 on p_{CO}^0 . Likewise, conversion levels lowering not proportionally indicate a reaction order on $p_{O_2}^0$ greater than 0, but still

lower than 1. In other words, integral conversion data are consistent with fractional kinetic dependence on both CO and O₂, resulting in overall 1st-order kinetic behaviour.

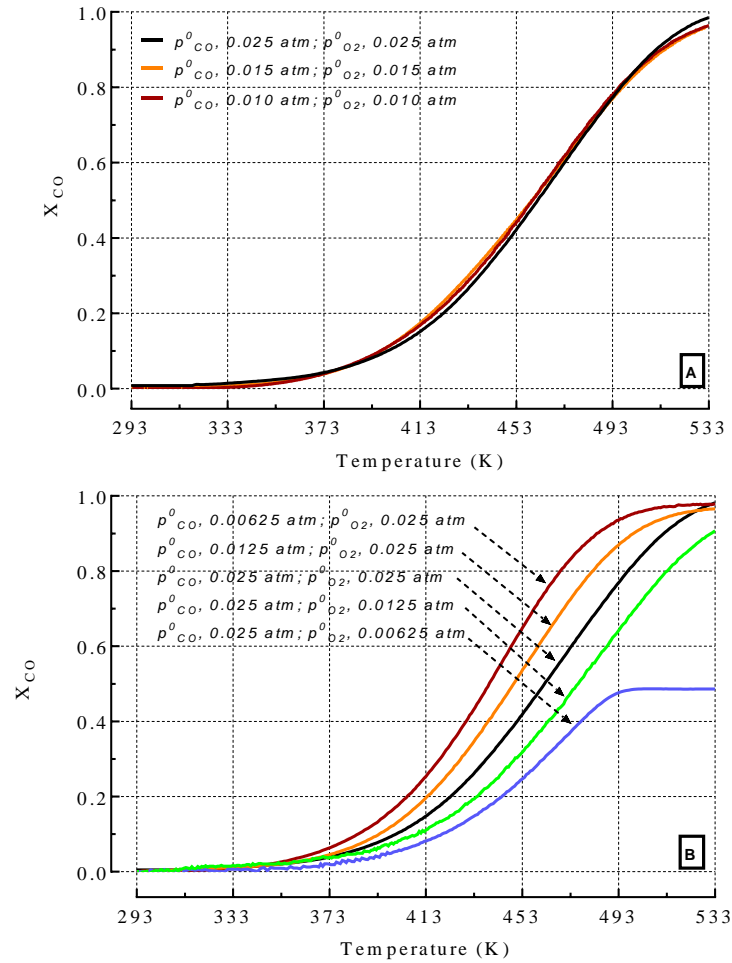


Figure 20. (A) CO conversion of the M5C1 catalyst in the range of 293-533K at different total reagents pressure (i.e., $p_{CO}^0 + p_{O_2}^0 = 0.0125-0.05$) and (B) CO/O₂ feed ratio (i.e., $\lambda_0 = p_{CO}^0/p_{O_2}^0 = 0.25-4$). (F, 60 stp mL/min; P, 1 atm; w_{cat} 0.02 g)

However, a more accurate assessment of the reaction kinetics is obtained from the *log-plot* of rate values at differential conversion levels ($X_{CO} < 12\%$) at different p_{CO}^0 and $p_{O_2}^0$ (Table 7), shown in Figure 21. The rate data depict rather accurate straight-line relationships as a function of both p_{CO}^0 and $p_{O_2}^0$, indicating similar constant reaction orders in the range of 353-403K of $0.6(\pm 0.1)$ and $0.4(\pm 0.1)$ on p_{CO}^0 and $p_{O_2}^0$,

respectively (Figure 21). These account for overall 1st order kinetics and fractional kinetic dependence on each reagent, previously assessed in qualitative terms.

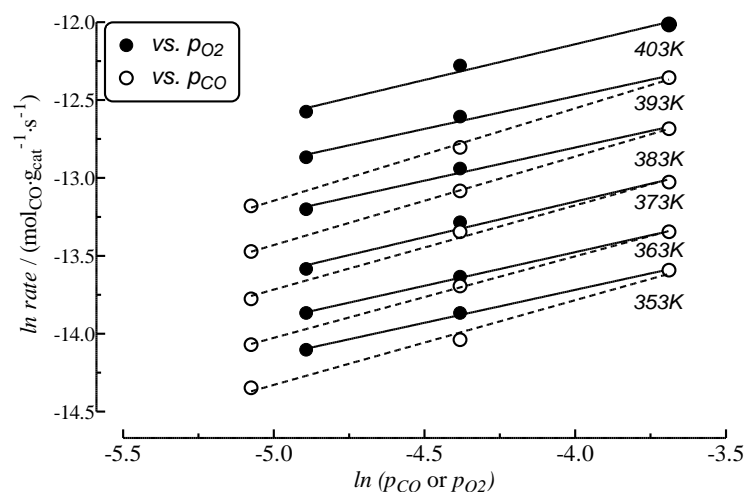


Figure 21. Log-plot of kinetic data ($X < 10\%$) in the range of 353-403K (data from Figure 20).

Such empiric kinetics match literature data for the CO oxidation on composite MnCeO_x [97] and MnO_x catalysts [139–141], although they are not related to any specific reaction mechanism [144,145]. However, they signal a strong interaction of CO with the catalyst surface, definitely ruling out the Eley-Rideal path implying 1st-order kinetic dependence on the reagent in the gas phase, while the half-order on $p_{O_2}^0$ would signal a dissociative adsorption mechanism that is rather unlikely on oxide surfaces.

Table 7. Influence of CO and O₂ partial pressure on reaction rate at various temperatures (Figure 20A).

reagent pressure (atm)		Temperature (K)					
$p_{O_2}^0$	p_{CO}^0	353	363	373	383	393	403
		reaction rate ($\text{mol}_{CO} \cdot \text{g}_{cat}^{-1} \cdot \text{s}^{-1}$)					
0.00625	0.025	$7.5 \cdot 10^{-7}$	$9.5 \cdot 10^{-7}$	$1.3 \cdot 10^{-6}$	$1.9 \cdot 10^{-6}$	$2.6 \cdot 10^{-6}$	$3.5 \cdot 10^{-6}$
0.0125	0.025	$9.5 \cdot 10^{-7}$	$1.2 \cdot 10^{-6}$	$1.7 \cdot 10^{-6}$	$2.4 \cdot 10^{-6}$	$3.4 \cdot 10^{-6}$	$4.7 \cdot 10^{-6}$
0.025	0.025	$1.3 \cdot 10^{-6}$	$1.6 \cdot 10^{-6}$	$2.2 \cdot 10^{-6}$	$3.1 \cdot 10^{-6}$	$4.3 \cdot 10^{-6}$	$6.1 \cdot 10^{-6}$
0.025	0.00625	$5.9 \cdot 10^{-7}$	$7.8 \cdot 10^{-7}$	$1.0 \cdot 10^{-6}$	$1.4 \cdot 10^{-6}$	$1.9 \cdot 10^{-6}$	n.d.
0.025	0.0125	$8.5 \cdot 10^{-7}$	$1.1 \cdot 10^{-6}$	$1.6 \cdot 10^{-6}$	$2.1 \cdot 10^{-6}$	$2.8 \cdot 10^{-6}$	n.d.
0.025	0.025	$1.3 \cdot 10^{-6}$	$1.6 \cdot 10^{-6}$	$2.2 \cdot 10^{-6}$	$3.1 \cdot 10^{-6}$	$4.3 \cdot 10^{-6}$	$6.1 \cdot 10^{-6}$

Finally, considering the potential importance of adsorption-desorption phenomena that could affect the reaction rate in the studied range of temperature, the kinetic effect of CO_2 has to be taken into account. In particular, two standard TPCR tests co-feeding CO_2 at 0.05 and 0.10 atm have been performed and compared with previous data in absence of CO_2 in Figure 22. In fact, CO_2 exerts a negative effect on CO oxidation activity at any temperature, the extent of which strengthens as $p^0_{\text{CO}_2}$ increases (Figure 22). This negative kinetic dependence on $p^0_{\text{CO}_2}$ reflects a competitive adsorption of the reaction product on active sites, being diagnostic of a surface L-H type reaction path, [144]. Such effect is obviously negligible under standard conditions due to the low partial pressure of CO_2 (≤ 0.025 atm) throughout the catalytic tests [124].

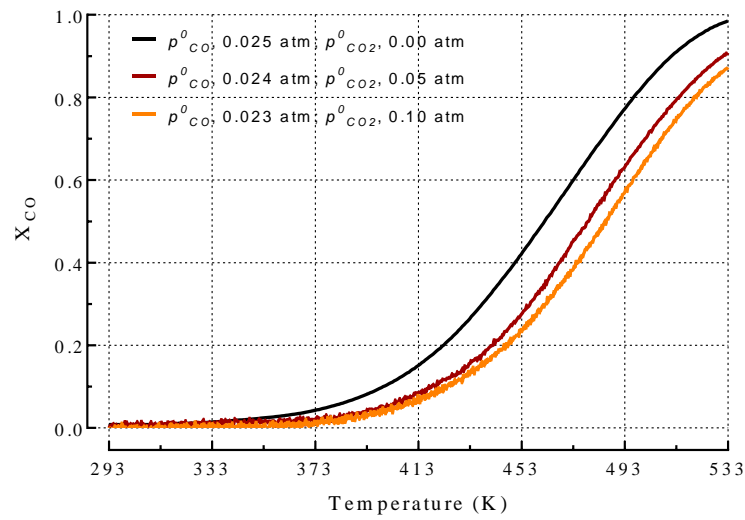


Figure 22. Effect of the CO_2 co-feeding ($p^0_{\text{CO}_2}$, 0-0.1 atm) on CO conversion in the range of 293-533K (p^0_{CO} , 0.023-0.025 atm; λ_0 , 1).

3.4.2 Mechanistic evidences

3.4.2.1 Mobility and reactivity of catalyst oxygen species

Reactivity and mobility of catalyst oxygen species are very crucial issues for the oxidative functionality of TMO catalysts [31,146], since a *Mars-van Krevelen* (MvK) mechanism implies the oxidation of the substrate and the reduction of O₂ at different sites of the catalytic surface, promoted by the high mobility of lattice oxygen ions [146,147]. This fundamental properties were probed by *isothermal pulse reaction* tests and *temperature programmed desorption* measurements.

In particular, isothermal pulse oxidation tests at 393K, in presence and absence of gas phase O₂, were carried out in this study to evaluate the reactivity and mobility of lattice oxygen ions under reaction conditions, useful to ascertain the occurrence of the *Mars van Krevelen* reaction path [144,147]. Figure 23 shows the CO and CO₂ signals (Figure 23A) and the CO conversion (Figure 23B) during five consecutive CO pulses under 5% O₂/He and He carrier flow, respectively.

These data show a constant CO₂ production during five pulses under O₂/He carrier flow, corresponding to a steady CO conversion of 22-23%. Whereas, a lower reactivity, also declining during time, is observable under He flow; the CO pulse conversion attains an initial value of 15%, lowering progressively during the successive pulses. This finding uncovers a mobility of lattice oxygen ions under reaction conditions too low to effectively sustain the surface reaction cycle at a rate comparable to that in presence of O₂. In other words, such data rule out a reaction path involving different surface sites for the CO oxidation step by lattice oxygen species and the oxygen replenishment by gas phase O₂, that is typical of the *Mars van Krevelen* mechanism [144,147].

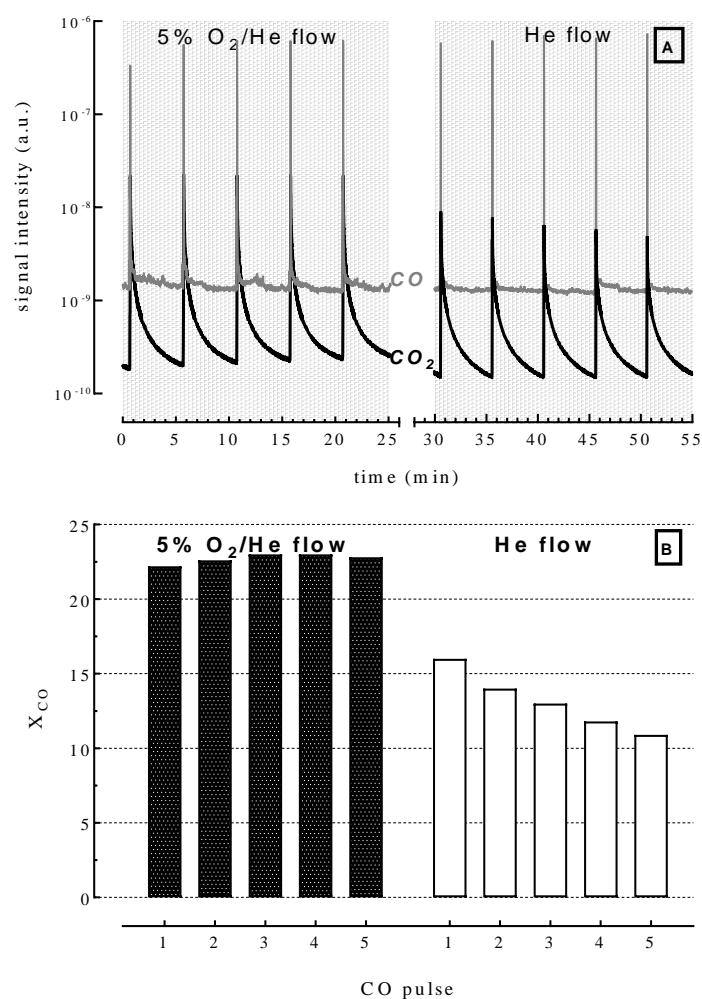


Figure 23. CO-pulse ($1.3 \mu\text{mol}_{\text{CO}}$) reaction test at 393K under 5% O₂/He and He carrier flow (F , 35 mL/min; w_{cat} 20 mg).

A confirmation of such evidence comes from the O₂ uptake measurements at steady state indicating a fully oxidized status of the catalyst surface in contrast to the significant catalyst reduction predicted by the MvK mechanism [124,146], and mostly from the O₂ desorption pattern of the catalyst, probed by the TPD analyses in Figure 24. A poor mobility of lattice oxygen ions under reaction conditions is evident from the O₂-TPD pattern, showing the largest portion of oxygen release at $T > 643\text{K}$, well beyond the temperature of catalyst testing. Irrespective of the treatment atmosphere, all the TPD profiles show an analogous O₂ desorption band in the range of 593-973K, with an

inflection point at 743K and two maxima at 753 and 913K, accounting for the thermal reduction of surface and bulk MnO_x species to Mn_3O_4 , according to an overall release of $2.0 \pm 0.1 \text{ mmol}_{\text{O}_2}/\text{g}_{\text{cat}}$ [148]. Some slight differences in the desorption profiles in the range of 293-493K concern the small O_2 peak due to adsorbed reactive oxygen species (Figure 24) [93,97,114,149]. Its absence in the profile of the sample treated under CO proves, in fact, the high reactivity of such oxygen species toward the substrate, while the higher intensity for the sample exposed to the CO/O_2 reaction mixture confirms the over-oxidized status of the catalyst, probed by O_2 uptake measurements under steady state conditions.

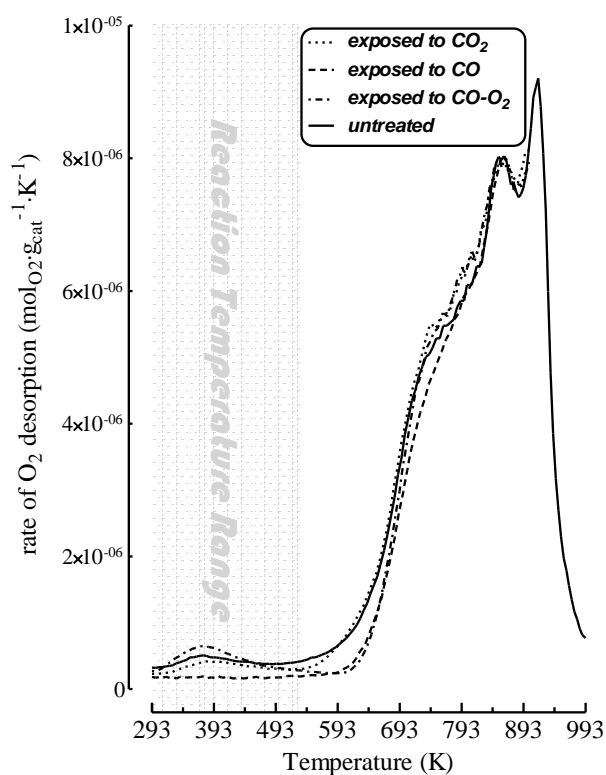


Figure 24. O_2 -TPD pattern of the M5C1 catalyst exposed to CO, CO/O_2 and CO_2 flow at 298K (1h).

3.4.2.2 Surface interactions and reaction intermediates

The interaction of the catalyst with CO and the presence of adsorbed species on the catalyst surface under steady state conditions were probed by temperature programmed

desorption measurements of catalyst samples pretreated at 298K under CO, CO-O₂ and CO₂ flow (1h), shown in Figure 25A. Irrespective of the pre-treatment, the lack of any CO desorption signal proves the strong interaction of the substrate molecule with the catalyst surface, leading to a prompt formation of CO₂, also in absence of O₂ [95,112,124,143]. All the CO₂-TPD profiles show a main peak strongly tailed on the high-temperature side, whose characteristics depend on the treatment atmosphere. The catalyst sample treated in the CO-O₂ stream features a main peak (343K) centered 30K below that recorded after treatment in CO (373K), while both show the contribution of another small component centered at 483K.

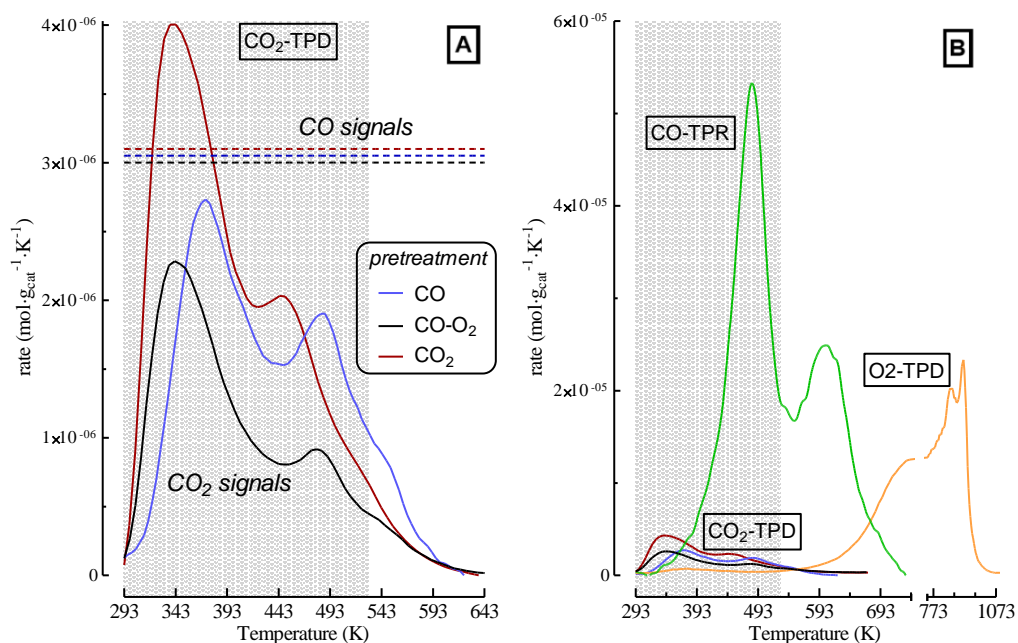


Figure 25. (A) CO₂ Temperature programmed desorption profiles of the M5C1 catalyst pretreated in CO, CO-O₂ and CO₂. (B) Comparison of O₂-TPD, CO₂-TPD and CO-TPR of the M5C1 sample.

Apart from a higher intensity, likely due to a saturation pressure (p_{CO_2}) of 0.10 atm, the CO₂ adsorption gives rise to a TPD profile analogous to that produced by the reaction mixture, signaling a reversible formation of the less stable carbonate species.

Finally, the comparison of the rates of CO-TPR, O₂-TPD and CO₂-TPD, shown in Figure 25B, highlights a much faster catalyst reduction than O₂ and CO₂ desorption in the range of temperature of the catalytic tests.

A summary of IR spectroscopy data, useful to ascertain the surface interactions of CO with MnO_x and MnCeO_x systems and the nature of adsorbed species, both in absence and presence of O₂, is presented in Table 8 [93,98,143,150].

Beside to the signals in the ranges of 2100-2200 cm⁻¹ and 2300-2400 cm⁻¹, typical of gas-phase and/or weakly interacting CO and carbonate species, the literature data show a general consensus on bands at 1217-1233, 1340-1381 (1455-1470) and 1552-1580 cm⁻¹, due to *bridged*, *unidentate* and *bidentate* carbonate intermediates, respectively (Figure 26) [151]. Their occurrence in presence and absence of O₂, even at 85K [143], supports the high reactivity of catalyst surface oxygen species toward CO, although the presence of the bidentate species (1565 cm⁻¹) is strictly related to the presence of O₂. Generally, it occurs at low temperature (≤298K) and only at T≥393K in absence of O₂ (Table 8).

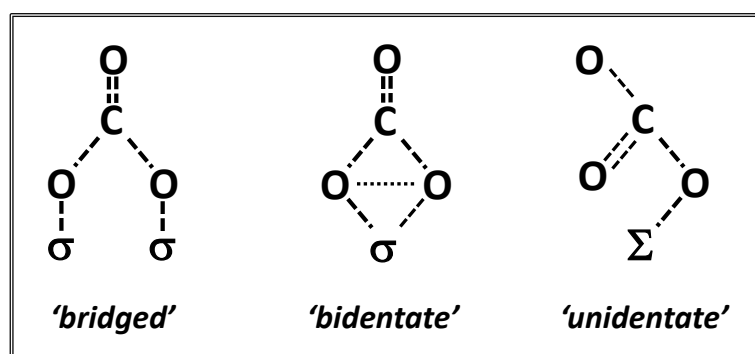
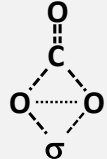
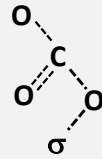
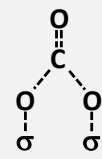


Figure 26. Scheme of carbonate intermediates forming at the surface of TMO systems. Adapted from ref. [151].

Therefore, it can be argued that the *bridged* carbonate is due to the adsorption of CO on the oxidised sites of the catalyst in absence of O₂, being responsible of the peak at 373K. At variance, the *bidentate* intermediate arises from the interaction of CO with

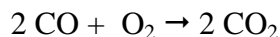
diatomic oxygen species adsorbed on O-vacancies, this being more reactive than previous one, according to lower TPD maximum (343K). Finally, the last TPD component (453-483K) is ascribable to the most stable *unidentate* carbonate species, which is the result of the interaction of CO₂ molecules with surface basic centres (i.e., ΣO). Its formation regardless of the treatment atmosphere infers that it is not a reactive intermediate having thus, a marginal role, if any, in the catalytic cycle (i.e., “spectator” species [98,123,124,151,152]).

Table 8. Summary of literature IR spectroscopy data for CO adsorption on MnO_x and MnCeO_x materials.

Sample	Exp. Conditions	IR signals (cm ⁻¹)							Ref.	
		Free carbonate species	Gas phase or weakly interacting CO	 'bidentate'		 'unidentate'		 'bridged'		
MnCeO _x	CO/O ₂ ; T, 298-393K		2113-2173							[93]
		2340-2360								
				1568		1470	1390	1217		
MnCeO _x	CO; T, 298K	2330		1614		1533	1348		1218	[98]
	CO; T, 673K	2400-2300			1568	1533		1394	1218	
	CO/O ₂ ; T, 298K			1609	1565		1395		1218	
	CO/O ₂ ; T, 673K				1565	1526	1348		1218	
MnO _x	CO; T, 298K			1675			1340		1220	
	CO; T, 673K	2360	2113-2150				1494,1418	1360	1220	
	CO/O ₂ ; T, 298K		2117-2173	1670	1568		1340		1220	
MnO _x /YSZ	CO; T, 85K		2161		1657			1375		[143]
	CO; T, 298K				1605			1455	1333 1224	
MnO _x /Al ₂ O ₃ MnCeO _x /Al ₂ O ₃	CO; T, 100K		2170-2180							[150]
	CO; T, 473-673K			1768	1552		1456	1384	1233	

3.4.3 Reaction mechanism

The CO oxidation



is a well-known “model” reaction that can provide basic information on the oxidative functionality of heterogeneous catalysts, due to a simple chemistry making easier the study of surface reaction steps and intermediates leading to active sites and surface oxygen species identification [31].

However, despite the numerous studies devoted during the last decades at ascertaining the CO oxidation functionality of MnO_x catalysts, reaction mechanism, active sites and nature of oxygen species are still matter of debate. This uncertainty depends on a variety of oxide phases, supports and promoters, and a decisive influence of the reaction system on the steady-state of MnO_x -based systems [83,89,148,90,95,97,128,139–141,143], similarly to noble-metal systems [31,153]. In this respect, kinetic-mechanistic evidences exclude the classical *Eley-Rideal* and *MvK redox* mechanisms pointing, conversely, to a *Langmuir-Hinshelwood* (L-H) path, according to recent computational studies on model M(IV)-doped CeO_2 systems, indicating the following reaction network for the CO oxidation by Mn(IV) active centres [103].

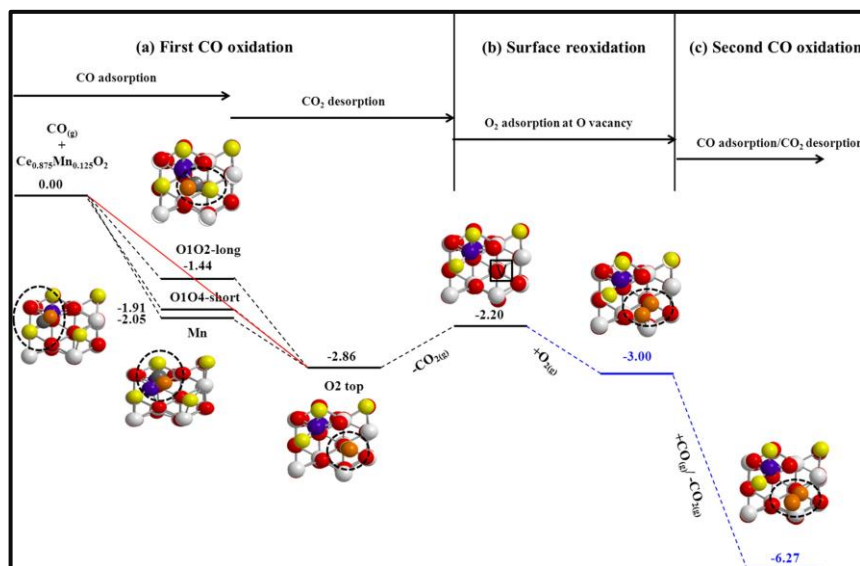


Figure 27. Calculated potential energy diagram for CO oxidation on $Ce_{0.875}Mn_{0.125}O_2$ (111) surface and catalyst regeneration adapted from ref. [103].

The proposed catalytic cycle involves: (A) *the adsorption and the oxidation of a first CO molecule* on the stoichiometric $Ce_{0.875}Mn_{0.125}O_2$ (111) surface through participation of catalyst oxygen, leading to the formation of O-vacancy and CO_2 desorption; (B) *the adsorption of molecular O_2 at the O-vacancy*, leading to the formation of surface adspecies; (C) *the interaction of a CO molecule with these O adspecies*, which drives the formation of the 2nd CO_2 molecule regenerating the $Ce_{0.875}Mn_{0.125}O_2$ (111) surface. Although being the result of theoretical evaluations, it is evident that this scheme matches the experimental evidences of this study, as indicated in the followings:

- a fractional kinetic dependence on p_{CO}^0 , index of a strong interaction of CO with the catalyst surface;
- an *easy abstraction of oxygen atoms* adjacent to surface Mn^{IV} sites in the same reaction temperature range, as probed by the reducibility pattern;
- a significant *kinetic effect* of gas phase O_2 , ruling out the *step-wise* redox path;
- a *poor mobility of lattice oxygen ions* under reaction condition;

- a reversible formation of *adsorbed carbonate species* in competition for active sites.

Thus, the last unsolved issues for devising the possible reaction mechanism remain the role of catalyst oxygen and the *rate determining step (r.d.s.)* [144,146]. In this respect, an analysis of the activation energy barrier of the reaction steps allows ascertaining the origin of the *r.d.s.*. The Arrhenius plots of differential rate data ($X < 12\%$) and of integral conversion data ($X > 12\%$), elaborated by 1st-order model for a packed-bed reactor [138]

$$\ln[-\ln(1 - X)] = k \cdot \tau \quad (12),$$

are compared to the Arrhenius plot of the rate of catalyst reduction (CO-TPR) in Figure 28 [95,123,152].

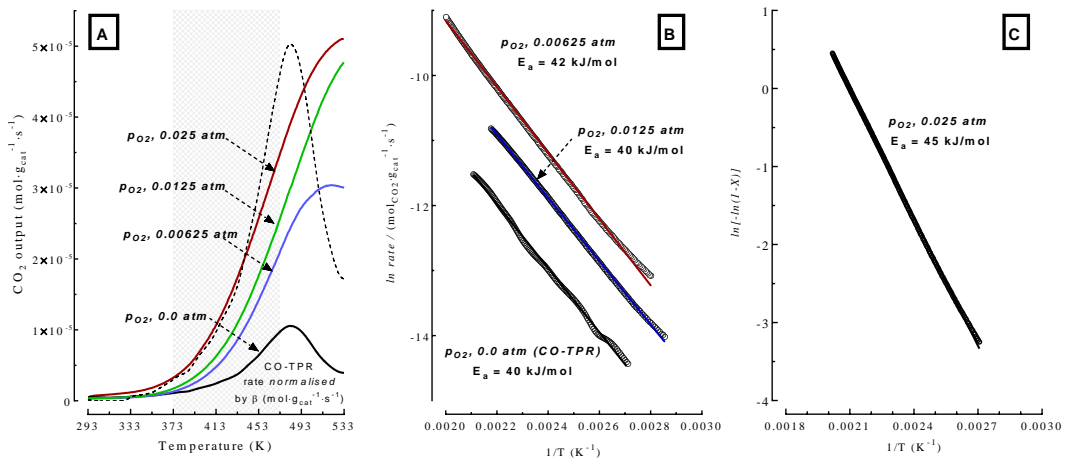
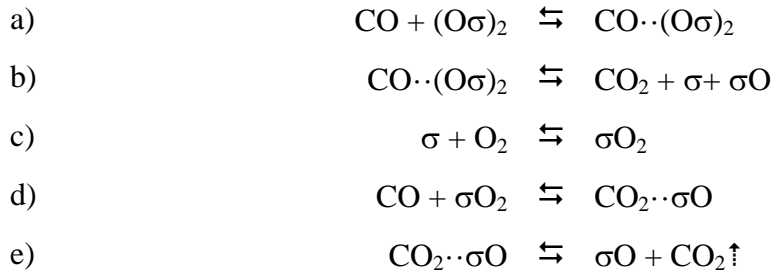


Figure 28. (A) Rate of CO₂ formation at various p_{O₂} (0.0-0.025 atm); (B) and (C) Arrhenius plot of the CO₂ rate in the range of 373-473K.

All these provide analogous straight-line relationships, accounting for activation energy values of 40-45 kJ/mol, proving that the formation of O-vacancies is the *r.d.s.* of the surface reaction cycle [90,91,140,141,143,154,93,95,97,98,103,104,133,139]. These match the activation energy values (41 ± 3 kJ/mol) found for reduction and CO oxidation on the M1C1-R4 catalyst [97], being also in satisfactory agreement with the energy

barrier (0.22-0.37 eV) predicted for the formation of surface O-vacancies on the model $\text{Mn}_{0.125}\text{Ce}_{0.875}\text{O}_2$ system [103].

Therefore, all the evidences infer that the CO oxidation on the M5C1 catalyst proceeds via an *extrafacial* L-H type reaction path [93,97,98,103,104,146,148], involving catalyst oxygen atoms and adsorbed O_2 species, according to the following reaction scheme:



It consists of the following five elementary reaction steps:

- a) CO adsorption on active Mn^{IV} sites forming the *bridged* intermediate (i.e., $\text{CO}\cdot\cdot(\text{O}\sigma)_2$);
- b) the decomposition of the latter into CO_2 and surface O-vacancy (i.e., σ);
- c) the adsorption of O_2 on σ , forming reactive *diatomic oxygen species* (i.e., σO_2);
- d) the interaction of a second CO molecule with the σO_2 intermediate, leading to the formation of the *bidentate intermediate* (i.e., $\text{CO}_2\cdot\cdot\sigma\text{O}$);
- e) the decomposition of the latter into a CO_2 molecule, with *replenishment of the active site* (i.e., σO).

According to literature and experimental evidences, it explains the relationship between activity and catalyst reducibility, generally taken as diagnostic of the MvK mechanism. It also elucidates the surface interactions leading to the various carbonate intermediates.

Indeed, the $\text{CO}\cdot\cdot(\sigma\text{O})_2$ intermediates mirror the features of *bridged* carbonate species, arising from the interaction of CO with two active Mn^{IV} sites $(\sigma\text{O})_2$, while the $\text{CO}_2\cdot\cdot\sigma\text{O}$ species matches structure and stoichiometry of *bidentate* carbonates, generated by the interaction of CO with adsorbed diatomic oxygen species (i.e., O_2^- ; $\text{O}_2^{\cdot-}$). A pictorial

description of the surface reaction cycle in Figure 29 shows the various reaction steps and intermediates, stressing the role of *spectator* species for the *unidentate* carbonate.

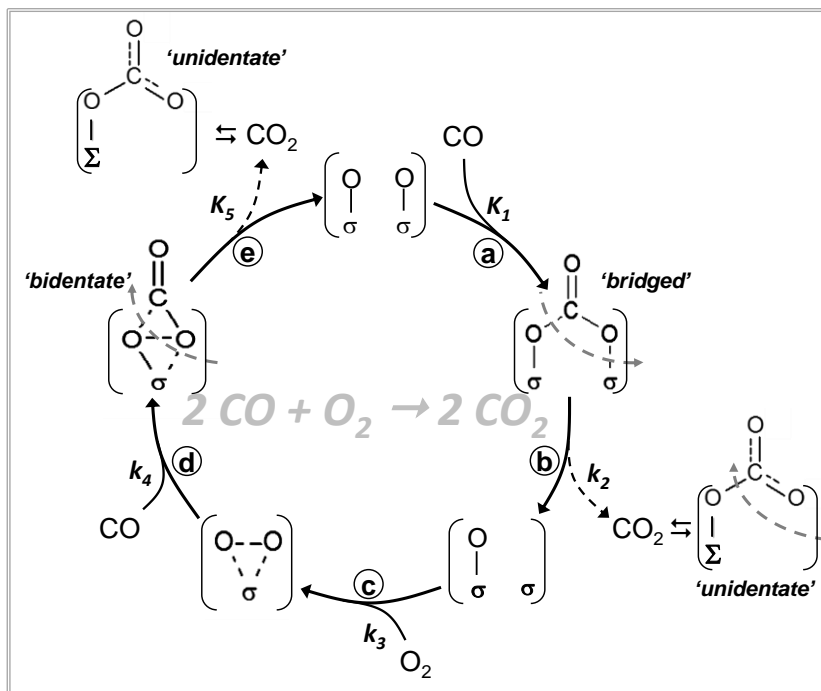


Figure 29. Scheme of the CO oxidation reaction cycle on the M5C1 catalyst.

3.4.4 Kinetic Modelling

The derivation of the formal kinetic equation is the next step of this work, essential to ascertain validity and field of applicability of the above reaction mechanism. Despite a small number of elementary steps, however, some conventional approximations are essential to get a friendly form of the kinetic equation.

In particular, supported by a reversible formation of the reaction intermediates [151], the CO adsorption (a) and the CO₂ desorption steps (e) are assumed at equilibrium conditions (*q.e.*), while the approximation of *irreversible step (i.s.)* for b (*r.d.s.*), c (*fast*), and d (*fast*) ones can be made.

These lead to the following thermodynamic and kinetic relationships

$$q.e. \quad K_1 = \frac{[\sigma O \cdot CO]}{p_{CO} \cdot [\sigma O]} \quad (13),$$

$$r.d.s. \quad r_2 = k_2 \cdot [\sigma OCCO] \quad (14),$$

$$i.s. \quad r_3 = k_3 \cdot p_{O_2} \cdot [\sigma] \quad (15),$$

$$i.s. \quad r_4 = k_4 \cdot p_{CO} \cdot [\sigma O_2] \quad (16),$$

$$q.e. \quad K_5 = \frac{[\sigma O] \cdot p_{CO_2}}{[\sigma O \cdot CO_2]} \quad (17).$$

Hence, the mass-balance on active sites and intermediates, along with thermodynamic and kinetic relationships (i.e., $r_2=r_3=r_4$), provide the following expression for the active sites:

$$[\sigma O] = \frac{1}{\left[1 + K_1 \cdot p_{CO} + \frac{K_1 \cdot k_2 \cdot p_{CO}}{k_3 \cdot p_{O_2}} + \frac{K_1 \cdot k_2}{k_4} + \frac{p_{CO_2}}{K_5} \right]} \quad (18).$$

Neglecting the last term due to very small p_{CO_2} ($<2.5 \cdot 10^{-3}$ atm) for differential CO conversion conditions, the expression for the fraction of active sites in the fundamental status

$$[\sigma O] = \frac{1}{1 + K_1 \cdot p_{CO} + \frac{K_1 \cdot k_2 \cdot p_{CO}}{k_3 \cdot p_{O_2}} + \frac{K_1 \cdot k_2}{k_4}} \quad (19),$$

leads to the final equation rate

$$rate = \frac{K_1 \cdot k_2 \cdot k_3 \cdot k_4 \cdot p_{CO} \cdot p_{O_2}}{k_3 \cdot k_4 \cdot p_{O_2} + K_1 \cdot k_3 \cdot k_4 \cdot p_{CO} \cdot p_{O_2} + K_1 \cdot k_2 \cdot k_4 \cdot p_{CO} + K_1 \cdot k_2 \cdot k_3 \cdot p_{O_2}} \quad (20).$$

However, the complexity of such equation rate hinders a reliable assessment of the kinetic parameters by the fitting of experimental rate data. Therefore, the eq. 20 was transformed in the reciprocal function, corresponding to the sum of the various kinetic resistances:

$$\frac{p_{CO}^0 \cdot p_{O_2}^0}{rate} = p_{CO}^0 \cdot p_{O_2}^0 \cdot \left[\frac{1}{(K_1 \cdot k_2) \cdot p_{CO}} + \frac{1}{k_4 \cdot p_{CO}} + \frac{1}{k_2} + \frac{1}{k_3 \cdot p_{O_2}} \right] \quad (21),$$

Being $p_{CO}^0 \approx p_{CO}$ and $p_{O_2}^0 \approx p_{O_2}$ under differential conversion conditions, the following straight-lines as a function of p_{CO}^0 and $p_{O_2}^0$ can be taken into account:

$$\frac{p_{CO}^0 \cdot p_{O_2}^0}{rate} = \frac{p_{O_2}^0}{k_{CO_2}} + \frac{p_{CO}^0 \cdot p_{O_2}^0}{k_2} + \frac{p_{CO}^0}{k_3} \quad (22),$$

considering that k_{CO_2} corresponds to the reciprocal of the sum of resistances for steps a-b and d, yielding to two CO₂ molecules

$$\frac{1}{k_{CO_2}} = \frac{1}{(K_1 \cdot k_2)} + \frac{1}{k_4} \quad (23).$$

In fact, experimental rate data elaborated by the eq. 22 provides two series of straight-line relationships as function of both p_{CO}^0 (Figure 30A) and $p_{O_2}^0$ (Figure 30B), slope and intercept values of which provide the kinetic constants k_2 , k_3 and k_{CO_2} in the range of 353-403K, listed in Table 9.

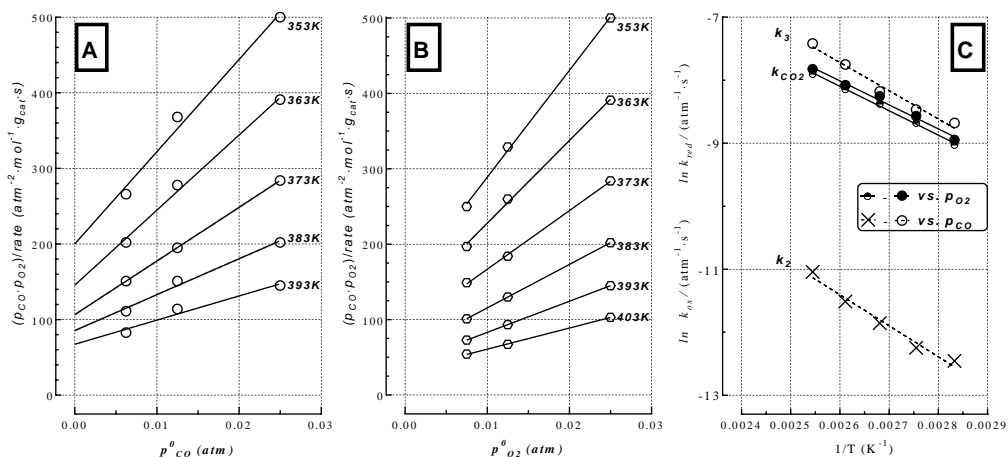


Figure 30. Elaboration of rate data by eq. 22 at different p_{CO} (A) and p_{O_2} (B) and Arrhenius plot of k_2 , k_3 and k_{CO_2} (C).

Table 9. Slope and intercept values of the straight-line relationships obtained from rate data elaborated by the eq. 22 (Figure 30), and kinetic constant values of the various reaction steps.

T (K)	$slope_{CO}$	$intercept_{CO}$	$slope_{O_2}$	$intercept_{O_2}$	k_2 (s^{-1})	k_3 ($s^{-1} \cdot atm_{O_2}^{-1}$)	k_{CO_2} ($s^{-1} \cdot atm_{CO}^{-1}$)
353	12,210±1426	200±24	14,170±471	147±8	$4.0 \cdot 10^{-6}$	$1.7 \cdot 10^{-4}$	$1.3 \cdot 10^{-4}$
363	9,931±772	146±13	10,970±471	118±1	$4.8 \cdot 10^{-6}$	$2.1 \cdot 10^{-4}$	$1.7 \cdot 10^{-4}$
373	7,097±20	107±1	8,757±396	89±4	$7.1 \cdot 10^{-6}$	$2.8 \cdot 10^{-4}$	$2.1 \cdot 10^{-4}$
383	4,743±574	86±10	6,194±376	58±1	$1.0 \cdot 10^{-5}$	$4.3 \cdot 10^{-4}$	$2.8 \cdot 10^{-4}$
393	3,198±622	67±10	4,445±267	42±1	$1.6 \cdot 10^{-5}$	$6.0 \cdot 10^{-4}$	$3.6 \cdot 10^{-4}$
403	n.d.	n.d.	3,051±162	33±1	n.d.	$7.6 \cdot 10^{-4}$	n.d.

Referring to the $\sigma O \cdot CO$ reaction step (b), the constant k_2 ($mol \cdot g_{cat}^{-1} \cdot s^{-1}$) is smaller than k_{CO_2} and k_3 ($mol \cdot g_{cat}^{-1} \cdot s^{-1} \cdot atm^{-1}$) by almost two orders of magnitude (Table 9), being insensitive to the reagent pressure. Moreover, the temperature dependence of the above constants indicates an energy barrier of 38-46 kJ/mol (Figure 30), consistent with the

apparent activation values (Figure 26) [123,152]. In fact, the derivative function of eq. 20 on temperature reciprocal shows that the apparent value mirrors the energetic barrier for the formation of the surface O-vacancy:

$$E_{app} = \Delta H_1 + E_2 \quad (24),$$

confirming a negligible energetic barrier for the steps c-e [103,104].

Thus, matching theoretical and experimental evidences, the proposed reaction mechanism and its kinetic model provide a definitive account of the CO oxidation functionality of the MnCeO_x system, confirmed by the *parity plot* in Figure 31, documenting the excellent agreement between calculated and experimental rate data in the range 353-403K (Table 7).

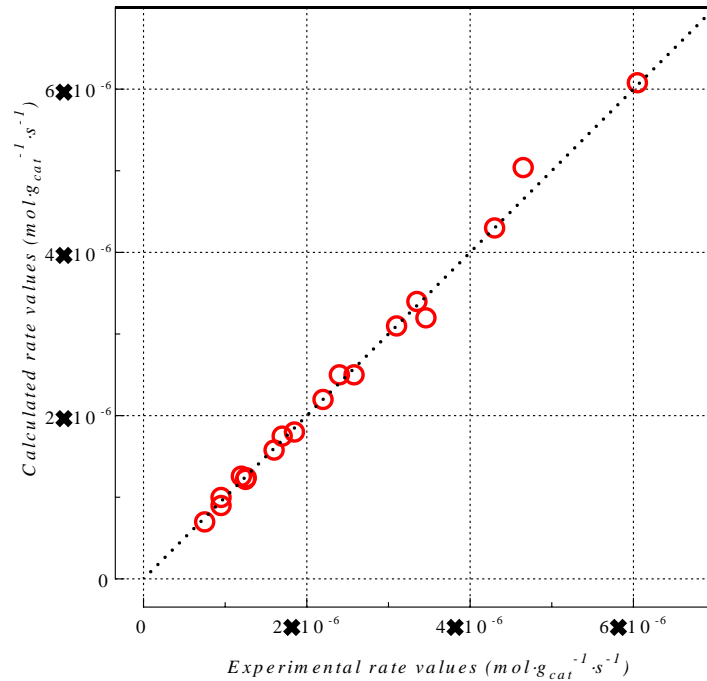


Figure 31. Calculated vs. experimental rate values in the range of 353–403 K at different p_{CO} and p_{O_2} .

In addition, considering the unchanging reaction mechanism (Figure 28), the kinetic model can be employed to simulate the reactivity pattern of the M5C1 catalyst in the whole temperature and conversion ranges (Figure 20) [4,6-9,18-22].

The integral rate equation is obtained from the relationship among conversion (X), rate and contact time (τ , $s \cdot g_{cat} \cdot mol_{CO}^{-1}$)

$$\frac{dX}{d\tau} = rate \quad (25).$$

Taking into account the kinetic effects of CO₂, substitution of eq. 20 in 25 leads to the following indefinite integral

$$\int \left[\frac{1}{k_3 \cdot p_{O_2}} + \frac{1}{k_2} + \frac{1}{k_{CO_2} \cdot p_{CO}} + \frac{K_5 \cdot p_{CO_2}}{K_1 \cdot k_2 \cdot p_{CO}} \right] dX = \tau \quad (26).$$

Using the relationships 27a and 27b for p_{CO} and p_{O₂}

$$p_{CO} = p_{CO}^0 \cdot (1 - X) \quad (27a) \quad p_{O_2} = \frac{p_{CO}^0}{\lambda_0} \cdot \left(1 - \frac{\lambda_0}{2} \cdot X \right) \quad (27b),$$

And considering that λ_0 is equal to the ratio $p_{CO}^0/p_{O_2}^0$, the equation giving X as a function of temperature through the k_2, k_3, k_{CO_2} constants is

$$\left[-\frac{2}{k_3 \cdot p_{CO}^0} \cdot \ln \left(1 - \frac{\lambda_0}{2} \cdot X \right) + \frac{1}{k_2} \cdot X - \left(\frac{1}{k_{CO_2} \cdot p_{CO}^0} + \frac{K_5 \cdot p_{CO_2}^0}{K_1 \cdot k_2 \cdot p_{CO}^0} \right) \cdot \ln(1 - X) \right] = \tau \quad (28).$$

With the values of the k_2, k_3 and k_{CO_2} constants in the range of 403-533K, predicted by the Arrhenius plots (Figure 30), conversion data were calculated by the eq. 28 and compared to experimental ones in Figure 32. A very good agreement between predicted and observed data, at any reagents pressure (p_{CO}^0 , 0.01-0.025 atm; $\lambda_0, 1$), $p_{CO}^0/p_{O_2}^0$ ratio

(λ_0 , 0.25-4.0) and temperature (293-533K), substantiates the reliability of the kinetic model to simulate the CO oxidation pattern of the M5C1 catalyst in all reaction conditions. Consequently, the eq. 28 constitutes the scientific background for process design, as it allows predicting the conditions to attain the desired degree of conversion, known p_{CO}^0 , λ_0 and $p_{CO_2}^0$.

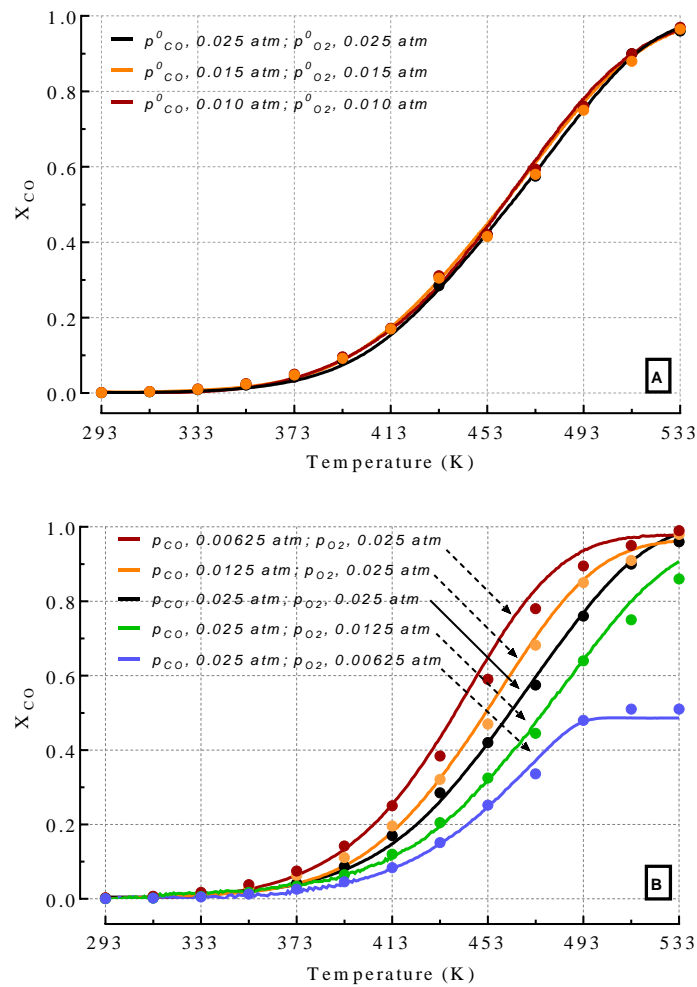


Figure 32. Predicted (symbols) and experimental CO conversion data (lines) at different reagents concentration and λ_0 values.

Moreover, modelling of conversion data with CO₂ co-feed (Figure 22) by eq. 28 also allows evaluating the ratio of CO₂ and CO adsorption constants from the K_5/K_1 ratio. In fact, the model signals a twofold decrease of the K_5/K_1 ratio in the range of 353-513K,

accounting for an average CO adsorption enthalpy higher than CO₂ by 8±1 kJ/mol (Figure 33).

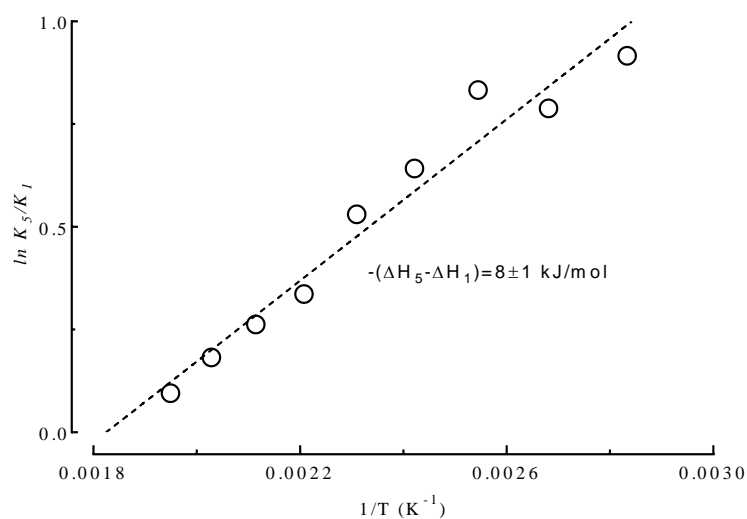


Figure 33. Van't Hoff plot of the K_5/K_1 ratio in the range of 353-513K.

3.4.5 Conclusions

Activity data in a wide range of experimental conditions and systematic evidences on the reaction mechanism are synthesised into the following conclusions:

- a fractional kinetic order on p_{CO} exclude an *Eley-Rideal* mechanism;
- low lattice oxygen mobility and significant kinetic effect of oxygen rule out a typical step-wise *Mars-van Krevelen* redox mechanism;
- the adsorption of reagent and product molecules leads to the formation of various surface carbonate intermediates;
- CO₂ has a negative influence on the CO oxidation activity;
- high reactivity of surface oxygen to CO signals an *extrafacial redox* path, started by abstraction of oxygen atoms from active Mn^{IV} sites;
- the formation of O-vacancies is the *r.d.s* of the surface reaction network;

- very reactive diatomic oxygen species are generated on O-vacancies, explaining the significant kinetic effect of gas phase O₂;
- a *Langmuir-Hinshelwood* mechanism fully predicts the CO oxidation activity of the M5C1 catalyst in the range of 293-533K;
- the kinetic model obtained can be employed to engineer the reactivity pattern of the M5C1 catalyst in all reaction conditions in terms of temperature, reagents pressure and ratio, and contact time.

4. FINAL REMARKS AND FUTURE PROSPECTS

Catalytic oxidation technologies can play a key role in the elimination of harmful gaseous compounds, thanks to the development of increasingly active and economic materials. To achieve this goal, it is necessary to deepen the knowledge that we possess of the catalytic systems, and of the reaction mechanisms that govern their behavior. This PhD thesis work, therefore, illustrates a series of results that contribute to the aforementioned aims, by analyzing the catalytic pattern of MnCeO_x systems in the carbon monoxide oxidation.

From the systematic comparison of the characterization and catalytic activity data of a series of catalysts, it was possible to define the role of cerium as a structural promoter, and identify surface Mn(IV) centers as the catalytic active sites. The latter information has a dual function, providing a starting point for catalyst optimization and the subsequent study of the reaction mechanism.

In this context, evidences on the role of reagents and products, surface intermediates, active oxygen species and *rate determining step* of the catalytic cycle led to the formulation of a *Langmuir-Hinshelwood* mechanism that fully predicts the CO oxidation activity of the M5C1 catalyst in the range of 293-533K. The kinetic model derived can be employed as a practical tool to engineer the reactivity pattern of the catalyst in all reaction conditions in terms of temperature, reagents pressure and ratio, and contact time.

Although these results may seem apparently of a theoretical nature, the acquired knowledge on the catalytic oxidation functionality of Mn-based systems can lead to

further applicative developments. Preliminary tests over MnCeO_x catalysts have already shown a good activity and selectivity, in fact, in PROX (Preferential Oxidation) reaction. Atomistic computational approaches, such as the DFT ones, on a model manganese system would be highly desirable, not only to support the experimental and theoretical findings presented in this thesis work, but also to explain the different reactivity of these materials towards hydrogen. Finally, the conclusions of this study constitute a precious scientific background for a better knowledge of the oxidative pattern of MnCeO_x composite catalyst in liquid phase reactions like the CWAO and the green selective oxidation of organic substrates for the synthesis of fine chemicals.

5. REFERENCES

- [1] NASA, The relentless rise of carbon dioxide – Climate Change: Vital Signs of the Planet, 2018.
- [2] Environmental Protection Agency (EPA), Real-time World Air Quality Index, 2018.
- [3] World Health Organization, Ambient air pollution: A global assessment of exposure and burden of disease, Geneva, 2016.
- [4] D.R. Lide, CRC Handbook of Chemistry and Physics, CRC Press, Boca Raton, 2005.
- [5] I. Blumenthal, J. R. Soc. Med. 94 (2001) 270–272.
- [6] J.M. Berg, J.L. Tymoczko, L. Stryer, Biochemistry, Fifth Ed., W.H. Freeman, New York, 2002.
- [7] K. Schmidt-Nielsen, Animal physiology : adaptation and environment, Fourth Ed., Cambridge University Press, Cambridge, 1990.
- [8] L.K. Weaver, N. Engl. J. Med. 360 (2009) 1217–1225.
- [9] M. Goldstein, J. Emerg. Nurs. 34 (2008) 538–42.
- [10] T. Struttman, A. Scheerer, T.S. Prince, L.A. Goldstein, J. Am. Board Fam. Med. 11 (1998) 481–484.
- [11] D.G. Penney, Carbon monoxide poisoning, CRC Press, Boca Raton, 2008.
- [12] S.T. Omaye, Toxicology. 180 (2002) 139–150.
- [13] D. Ehhalt, M. Prather, IPCC - Climate Change 2001: The Scientific Basis - Grid-Arendal, 2001.
- [14] Environmental Protection Agency (EPA), Carbon Monoxide Emissions, 2015.
- [15] J.S. Daniel, S. Solomon, J. Geophys. Res. 103 (1998) 13249–13260.
- [16] P.J. Bergamaschi, P Hein, R Heimann M Crutzen, 105 (2000) 1909–1927.
- [17] D.A. Hauglustaine, G.P. Brasseur, S. Walters, P.J. Rasch, J.-F. Müller, L.K. Emmons, M.A. Carroll, J. Geophys. Res. Atmos. 103 (1998) 28291–28335.
- [18] V. Smil, Enriching the earth : Fritz Haber, Carl Bosch, and the transformation of world food production, MIT Press, Cambridge, Massachusetts, 2001.
- [19] S. Ritter, Chem. Eng. News News Ed. Am. Chem. Soc. (2008).
- [20] G. Centi, P. Ciambelli, S. Perathoner, P. Russo, Catal. Today. 75 (2002) 3–15.

- [21] H. Dai, *Sci. Bull.* 60 (2015) 1708–1710.
- [22] R.M. Stephenson, S. Malanowski, *Handbook of the Thermodynamics of Organic Compounds*, Springer Netherlands, Dordrecht, 1987.
- [23] I. Langmuir, *J. Am. Chem. Soc.* 40 (1918) 1361–1403.
- [24] J. Kašpar, P. Fornasiero, N. Hickey, *Catal. Today.* 77 (2003) 419–449.
- [25] H.-F. Oetjen, V.M. Schmidt, U. Stimming, F. Trila, *J. Electrochem. Soc.* 143 (1996) 3838.
- [26] Q. Li, R. He, J.O. Jensen, N.J. Bjerrum, *Chem. Mater.* 15 (2003) 4896–4915.
- [27] E.D. Park, D. Lee, H.C. Lee, *Catal. Today.* 139 (2009) 280–290.
- [28] A.B. Lamb, W.C. Bray, J.C.W. Frazer, *J. Ind. Eng. Chem.* 12 (1920) 213–221.
- [29] H.J. Freund, G. Meijer, M. Scheffler, R. Schlögl, M. Wolf, *Angew. Chemie - Int. Ed.* 50 (2011) 10064–10094.
- [30] C.D. Jones, *The Ambient Temperature Oxidation of Carbon Monoxide By Copper-Manganese Oxide Based Catalysts*, Cardiff University, 2006.
- [31] S. Royer, D. Duprez, *ChemCatChem.* 3 (2011) 24–65.
- [32] Y.-F.Y. Yao, *J. Catal.* 87 (1984) 152–162.
- [33] N.W. Cant, *J. Catal.* 62 (1980) 173–175.
- [34] S.H. Oh, C.C. Eickel, *J. Catal.* 128 (1991) 526–536.
- [35] M. V. Twigg, *Platin. Met. Rev.* 54 (2010) 180–183.
- [36] H.C. Yao, Y.F.Y. Yao, *J. Catal.* 86 (1984) 254–265.
- [37] B.B. Harrison, A.F. Diwell, C. Hallett, *Platin. Met. Rev.* (1988) 73–83.
- [38] J. Barbier, D. Duprez, *Appl. Catal. B Environ.* 4 (1994) 105–140.
- [39] S. Bedrane, C. Descorme, D. Duprez, *Catal. Today.* 73 (2002) 233–238.
- [40] S. Bedrane, C. Descorme, D. Duprez, *Appl. Catal. A Gen.* 289 (2005) 90–96.
- [41] N.R. Collins, M. V. Twigg, *Top. Catal.* 42–43 (2007) 323–332.
- [42] J. Barbier, D. Duprez, *Appl. Catal. B-Environmental.* 3 (1993) 61–83.
- [43] R.H. Nibbelke, M.A.J. Campman, J.H.B.J. Hoebink, G.B. Marin, *J. Catal.* 373 (1997) 358–373.
- [44] S.H. Oh, C.C. Eickel, *J. Catal.* 112 (1988) 543–555.
- [45] C. Serre, F. Garin, G. Belot, G. Maire, *J. Catal.* 141 (1993) 1–8.

- [46] S.O. Shekhtman, A. Goguet, R. Burch, C. Hardacre, N. Maguire, *J. Catal.* 253 (2008) 303–311.
- [47] I. Manuel, J. Chaubet, C. Thomas, H. Colas, N. Matthess, G. Djéga-Mariadassou, *J. Catal.* 224 (2004) 269–277.
- [48] R.H. Nibbelke, A.J. Nievergeld, J.H.B. Hoebink, G.B. Marin, *Appl. Catal. B Environ.* 19 (1998) 245–259.
- [49] M. Haruta, N. Yamada, T. Kobayashi, S. Iijima, *J. Catal.* 115 (1989) 301–309.
- [50] M. Haruta, T. Kobayashi, H. Sano, N. Yamada, *Chem. Lett.* 16 (1987) 405–408.
- [51] R. Meyer, C. Lemire, S.K. Shaikhutdinov, H.-J. Freund, *Gold Bull.* 37 (2004) 72–124.
- [52] E.J. Spanjaard, CO oxidation catalysis with substituted ceria nanoparticles, Massachusetts Institute of Technology, 2016.
- [53] J.W. Saalfrank, W.F. Maier, *Angew. Chemie - Int. Ed.* 43 (2004) 2028–2031.
- [54] Y.-F.Y. Yao, *J. Catal.* 33 (1974) 108–122.
- [55] F. Grillo, M.M. Natile, A. Glisenti, *Appl. Catal. B Environ.* 48 (2004) 267–274.
- [56] J. Jansson, *J. Catal.* 194 (2000) 55–60.
- [57] I. Lopes, A. Davidson, C. Thomas, *Catal. Commun.* 8 (2007) 2105–2109.
- [58] M. Kang, M.W. Song, C.H. Lee, *Appl. Catal. A Gen.* 251 (2003) 143–156.
- [59] J.-Y. Luo, M. Meng, X. Li, X.-G. Li, Y.-Q. Zha, T.-D. Hu, Y.-N. Xie, J. Zhang, *J. Catal.* 254 (2008) 310–324.
- [60] M.S. Yakimova, V.K. Ivanov, O.S. Polezhaeva, A.A. Trushin, A.S. Lermontov, Y.D. Tretyakov, *Dokl. Chem.* 427 (2009) 186–189.
- [61] M. Ozawa, H. Toda, O. Kato, S. Suzuki, *Appl. Catal. B Environ.* 8 (1996) 123–140.
- [62] G.G. Jernigan, G.A. Somorjai, *J. Catal.* 147 (1994) 567–577.
- [63] V.A. Sadykov, S.F. Tikhov, N.N. Bulgakov, A.P. Gerashev, *Catal. Today.* 144 (2009) 324–333.
- [64] S. Royer, D. Duprez, S. Kaliaguine, *J. Catal.* 234 (2005) 364–375.
- [65] T.-J. Huang, D.-H. Tsai, *Catal. Letters.* 87 (2003) 173–178.
- [66] D. Le, S. Stolbov, T.S. Rahman, *Surf. Sci.* 603 (2009) 1637–1645.
- [67] E.D. Pierron, J.A. Rashkin, J.F. Roth, *J. Catal.* 9 (1967) 38–44.
- [68] Y.F. Yu Yao, J.T. Kummer, *J. Catal.* 46 (1977) 388–401.

- [69] Y.-F. Yu Yao, *J. Catal.* 39 (1975) 104–114.
- [70] K.I. Choi, M.A. Vannice, *J. Catal.* 131 (1991) 22–35.
- [71] T.-J. Huang, T.-C. Yu, S.-H. Chang, *Appl. Catal.* 52 (1989) 157–163.
- [72] T.-J. Huang, T.-C. Yu, *Appl. Catal.* 71 (1991) 275–282.
- [73] A.L. Agudo, J.M. Palacios, J.L.G. Fierro, J. Laine, F. Severino, *Appl. Catal. A Gen.* 91 (1992) 43–55.
- [74] F. Severino, J.L. Brito, J. Laine, J.L.G. Fierro, A.L. Agudo, *J. Catal.* 177 (1998) 82–95.
- [75] J. Laine, F. Severino, *Appl. Catal.* 65 (1990) 253–258.
- [76] J. Laine, F. Severino, A. Lopez-Agudo, J.L.G. Fierro, *J. Catal.* 129 (1991) 297–299.
- [77] F. Severino, J. Brito, O. Carías, J. Laine, *J. Catal.* 102 (1986) 172–179.
- [78] S. Kacimi, J. Barbier, R. Taha, D. Duprez, *Catal. Letters.* 22 (1993) 343–350.
- [79] F. Mariño, C. Descorme, D. Duprez, *Appl. Catal. B Environ.* 58 (2005) 175–183.
- [80] F. Mariño, G. Baronetti, M. Laborde, N. Bion, A. Le Valant, F. Epron, D. Duprez, *Int. J. Hydrogen Energy.* 33 (2008) 1345–1353.
- [81] S. Imamura, Y. Tsuji, Y. Miyake, T. Ito, *J. Catal.* 151 (1995) 279–284.
- [82] J.S. Park, D.S. Doh, K. Lee, *Top. Catal.* 10 (2000) 127–131.
- [83] Shuhui Liang, Fei Teng, G. Bulgan, and Ruilong Zong, Y. Zhu*, (2008).
- [84] R. Hu, L. Xie, S. Ding, J. Hou, Y. Cheng, D. Wang, *Catal. Today.* 131 (2008) 513–519.
- [85] L.-C. Wang, Q. Liu, X.-S. Huang, Y.-M. Liu, Y. Cao, K.-N. Fan, *Appl. Catal. B Environ.* 88 (2009) 204–212.
- [86] A.V. Salker, R.K. Kunkalekar, *Catal. Commun.* 10 (2009) 1776–1780.
- [87] V. Iablokov, K. Frey, O. Geszti, N. Kruse, *Catal. Letters.* 134 (2010) 210–216.
- [88] S.A.C. Carabineiro, S.S.T. Bastos, J.J.M. Órfão, M.F.R. Pereira, J.J. Delgado, J.L. Figueiredo, *Catal. Letters.* 134 (2010) 217–227.
- [89] K. Frey, V. Iablokov, G. Sáfrán, J. Osán, I. Sajó, R. Szukiewicz, S. Chenakin, N. Kruse, *J. Catal.* 287 (2012) 30–36.
- [90] K. Morgan, K.J. Cole, A. Goguet, C. Hardacre, G.J. Hutchings, N. Maguire, S.O. Shekhtman, S.H. Taylor, *J. Catal.* 276 (2010) 38–48.

- [91] J.-H. Park, D.-C. Kang, S.-J. Park, C.-H. Shin, *J. Ind. Eng. Chem.* 25 (2015) 250–257.
- [92] A.C. Gluhoi, S.D. Lin, B.E. Nieuwenhuys, *Catal. Today.* 90 (2004) 175–181.
- [93] Z. Zou, M. Meng, Y. Zha, *J. Phys. Chem. C.* (2010) 468–477.
- [94] F. Arena, *Catal. Sci. Technol.* 4 (2014) 1890–1898.
- [95] F. Arena, R. Di Chio, B. Fazio, C. Espro, L. Spiccia, A. Palella, L. Spadaro, *Appl. Catal. B Environ.* 210 (2017) 14–22.
- [96] P. Zhang, H. Lu, Y. Zhou, L. Zhang, Z. Wu, S. Yang, H. Shi, Q. Zhu, Y. Chen, S. Dai, *Nat. Commun.* 6 (2015) 1–10.
- [97] F. Arena, G. Trunfio, B. Fazio, J. Negro, L. Spadaro, *J. Phys. Chem. C.* 113 (2009) 2822–2829.
- [98] X. man Zhang, Y.Q. Deng, P. Tian, H. huan Shang, J. Xu, Y.F. Han, *Appl. Catal. B Environ.* 191 (2016) 179–191.
- [99] F. Arena, G. Trunfio, J. Negro, L. Spadaro, *Appl. Catal. B Environ.* 85 (2008) 40–47.
- [100] F. Arena, J. Negro, A. Parmaliana, L. Spadaro, G. Trunfio, *Ind. Eng. Chem. Res.* 46 (2007) 6724–6731.
- [101] F. Arena, L. Spadaro, WO 2012168957 (A1), 2012.
- [102] F. Arena, G. Trunfio, J. Negro, B. Fazio, L. Spadaro, *Chem. Mater.* 19 (2007) 2269–2276.
- [103] L. Hsu, M. Tsai, Y. Lu, H. Chen, *J. Phys. Chem. C.* 117 (2013) 433–441.
- [104] W. Cen, Y. Liu, Z. Wu, H. Wang, X. Weng, *Phys. Chem. Chem. Phys.* 14 (2012) 5769.
- [105] P. Sudarsanam, B. Hillary, M.H. Amin, S.B.A. Hamid, S.K. Bhargava, *Appl. Catal. B Environ.* 185 (2016) 213–224.
- [106] F. Arena, B. Gumina, C. Cannilla, L. Spadaro, A. Patti, L. Spiccia, *Appl. Catal. B Environ.* 170–171 (2015) 233–240.
- [107] F. Larachi, *Top. Catal.* 33 (2005) 109–134.
- [108] J. Hendrick, J Cordier, D Gambogi, US Geol. Surv. Virginia, VA, USA. (2011) 198.
- [109] F. Arena, T. Torre, C. Raimondo, A. Parmaliana, *Phys. Chem. Chem. Phys.* 3 (2001) 1911–1917.
- [110] F. Arena, G. Trunfio, J. Negro, L. Spadaro, *Mater. Res. Bull.* 43 (2008) 539–545.

- [111] F. Arena, C. Italiano, A. Raneri, C. Saja, *Appl. Catal. B Environ.* 99 (2010) 321–328.
- [112] F. Arena, B. Gumina, A.F. Lombardo, C. Espro, A. Patti, L. Spadaro, L. Spiccia, *Appl. Catal. B Environ.* 162 (2015) 260–267.
- [113] P. Venkataswamy, K.N. Rao, D. Jampaiah, B.M. Reddy, *Appl. Catal. B Environ.* 162 (2015) 122–132.
- [114] M. Kobayashi, H. Kobayashi, *J. Catal.* 27 (1972) 114–119.
- [115] J. J. Thomson, *Proc. R. Soc. A* 89 (1913) 1–20.
- [116] C.J.F. R. Sleeman, *Encyclopedia of Analytical Science - Mass Spectrometry Overview*, Elsevier Ltd, Geneva, 2005.
- [117] A.J. Dempster, *Phys. Rev.* 11 (1918) 316–325.
- [118] K.M. Downard, *Eur. J. Mass Spectrom.* 13 (2007) 177–190.
- [119] R.E. March, *Encyclopedia of Analytical Science - Mass Spectrometry Ion traps*, Elsevier Ltd, Geneva, 2005.
- [120] E. de Hoffmann, V. Stroobant, *Mass Spectrometry - Principles and Applications.*, Third Ed., John Wiley & Sons Ltd, Chichester, 2007.
- [121] F. Arena, F. Frusteri, A. Parmaliana, N. Giordano, *Appl. Catal. A, Gen.* 125 (1995) 39–59.
- [122] F. Arena, F. Frusteri, A. Parmaliana, N. Giordano, *J. Catal.* 143 (1993) 299–303.
- [123] F. Arena, R. Di Chio, C. Espro, A. Palella, L. Spadaro, *React. Chem. Eng.* 3 (2018) 293–300.
- [124] F. Arena, R. Di Chio, L. Filiciotto, G. Trunfio, C. Espro, A. Palella, A. Patti, L. Spadaro, *Appl. Catal. B Environ.* 218 (2017) 803–809.
- [125] A. Parmaliana, F. Arena, *J. Catal.* 167 (1997) 57–65.
- [126] F. Arena, P. Famulari, G. Trunfio, G. Bonura, F. Frusteri, L. Spadaro, *Appl. Catal. B Environ.* 66 (2006) 81–91.
- [127] D. Li, J. Yang, W. Tang, X. Wu, L. Wei, Y. Chen, *RSC Adv.* 4 (2014) 26796–26803.
- [128] J. Jia, P. Zhang, L. Chen, *Appl. Catal. B Environ.* 189 (2016) 210–218.
- [129] K. Selvakumar, S.M. Senthil Kumar, R. Thangamuthu, K. Ganesan, P. Murugan, P. Rajput, S.N. Jha, D. Bhattacharyya, *J. Phys. Chem. C.* 119 (2015) 6604–6618.
- [130] T. Gao, H. Fjellvåg, P. Norby, *Anal. Chim. Acta.* 648 (2009) 235–239.
- [131] B. Fazio, L. Spadaro, G. Trunfio, J. Negro, F. Arena, *J. Raman Spectrosc.* 42 (2011) 1583–1588.

- [132] E. Widjaja, J.T. Sampanthar, *Anal. Chim. Acta.* 585 (2007) 241–245.
- [133] X. Zhang, J. Wei, H. Yang, X. Liu, W. Liu, C. Zhang, Y. Yang, *Eur. J. Inorg. Chem.* 2013 (2013) 4443–4449.
- [134] Y. Hamlaoui, L. Tifouti, C. Remazeilles, F. Pedraza, *Mater. Chem. Phys.* 120 (2010) 172–180.
- [135] T. Sato, T. Komanoya, *Catal. Commun.* 10 (2009) 1095–1098.
- [136] X. Wu, S. Liu, D. Weng, F. Lin, R. Ran, *J. Hazard. Mater.* 187 (2011) 283–290.
- [137] F. Larachi, J. Pierre, A. Adnot, A. Bernis, *Appl. Surf. Sci.* 195 (2002) 236–250.
- [138] C.J. Liang, J.W. Fang, *Chem. Eng. Sci.* 144 (2016) 101–107.
- [139] J. Xu, Y.-Q. Deng, Y. Luo, W. Mao, X.-J. Yang, Y.-F. Han, *J. Catal.* 300 (2013) 225–234.
- [140] J. Xu, Y. Deng, X. Zhang, Y. Luo, W. Mao, X. Yang, L. Ouyang, P. Tian, Y. Han, *ACS Catal.* (2014).
- [141] K. Ramesh, L. Chen, F. Chen, Y. Liu, Z. Wang, Y.-F. Han, *Catal. Today.* 131 (2008) 477–482.
- [142] M.C. Biesinger, B.P. Payne, A.P. Grosvenor, L.W.M. Lau, A.R. Gerson, R.S.C. Smart, *Appl. Surf. Sci.* 257 (2011) 2717–2730.
- [143] R. Craciun, B. Nentwick, K. Hadjiivanov, H. Knözinger, *Appl. Catal. A Gen.* 243 (2003) 67–79.
- [144] M.A. Vannice, *Catal. Today.* 123 (2007) 18–22.
- [145] I.E. Wachs, K. Routray, *ACS Catal.* 2 (2012) 1235–1246.
- [146] A. Bielański, J. Haber, *Oxygen in catalysis*, First Ed., Marcel Dekker Inc., New York, 1991.
- [147] C. Doornkamp, V. Ponc, *J. Mol. Catal. A Chem.* 162 (2000) 19–32.
- [148] M.I. Zaki, M.A. Hasan, L. Pasupulety, K. Kumari, *Thermochim. Acta.* 311 (1998) 97–103.
- [149] F. Arena, G. Trunfio, J. Negro, B. Fazio, L. Spadaro, *Chem. Mater.* 19 (2007) 2269–2276.
- [150] N. Drenchev, I. Spassova, E. Ivanova, M. Khristova, K. Hadjiivanov, *Appl. Catal. B Environ.* 138–139 (2013) 362–372.
- [151] C. Li, Y. Sakata, T. Arai, K. Domen, K. Maruya, T. Onishi, *J. Chem. Soc. Faraday Trans. 1 Phys. Chem. Condens. Phases.* 85 (1989) 1451.
- [152] F. Arena, R. Di Chio, L. Filiciotto, G. Trunfio, C. Espro, A. Palella, A. Patti, L. Spadaro, *Appl. Catal. B Environ.* 218 (2017) 803–809.

- [153] B.L.M. Hendriksen, J.W.M. Frenken, *Phys. Rev. Lett.* 89 (2002) 046101-1-046101-4.
- [154] F. Arena, G. Trunfio, J. Negro, C. Saja, A. Raneri, L. Spadaro, *Stud. Surf. Sci. Catal.* 175 (2010) 493–496.

APPENDIX A: LIST OF TABLES

Table 1. <i>Effects of carbon monoxide in relation to the concentration in parts per million in the air</i>	10
Table 2. <i>Literature CO₂ yield data of bare and promoted MnO_x catalysts at various temperatures.</i>	27
Table 3. <i>Physico-chemical properties of the studied catalysts.</i>	47
Table 4. <i>XPS data of the studied catalysts.</i>	54
Table 5. <i>Activation energy values (E_{app}) and activity data of the studied catalysts at 393K.</i>	58
Table 6. <i>Data of the deconvolution analysis of the Mn_{2p3/2} XPS peak (see Figure 18).</i>	60
Table 7. <i>Influence of CO and O₂ partial pressure on reaction rate at various temperatures (Figure 20A).</i>	65
Table 8. <i>Summary of literature IR spectroscopy data for CO adsorption on MnOx and MnCeOx materials.</i>	73
Table 9. <i>Slope and intercept values of the straight-line relationships obtained from rate data elaborated by the eq. 22 (Figure 30), and kinetic constant values of the various reaction steps.</i>	81

APPENDIX B: LIST OF FIGURES

Figure 1 <i>Snapshot of Real Time Air Quality Index map of (A) Europe and North America and (B) Asia; (C) Air Quality Index Chart [2].</i>	4
Figure 2. <i>Relative amount of U.S. CO emissions from anthropogenic and biogenic sources in 2011 (adapted from ref. [14]).</i>	11
Figure 3. <i>Anthropogenic CO emissions in the U.S. by sources category in the period 1990-2011 (adapted from ref. [14]).</i>	11
Figure 4. <i>Sources of global CO emissions in terms of T(CO)/yr (adapted from ref. [16]).</i>	12
Figure 5. <i>Schematics of a simple mass spectrometer with sector type mass analyzer.</i>	35
Figure 6. <i>Schematic diagram of quadrupole with adjacent rodes out-of-phase by 180° [119].</i>	36
Figure 7. (A) <i>Comparison of CO and O₂ conversion data by internal-standard and mass-balance methods ($X_{CO(MB)}/X_{CO(IS)}$) and CO-O₂ conversion values ($X_{CO(MB)}/X_{O_2(IS)}$) as a function of X_{CO}. (B) Comparison of CO conversion data of the same sample in 2016 (red line) and 2017 (blue line).</i>	40
Figure 8. (A) <i>Influence of the contact time on CO conversion and (B) CO_x molar flow.</i>	44
Figure 9. <i>Influence of the particle size on CO conversion.</i>	45
Figure 10. <i>Effect of the heating rate (β) on CO conversion.</i>	45
Figure 11. (A) <i>CO oxidation conversion of the studied catalysts in the range of 293-533K; (B) Stability test (2nd reaction cycle) of M5C1 and M catalysts. (F, 60 stp mL/min; P, 1 atm; p_{CO}^0, 0.025; $p_{O_2}^0$, 0.025; w_{cat}, 0.02 g).</i>	48
Figure 12. (A) <i>XRD patterns of the studied catalysts.</i>	50
Figure 13. <i>Laser Raman scattering spectra of the studied catalysts.</i>	52
Figure 14. <i>Influence of the cerium loading on the textural properties of the studied catalysts.</i>	53
Figure 15. <i>XPS spectra of (A) Mn_{2p}, (B) Ce_{3d}, and (C) O_{1s} core levels of the various catalysts and (D) effect of cerium loading on the AON and relative abundance of surface Mn and Ce atoms.</i>	56
Figure 16. <i>CO-TPR pattern of the studied catalysts.</i>	57
Figure 17. <i>Arrhenius plot of differential (3-10%) CO conversion data and elaboration of integral CO conversion data (3-80%) by eq. 11 [138] (inset).</i>	59
Figure 18. <i>Deconvolution analysis of the Mn_{2p} XPS peak of the various catalysts.</i>	60
Figure 19. <i>Influence of the cerium loading on: (A) surface concentration of Mn^x centers and (B) surface and MnO_x activity at 393K.</i>	62
Figure 20. (A) <i>CO conversion of the M5C1 catalyst in the range of 293-533K at different total reagents pressure (i.e., $p_{CO}^0+p_{O_2}^0=0.0125-0.05$) and (B) CO/O₂ feed ratio (i.e., $\lambda_0=p_{CO}^0/p_{O_2}^0=0.25-4$).</i>	64
Figure 21. <i>Log-plot of kinetic data (X<10%) in the range of 353-403K (data from Figure 20).</i>	65

- Figure 22. Effect of the CO_2 co-feeding ($p_{CO_2}^0$, 0-0.1 atm) on CO conversion in the range of 293-533K (p_{CO}^0 , 0.023-0.025 atm; λ_0 , 1). 66
- Figure 23. CO-pulse ($1.3 \mu mol_{CO}$) reaction test at 393K under 5% O_2/He and He carrier flow (F , 35 sccm; w_{cat} , 20 mg). 68
- Figure 24. O_2 -TPD pattern of the M5C1 catalyst exposed to CO, CO/ O_2 and CO_2 flow at 298K (1h). 69
- Figure 25. (A) CO_2 Temperature programmed desorption profiles of the M5C1 catalyst pretreated in CO, CO- O_2 and CO_2 . (B) Comparison of O_2 -TPD, CO_2 -TPD and CO-TPR of the M5C1 sample. 70
- Figure 26. Scheme of carbonate intermediates forming at the surface of TMO systems. Adapted from ref. [152]. 71
- Figure 27. Calculated potential energy diagram for CO oxidation on $Ce_{0.875}Mn_{0.125}O_2$ (111) surface and catalyst regeneration adapted from ref. [103]. 75
- Figure 28. (A) Rate of CO_2 formation at various p_{O_2} (0.0-0.025 atm); (B) and (C) Arrhenius plot of the CO_2 rate in the range of 373-473K. 76
- Figure 29. Scheme of the CO oxidation reaction cycle on the M5C1 catalyst. 78
- Figure 30. Elaboration of rate data by eq. 22 at different p_{CO} (A) and p_{O_2} (B) and Arrhenius plot of k_2 , k_3 and k_{CO_2} (C). 81
- Figure 31. Calculated vs. experimental rate values in the range of 353–403 K at different p_{CO} and p_{O_2} . 82
- Figure 32. Predicted (symbols) and experimental CO conversion data (lines) at different reagents concentration and λ_0 values. 84
- Figure 33. Van't Hoff plot of the K_3/K_1 ratio in the range of 353-513K. 85

APPENDIX C: LIST OF PUBLICATIONS AND CONGRESSES PARTICIPATION

List of publications (2015-2018)

1. F. Arena, **R. Di Chio**, C. Espro, A. Palella, L. Spadaro, *React. Chem. Eng.* 3 (2018) 293–300.
2. F. Arena, **R. Di Chio**, L. Filiciotto, G. Trunfio, C. Espro, A. Palella, A. Patti, L. Spadaro, *Appl. Catal. B Environ.* 218 (2017) 803-809.
3. F. Arena, **R. Di Chio**, B. Fazio, C. Espro, L. Spiccia, A. Palella, L. Spadaro, *Appl. Catal. B Environ.* 210 (2017).
4. F. Arena, **R. Di Chio**, G. Trunfio, *Appl. Catal. A Gen* 503 (2015) 227-236.
5. F. Arena, **R. Di Chio**, B. Gumina, L. Spadaro, G. Trunfio *Inorganica Chim. Acta* 431 (2015) 101-109.

List of congresses and schools participation (2015-2018)

1. **R. Di Chio**, F. Arena, S. G. Leonardi, G. Neri, N. Donato. “Nanostructured MnO₂ for phenolic compounds degradation and monitoring”. 2018 IEEE International Workshop on Metrology for the Sea (MetroSea 2018), October 8-10, 2018, Bari, Italy
2. L. Spadaro, A. Palella, **R. Di Chio**, F. Arena. “Insight into CO₂ utilization for energetic purposes: the catalytic hydrogenation versus the photocatalytic reduction”. International Conference on Sustainable Energy and Environment Sensing (SEES 2018), June 18-19, 2018, Cambridge city, United Kingdom. ISBN: 978-1-912532-01-8
3. F. Arena, , A. Palella, L. Spadaro. “A new class of Ce/MnOx nano-composite materials for the **R. Di Chio** exhaust emissions control: Catalytic study with CO model compound”. 11th Congress on Catalysis and Automotive Pollution Control CAPoC11, October 29- 31, 2018, Brussels, Belgium.
4. A. Palella, F. Arena, **R. Di Chio**, L. Spadaro. “Combining different X-ray characterization techniques for the definitive assessment of composition and chemical structure of metallic contaminants in exhausted catalysts.” 11th Congress on Catalysis and Automotive Pollution Control CAPoC11, October 29-31, 2018, Brussels, Belgium.

5. A. Palella, F. Arena, **R. Di Chio**, L. Spadaro “Desulfuration processes in refinery and biorefinery: Insight into the role of catalyst protection by catalytic study in the o-xylene hydrogenation process”. International Conference on “Petroleum Engineering” 2018, August 06-07, 2018, Dubai, UAE
6. L. Spadaro, A. Palella, **R. Di Chio**, F. Arena. “Biofuels from bio-oils upgrading via HDO process, catalytic study with MTBE model compound”. International Conference on “Petroleum Engineering” 2018, August 06-07, 2018, Dubai, UAE
7. **R. Di Chio**, C. Espro, A. Palella, L. Spadaro, F. Arena. “Scientific and engineering issues of the CO oxidation on nanocomposite MnCeO_x catalysts”. 1st International Conference on Reaction Kinetics, Mechanisms and Catalysis (RKMC 2018), June 6-9, 2018, Budapest, Hungary.
8. F. Arena, **R. Di Chio**, C. Espro, A. Palella, L. Spadaro. “Mechanism and kinetics of CO oxidation on nanostructured MnCeO_x catalysts”. International Conference on Catalysis and Surface Chemistry, March 18-23, 2018, Krakow, Poland.
9. F. Arena, **R. Di Chio**, C. Espro, A. Palella, L. Spadaro. “Catalytic Wet Air Oxidation (CWAO) of Industrial Wastewaters: Mechanistic Evidences, Catalyst Development and Kinetic Modeling”. Frontiers International Conference on Wastewater Treatment. May 21-24, 2017, Palermo, Italy.
10. **R. Di Chio**, L. Filiciotto, C. Espro, G. Trunfio, L. Spadaro, F. Arena. “Effect of oxide promoters on the total oxidation functionality of nanocomposite MnO_x catalysts: mechanism and kinetics of the CO oxidation reaction”. Reaction rate theory – Faraday Discussion. September 19-21, 2016, Cambridge, United Kingdom.
11. **R. Di Chio**, F. Arena, G. Trunfio. “A comprehensive assessment of the surface acidic properties of heterogeneous catalysts by the Ammonia Temperature Programmed Desorption technique”. International Winter School “Molecules@Surfaces”. January 31 – February 5, 2016, Bardonecchia (TO), Italy.